DOCTORAL THESIS IN PHOTONICS
ICFO BARCELONA 2014

Hybrid diffuse optics for monitoring of tissue hemodynamics with applications in oncology

PARISA FARZAM
Advisor: Turgut Durduran

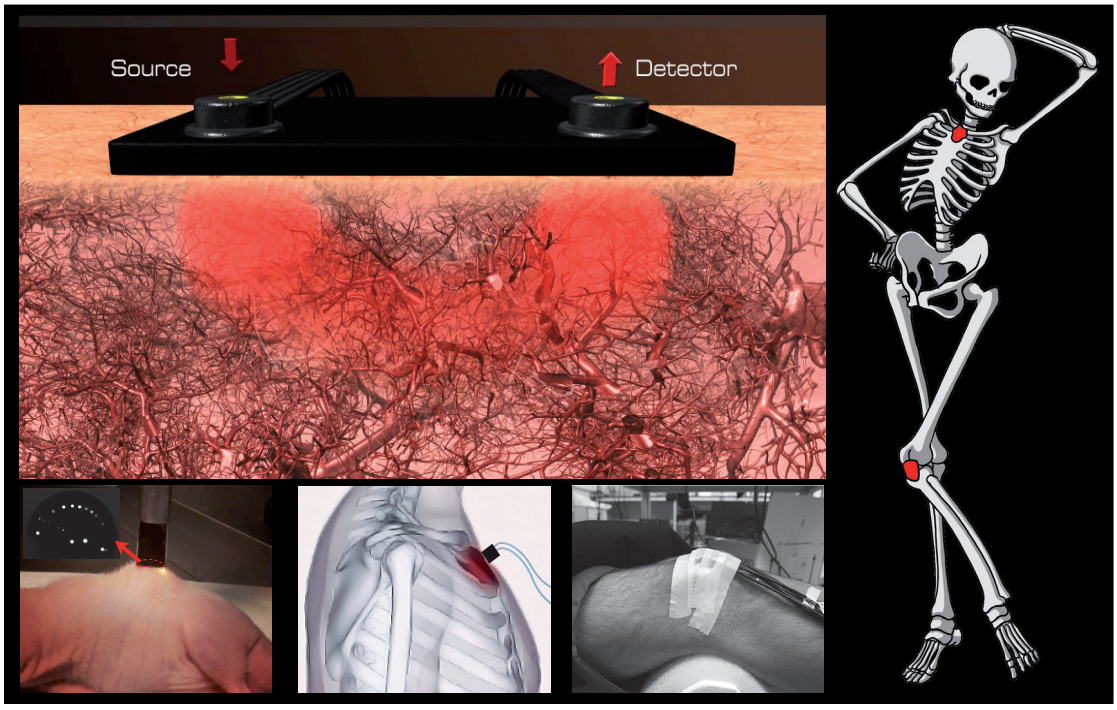

Doctor of Philosophy in Photonics

Institute of Photonic Sciences (ICFO)

Hybrid diffuse optics for monitoring of tissue hemodynamics with applications in oncology

by Parisa Farzam

Ph.D. Dissertation
Advisor: Prof. Turgut Durduran

Barcelona, July 2014

نازنین مادرم، فرزانه پدرم،

پایان نامه دکترایم هرچه هست بیش یا کم،

پیشکش ناز سرانگشتان شما.

Declaration

I hereby declare that except where specific reference is made to the work of others, the contents of this dissertation are original [1] and have not been submitted in whole or in part for consideration for any other degree or qualification in this, or any other university.

Parisa Farzam
July 2014

[1] Two photos in the cover page are adopted from from:
http://www.wikihow.com/Draw-a-Cartoon-Skeleton and
http://commons.wikimedia.org/wiki/File:Manubrium_lateral.png

Acknowledgements

It is a great pleasure for me to acknowledge all the people who have supported me with their love and helped me to get to this point. Turgut is definitely on top of my list. I met Prof. Turgut Durduran in one of his amazing lectures. After his talk, I was absolutely sure that I want to peruse my academic career in his lab. I was lucky enough to be his first PhD student at ICFO and this gave me the invaluable opportunity to have his presence in the lab, long discussions, and deep education. Turgut is a brilliant advisor whose talent, creativity, critical thinking, and hardworking make him a special person. He aimed to make an independent researcher out of me and now I feel confident to find new problems and step forward to solve them on my own. He was not only a wonderful advisor, but he was also a great friend who has helped me in all my difficulties. I have no words to show my respect to him.

My research was not possible without the support of excellent clinical collaborators. I consider it an honor to work with Dr. Oriol Casanovas, Dr. Alvaro Urbano, Dr. Angels Sierra, and Dr. Tiziano Binzoni. Although I won't be able to list all our collaborators, I owe my deepest gratitude to all of them.

I took advantage of presence of Dr. Efrain Solarte and Dr. Joseph Culver at ICFO that gave me the chance to attend several of their lectures. I also had the privilege to visit Prof. Arjun Yodh lab in University of Pennsylvania. I am thankful of Dr. Rickson Mesquita who helped me during this visit and patiently accepted me in the hospital to be involve in their *in-vivo* measurements. I also would like to thank

Dr. Regine Choe who has been always welcoming to my questions and discussions.

I share the credit of my work with all my colleagues and my good friends in medical optics group, including Peyman Zirak, Johannes Johanson, Hari Varma, Igor Blanco, Claudia Valdes, Claus Lindner, Taisuke Minagawa, Mehmet Suzen, Alexia Giannoula, Udo Weigel, Juan Aguirre, Anna Kristoffersen, Francisco Remiro, Miguel Mireles, Jordi Morales Dalmau, Clara Gregori, Tanja Dragojevic, Marco Pagliazzi, Martina Giovannella, Victor Chamizo and many more. You made these years full of good memories. I miss all 32 of you. Are you really counting? Then include Maria please! Beside the medical optics group, I am deeply grateful to all ICFOnians specially Prof. Lluis Torner whose remarkable management made ICFO a fabulous center, Prof. Majid Ebrahim-Zadeh my respected advisor in master project who helped me a lot from my very first day in Barcelona, and Prof. David Artigas who was always kindly there to help me when I was lost and confused. I am thankful of ICFO's human resources (Anne, Laia, Mery, Manuela and Cristina), electronic and mechanical workshop and all my friends at ICFO.

During my PhD, I lost my beloved grandma without having the chance to say goodbye to her. She was my angle who treated me with pure love and good tea. I share my graduation happiness with her memory and with my lovely friends, cousins, aunts and uncles. I do not list your names here but I am grateful to have all of you in my life.

My heartfelt appreciation goes to my beloved father (Jafar), my amazing mother (Soori), and my awesome brother (Arash). You three are the light of my life. I can not think of a better place to grow rather than a house with you.

I want to dedicate not only this thesis but also my entire life to my dearest, Behrooz. You brought me laughter and joy. You gave me all one can imagine to have. I am thankful of your existence.

Abstract

Hybrid diffuse optics for monitoring of tissue hemodynamics with applications in oncology

Parisa Farzam

Noninvasive measurement of hemodynamics at the microvascular level may have a great impact on oncology in clinics for diagnosis, therapy planning and monitoring, and, in preclinical studies. To this end, diffuse optics is a strong candidate for noninvasive, repeated, deep tissue monitoring.

In this multi-disciplinary, translational work, I have constructed and deployed hybrid devices which are the combination of two qualitatively different methods, near infrared diffuse optical spectroscopy (NIRS) and diffuse correlation spectroscopy (DCS), for simultaneous measurement of microvascular total hemoglobin concentration, blood oxygen saturation and blood flow.

In a preclinical study, I applied the hybrid device to monitor the response of renal cell carcinoma in mice to antiangiogenic therapy. The results suggest that we can predict the output of therapy from early hemodynamic changes, which provide us with valuable information for better understanding of the tumor resistance mechanism to antiangiogenic therapies.

In two *in vivo* studies in human volunteers, I have developed protocols and probes to demonstrate the feasibility of noninvasive diffuse optical spectroscopy to investigate the pathophysiology of bone. First study was study on the physiology of the patella microvasculature, the other introduced the manubrium as a site that is rich in red bone marrow and accessible to diffuse optics as a potential window to monitor the progression of hematological malignancies.

Overall, during my Ph.D., I have developed instrumentation, algorithms and protocols and, then, applied this technique for preclinical and clinical investigations. My research is a link between preclinical and clinical studies and it opens new areas of applications in oncology.

Resumen

Óptica difusa híbrida para la monitorización de la hemodinámica de los tejidos con aplicaciones en oncología

Parisa Farzam

La medición no invasiva de la hemodinámica a nivel microvascular puede alcanzar un gran impacto en oncología: en las clínicas para el diagnóstico, la planeación y monitorización de las terapias, y en estudios preclínicos. La óptica difusa es una fuerte candidata para la monitorización no invasiva y repetida del tejido profundo.

En este trabajo multidisciplinario y traslacional, construí e implementé dispositivos híbridos que son la combinación de dos métodos cualitativamente diferentes: espectroscopía infrarroja de óptica difusa -near infrared diffuse optical spectroscopy (NIRS)- y espectroscopía de correlación de luz difusa -diffuse correlation spectroscopy (DCS)-. Estos híbridos permiten la medición simultánea de la concentración de hemoglobina total en sangre, la saturación de oxígeno y el flujo sanguíneo.

En un estudio preclínico, apliqué el dispositivo híbrido para monitorizar la respuesta de carcinomas de células renales, implantados en ratones, a terapias antiangiogénicas. Los resultados sugieren que podemos predecir la evolución de la terapia con base en cambios hemodinámicos

tempranos, lo cual proporciona información valiosa para un mejor entendimiento del mecanismo de resistencia de los tumores a las terapias antiangiogénicas.

En dos estudios *in vivo* realizados en pacientes voluntarios, desarrollé protocolos y sondas para demostrar la viabilidad de la espectroscopía de óptica difusa no invasiva en el estudio de la patofisiología ósea. El primer estudio se concentró en la fisiología microvascular de la rótula y en el otro se muestra que el manubrio, hueso rico en médula ósea roja, es un sitio accesible para la óptica difusa, y se presenta como una ventana para monitorizar la progresión de enfermedades hematológicas malignas.

En resumen, durante mi trabajo doctoral, desarrollé instrumentación, algoritmos y protocolos que posteriormente apliqué en estudios preclínicos y clínicos. Mi trabajo de investigación constituye así un enlace entre estos estudios y abre nuevas áreas de aplicación en oncología.

Table of contents

List of figures

List of tables

Nomenclature

α	fraction of dynamic photon scattering events in medium
c_i	concentration of the ith chromophore
D	photon diffusion coefficient, $D = \nu/3(\mu_a + \mu_s{}')$
D_b	Brownian diffusion coefficient
ϵ	extinction coefficient
g	scattering anisotropy factor
G_0	homogeneous Green's function solution of diffusion equation
G_1	electric field temporal autocorrelation function, $G_1(\boldsymbol{\rho}, \tau, t) =< E^*(\boldsymbol{\rho}, t)E(\boldsymbol{\rho}, t+\tau) >$
G_2	intensity autocorrelation function, $G_2(\boldsymbol{\rho}, \tau, t) =< I(\boldsymbol{\rho}, t)I(\boldsymbol{\rho}, t+\tau) >$
g_1	normalized electric field temporal autocorrelation function, $g_1(\boldsymbol{\rho}, \tau, t) = G_1(\boldsymbol{\rho}, \tau, t)/ < E^*(\boldsymbol{\rho}, t)E(\boldsymbol{\rho}, t) >$
g_2	normalized intensity autocorrelation function, $g_2(\boldsymbol{\rho}, \tau, t) = G_2(\boldsymbol{\rho}, \tau, t)/ < I(\boldsymbol{\rho}, t)I(\boldsymbol{\rho}, t) >$
$I(\boldsymbol{\rho}, t)$	light field intensity at position $\boldsymbol{\rho}$ and time t

l_{tr}	transport mean-free path, $l_{tr} \approx 1/\mu_s{}'$
λ	wavelength of light (nm)
λ_{DPDW}	wavelength of diffuse photon wave density (nm)
μ_a	absorption coefficient
μ_s	scattering coefficient
$\mu_s{}'$	reduced scattering coefficient, $\mu_s{}' = \mu_s(1-g)$
ν	speed of light in tissue
$\langle \Delta r^2(\tau) \rangle$	mean-square displacement in time τ of the scattering particles (e.g., red blood cells)
$\Phi(\boldsymbol{\rho}, t)$	photon-fluence rate at position $\boldsymbol{\rho}$ and time t
ρ	distance between source and detector
τ	delay time
$U(\boldsymbol{\rho})$	photon-fluence rate; expressed in the frequency domain, $\Phi(\boldsymbol{\rho}, t) = U(\boldsymbol{\rho})e^{-iwt}$
ω	source modulation frequency

Abbreviations

BFI	blood flow index estimated by DCS (i.e., αD_b)
BMI	body mass index
CCD	charge-coupled device
CT	computed tomography
CW	continuous wave

DCS	diffuse correlation spectroscopy
DOS	diffuse optical spectroscopy
DOT	diffuse optical tomography
DPDW	diffuse photon wave density
FD	frequency domain
Hb	deoxyhemoglobin
HbO_2	oxyhemoglobin
LME	linear mixed effect
MD-DCS	multi distance diffuse correlation spectroscopy
MRI	magnetic resonance imaging
NIRS	near infrared spectroscopy
PDT	photodynamic therapy
PET	positron emission tomography
QE	quantum efficiency
QTH	quartz tungsten halogen
RBCs	red blood cells
RCC	renal cell carcinoma
SO_2	blood oxygen saturation
THC	total hemoglobin concentration
TRS	time resolved spectroscopy
TTP	time-to-progress

Chapter 1

Introduction

In many languages feelings and emotions are described by colors – *"It was embarrassing, she blushed."*. One can learn a lot by looking at the color changes in a person's face. If we can see deeper than skin we will observe how diseases alter the tissue colors. Sounds exciting? It is what my dissertation is about – diffuse optics.

Diffuse optical spectroscopy, often denoted as near infrared spectroscopy (NIRS), has recently found many applications in biomedicine due to advances in the physical modeling of photon propagation through tissues, improvements in analysis algorithms, detector and source (laser, lamp etc) technologies as well as better understanding of its capabilities in relation to the physiological/clinical problems [1, 2].

The technique relies on the "physiological window" (650-950 nm) (figure 1.1) where the photon propagation in the tissue is dominated by scattering rather than absorption [3]. In this part of the spectrum , as it is shown in figure 1.2, light experiences many scattering events and can penetrate several centimeters (>5 cm) into the tissue due to the low absorption. As a rule of thumb, the mean light penetration depth in the reflection geometry is about half of source-detector separation. The sampled volumes in the reflection geometry, the map of the visitation

probabilities of the detected photons from a particular source , has the so-called “banana shape” (figure 1.2).

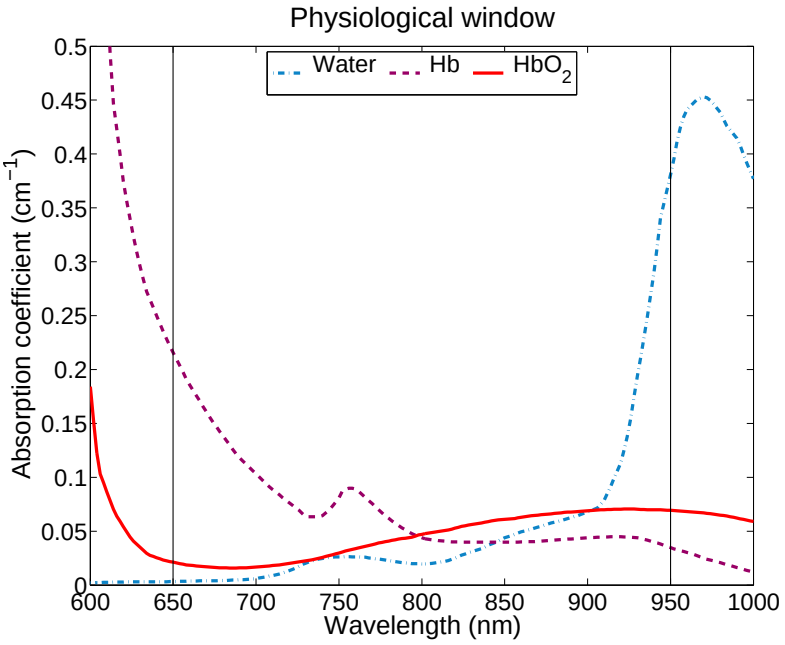

Fig. 1.1 Absorption (μ_a) spectra of water, deoxy- and oxy-hemoglobin in part of visible and near infrared range. The inset shows the “physiological window” where the absorption is relatively low and photon propagation is dominant by scattering events and photons can penetrate deep in the tissue.

Furthermore, in the “physiological window” there are clear features in the absorption spectra which enables us to estimate the chromophores concentrations (such as oxy- and deoxy-hemoglobin concentrations) and related them to total hemoglobin concentration (blood volume), blood oxygen saturation and oxygen consumption [4–7].

The main chromophores in this window are oxyhemoglobin (Hbo_2), deoxyhemoglobin (Hb), water (H_2O) and lipids. For typical concentrations their spectrum is shown in figure 1.1. This is all done in the

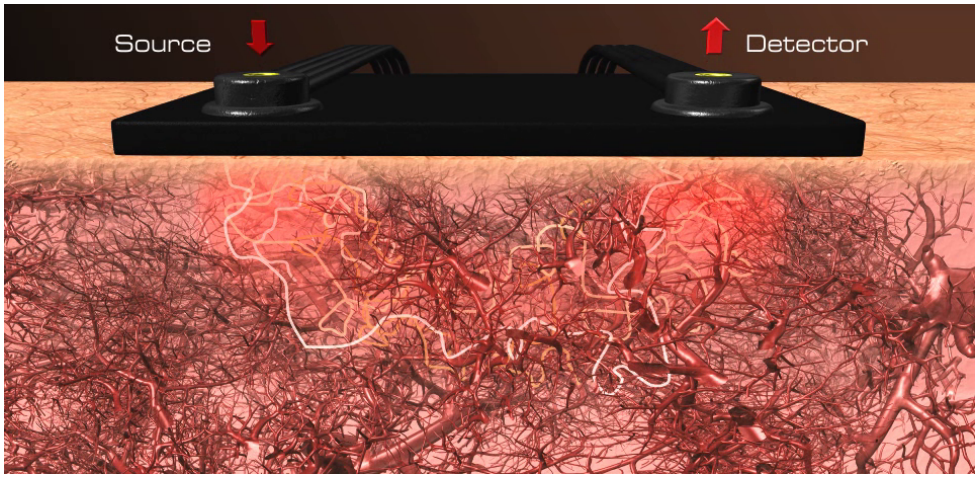

Fig. 1.2 The photons undergo multiple scattering events while propagating in a turbid media (such as tissue). These repeated scatterings change the direction of the photon path (random walk). The shadow of "banana shape" showing the sampled volumes in the reflection geometry which is the most probable path of photons for a given source-detector pair.

microvasculature which makes the technology particularly unique as a noninvasive monitoring and imaging tool. Knowing the concentration of oxygenated and deoxygenated hemoglobin provided us with information about the blood oxygen saturation which is an vital parameter and noninvasive measurement of it can provide valuable information over a wide range of medical conditions. For instance cerebral oxygenation monitoring has a great importance in minimizing secondary hypoxic and ischemic brain damage following severe head injury [8–11] or tumor hypoxia is an crucial parameter in oncology [12–15] therefore knowledge about oxygen level has a high impact on cancer therapies [16, 17]. For instance figure 1.3 shows the difference in the reflected spectrum (measured by the system described in the next chapters) of healthy tissue and tumor due to the hypoxia in the tumor. In hypoxic tissue (tumor) there is an absorption peak at ∼760 nm, which is the absorption peak of deoxyhemoglobin.

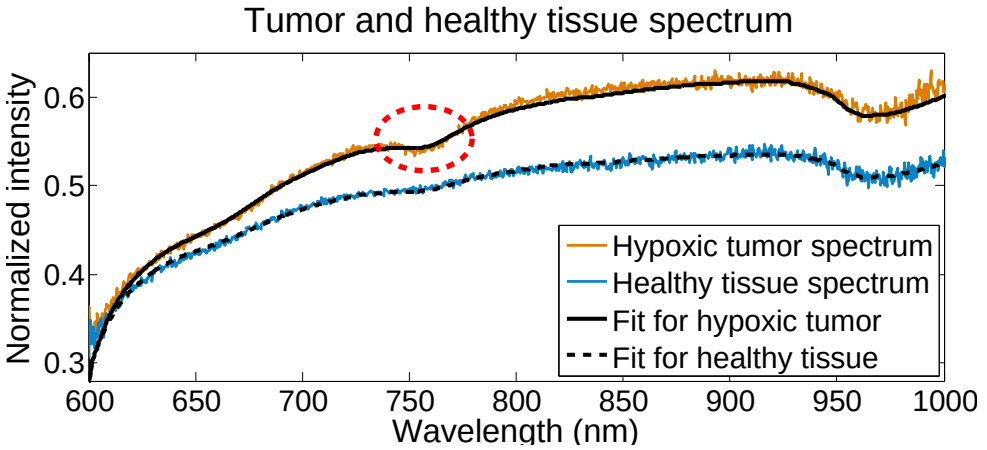

Fig. 1.3 The difference in the reflected spectrum of healthy tissue and tumor due to the hypoxia in the tumor. In hypoxic tissue (tumor) there is an absorption peak at ∼760 nm, which is the absorption peak of deoxyhemoglobin.

Deploying multiple wavelengths enables us to measure Oxy- and

deoxy-hemoglobin concentration as well as water, lipid, bone minerals and other desired tissue chromophores as the endogenous contrast species [18]. The sensitivity of measurement can be increased by the measurement of the concentration and lifetime of exogenous for example in the tumors [19–23]. Furthermore, from the speckle patterns of the multiply scattered light more information about dynamic properties of tissue (blood flow) can be obtained by a relatively new NIR technique, called diffuse correlation spectroscopy (DCS) or diffuse wave spectroscopy (DWS) [24–31]. DCS has been validated against perfusion magnetic resonance imaging (MRI) [32–36], power Doppler ultrasound [37, 38], Doppler ultrasound [39–42], laser Doppler [43, 44], Fluorescent microspheres [45], and xenon-enhanced computed tomography [46].

Hybrid devices, combination of traditional NIRS devices and DCS, contain information from both static (total hemoglobin concentration and oxygen saturation) and dynamic (blood flow) properties of tissue which can provide us with information about metabolism of the tissue, which is an important clinical parameter.

Although diffuse optics is limited by its resolution, due to its ability to noninvasively measure vital physiological parameters, it has found a wide range of applications specially in neurology and oncology [47–55]. In neurology it has been applied mostly in brain functional spectroscopy and imaging [56–66], brain studies in animal models [35, 44, 45, 67–77], stroke and brain damage investigation in adults and neonates [34, 40, 41, 78–87]. Wide range of neurological studies suggest that diffuse optics can play an important role not only as a complex research tool at the laboratory stage, but also as a powerful instrument for clinical applications.

Optical mammography mostly focuses in classifying women with high risk of breast cancer, diagnosis, characterization of malignant tumors, and monitoring the therapy efficiency [88–104]. All these studies

demonstrated the feasibility of employing diffuse optics for detecting, imaging, characterizing and monitoring the hemodynamic changes in cancer.

Diffuse optics has been applied in experimental oncology to study tumors in animal samples for better understanding of cancer mechanisms and drug development [37, 38, 105–110]. Murine models are the most popular *in vivo* models in oncology study since they an approximation of reality. Due to their similarity to the human in terms of genetics, anatomy and physiology, and ease of manipulation [111], they have been proven to be useful for novel cancer therapeutic strategies [112, 113].

My PhD is motivated mainly by application of diffuse optics for cancer studies to enhance the efficiency of new therapies and drugs. For this goal, I have applied hybrid diffuse optical devices to measure oxygen saturation, total hemoglobin concentration (blood volume), and blood flow which are important biomarkers of angiogenesis. Angiogenesis, formation of new vessels, is a necessary process for tumor growth and metastasis. One of the new class of cancer drugs are angiogenesis inhibitors. These type of therapy does not follow the general rules of conventional chemotherapy. The successful translation of angiogenesis inhibitors to clinical application depends on better understanding of angiogenesis in the tumor and the mechanisms of antiangiogenic therapies. As described, murine models are the good options for these investigations. In order to study murine tumors, we have combined broadband near infrared spectroscopy (NIRS) and diffuse correlation spectroscopy (DCS) in a single hand-held self-calibrating probe for noninvasive, repeated hemodynamic monitoring of murine tumors. The details of each device specification, probe design and validation tests are described in chapter 3.

After successful validation of device, we moved it to the animal fa-

cility of IDIBELL (Bellvitge Biomedical Research Institute, Barcelona, Spain) for a multidisciplinary collaboration with Dr. Oriol Casanovas. We have monitored the hemodynamics of the murine tumors during antiangiogenic therapy for better understanding of tumors mechanisms again antiangiogenic therapies. The details of measurements and results are described in chapter 4.

To continue the cancer studies in clinical stage, we initiated a collaboration with Dr. Alvaro Urbano at Hematology Department of Hospital Clínic de Barcelona in order to investigate the feasibility of applying diffuse optics in hematological malignancies. Most of the hematological malignancies originate in the bone marrow and alter its hemodynamics. Therefore, noninvasive methods that measure changes in hemodynamics induced by angiogenesis in the bone marrow have a potential impact on the earlier diagnosis, more accurate prognosis and in treatment monitoring. To this end we have applied hybrid diffuse optical spectroscopy methods, time resolved spectroscopy (TRS) and DCS, to evaluate the feasibility of the noninvasive hemodynamics measurement in the healthy manubrium as a site of bone marrow. The measurement protocol and the details of the measured optical and physiology properties can be found in chapter 5.

My interest in bone marrow led me to review the literature of bone optical properties. Despite skeletal muscle which is a well studied tissue [33, 114–119], the research on bone optical properties was very limited. Noninvasive, quantitative and practical measurements of local microvascular hemodynamics of bones could improve our fundamental understanding of bone function with potential applications in diagnosis and treatment of bone diseases [120–122]. This motivated me to apply optics to answer some physiological questions about bone hemodynamics. Having this goal in mind, we have started a collaboration with Dr. Tiziano Binzoni from University of Geneva, who is one the

pioneers of optical studies of bone. In this collaborative work we investigate the cardiac cycle related pulsatile behavior of the absorption and scattering coefficients of diffuse light and the corresponding alterations in hemoglobin concentrations in the human patella. The physiological origin of the observed signals was confirmed by applying a thigh cuff. Moreover, we have investigated the optical and physiological properties of the patella bone and their changes in response to arterial cuff occlusion. The details of this study is presented in chapter 6.

As it is described, I have performed optical measurements on human and animal by hybrid (NIRS-DCS) devices. Can we utilize the full set of information available from multi-distance DCS measurements for better absolute quantification instead of hybrid devices? This question led me to develop a new algorithm using multi-distance DCS for simultaneous measurement of absorption and scattering coefficient as well as blood flow index. The fitting is validated against numerical data, tissue simulating phantoms, and *in-vivo* measurements. The multi-distance DCS fitting is proposed as an alternative to hybrid NIRS-DCS devices for some applications. The fitting algorithm and validation data are presented in chapter 7.

Chapter 2

Theoretical background

2.1 Light propagation in tissues

The propagation of the photons in tissues is mainly affected by scattering rather than absorption. In this highly scattering medium few length scales are important: "scattering length" which corresponds to the typical distance traveled by photons before they scatter and its reciprocal is named scattering coefficient (μ_s). The longer distance, "transport mean-free path", l_{tr}, is the typical distance traveled by photons before their direction is randomized. The reciprocal of the photon transport mean-free path is called the reduced scattering coefficient $\mu_s{}' = 1/l_{tr}$.

The absorption length in tissue corresponds to the typical distance traveled by a photon before it is absorbed; its reciprocal, the absorption coefficient, is denoted by μ_a. All three of these length scales are wavelength-dependent [2].

Through this manuscript the light propagation in tissue is described by "diffusion equation" where the photon fluence rate, $\Phi(\boldsymbol{\rho}, t)$ $(photons/[cm^2 s])$, obeys the diffusion equation [123–125]:

$$\nabla \cdot (D(\boldsymbol{\rho})\nabla\Phi(\boldsymbol{\rho}, t)) - \nu\mu_a(\boldsymbol{\rho})\Phi(\boldsymbol{\rho}, t) - \frac{\partial\Phi(\boldsymbol{\rho}, t)}{\partial t} = -\nu S(\boldsymbol{\rho}, t). \quad (2.1)$$

This photon diffusion equation is valid when the radiance is nearly isotropic. This isotropy is achieved when $\mu_s{}' \gg \mu_a$ and and when photon propagation distances within the medium are large relative to l_{tr} that needs optode distance ($\rho = |\boldsymbol{\rho}|$) to be more than $3l_{tr}$. In addition, the assumptions of isotropic source, slow temporal flux variations, and rotational symmetry should be valid [126]. Here, ν is the speed of light in the medium (cm/s) and $D = \frac{\nu}{3(\mu_a+\mu_s{}')}$ is the photon diffusion coefficient. To apply the photon diffusion equation the diffused light is detected at a known distance from the source.

2.2 Source types

One can categorize near infrared spectroscopy (NIRS) methods based on the source type. Three types of light sources are used in diffuse optics as it is shown in figure 2.1: continuous wave, intensity modulated and time pulsed.

The simplest source type is CW, where the intensity remains constant over time [37, 38, 43, 44, 50, 58, 68–70, 74, 80, 91, 92, 95, 97, 105–109, 127–137]. CW measurements are simple and fast but they contain low amount of information. By single continuous wave (CW) measurement one can measure effective attenuation of medium but contribution of μ_a and $\mu_s{}'$ cannot readily be decoupled.

Intensity modulated sources are more complex but also provide more information about the medium [35, 41, 45, 77, 85, 89, 116, 117, 119, 130, 132, 138–144]. In frequency domain (FD) measurements light intensity of the source is modulated with a frequency in order of 100 MHz or larger, up to ∼1 GHz, producing a diffusive wave in the medium oscillating at the same frequency. At a given source-detector separation, both the amplitude and phase of the diffusing wave are measured. The increase of phase shift and intensity decrease over several

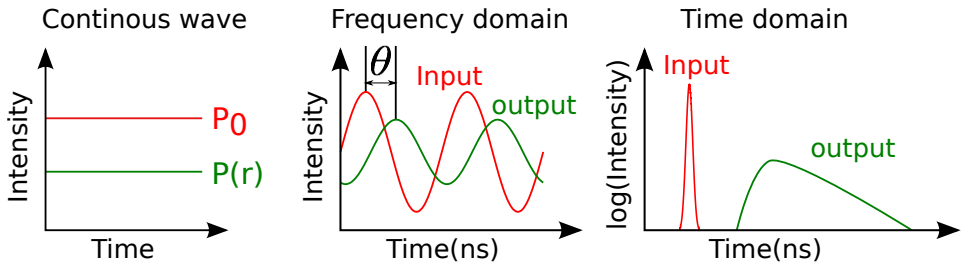

Fig. 2.1 Three types of sources that are deployed to measure optical properties of medium. [Left] continuous wave (CW) is the simplest method that measures the intensity drop at a specific distance from the source. P_0 is the intensity of the incident light and P(r) is detected intensity at distance r from the source. [Middle] Frequency domain that delivers intensity modulated light to the medium and measures the phase shift (θ) and intensity drop of the detected light. [Right] Time resolved spectroscopy (TRS) that shoots a narrow pulse to the medium and measures the broadening of the pulse.

source-detector separations provide simultaneous determination of μ_a and μ_s'. Time-domain technique (time resolved spectroscopy, TRS) is Fourier transform of frequency modulated measurement and it contains the same information content as FD measurement which is scanned over the wide range of modulation frequencies present in the pulse [51, 75, 90, 114, 145–157]. Due to multiple scattering in tissues the pulse temporally broadens. The information about optical properties of tissue can be extracted from the broadening of the detected light.

2.3 Diffuse photon density waves (DPDW)

The following theoretical discussion will be given in the frequency domain (assumption of $\omega = 0$ will be CW formulation), with the time-domain solution given for a common case. When the source of photons

in a turbid medium is intensity modulated, with "ac" and "dc" components (S_{ac} and S_{dc}), the photon fluence will oscillate at the same frequency. This small but measurable traveling wave disturbance of the light energy density is referred to as a diffuse photon density wave that oscillate at the same angular frequency as the source. [138, 158, 159]. The source term can be written as $S(\boldsymbol{\rho}, t) = S_{dc}(\boldsymbol{\rho}) + S_{ac}(\boldsymbol{\rho})e^{-iwt}$.

These ac solutions that oscillate at the same angular frequency as the source will have the following general form:

$$\Phi_{ac}(\boldsymbol{\rho}, t) = U(\boldsymbol{\rho})e^{-iwt}. \tag{2.2}$$

By substituting equation 2.2 to diffusion equation (equation 2.1) we have:

$$\nabla \cdot (D(\boldsymbol{\rho})\nabla U(\boldsymbol{\rho})) - (\nu\mu_a(\boldsymbol{\rho}) - i\omega)U(\boldsymbol{\rho}) = -\nu S(\boldsymbol{\rho}, t)),$$

which for the homogeneous medium will be simplified to:

$$(\nabla^2 - k^2)U(\boldsymbol{\rho}) = -\frac{\nu}{D}S_{ac}(\boldsymbol{\rho}).$$

The fluence rate of DPDW [2] in infinite geometry is:

$$U(\rho) = \frac{\nu S_{ac}}{4\pi D\rho}exp(-k\rho). \tag{2.3}$$

In equation 2.3, k is a complex wavevector $k = k_r + ik_i$:

$$k_r = (\frac{\nu\mu_a}{2D})^{1/2}[(1 + [\frac{\omega}{\nu\mu_a}]^2)^{1/2} + 1]^{1/2}, \tag{2.4}$$

$$k_i = -(\frac{\nu\mu_a}{2D})^{1/2}[(1 + [\frac{\omega}{\nu\mu_a}]^2)^{1/2} - 1]^{1/2}. \tag{2.5}$$

The real and imaginary parts of wavevector (k_r, k_i) are both function

of modulation frequency. The higher modulation frequency the larger wavevector. The dependency of k_r and k_i on modulation frequency is illustrated in figure 2.2. Writing the fluence rate in the form $U(r) = Ae^{i\theta}$,

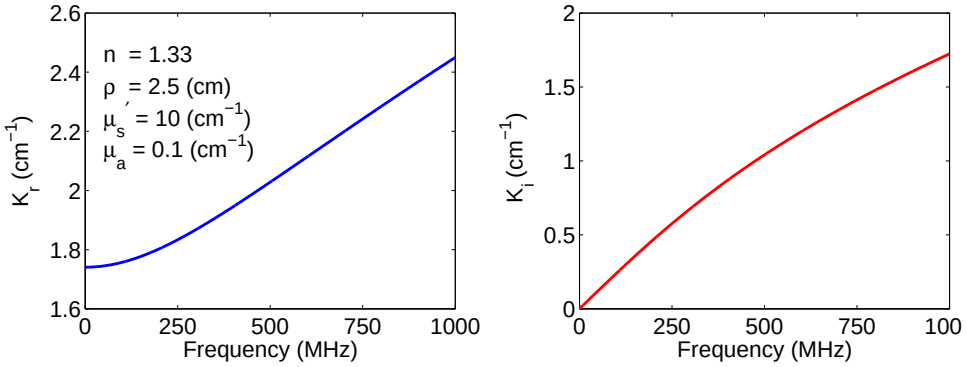

Fig. 2.2 The dependency of real and imaginary parts of diffuse wave density wavevector (k_r, k_i) on modulation frequency (ω).

the determination of the change in wave amplitude, A, and wave phase, θ, with distance from the source enables experimenters to extract μ_a and $\mu_s{}'$ of the turbid medium.

DPDWs have been demonstrated to exhibit several familiar wave-like properties including diffraction, refraction, interference and dispersion [159–162]. Figure 2.4 shows the dependency of DPDW's wavelength on optical properties of the medium as well as its intensity modulation. While its wavelength, λ_{DPDW}, has direct relation with the absorption coefficient (μ_a) of the medium, it has inverse relation with reduced scattering coefficient ($\mu_s{}'$), ratio of index of refraction to the outside (n) and modulation frequency (ω).

While the DPDW propagates in the medium by getting further from the source its amplitude decreases. The amplitude of DPDW and its decline over distance depends on optical properties of the medium. Figure 2.5 demonstrates the dependency of amplitude of different source-

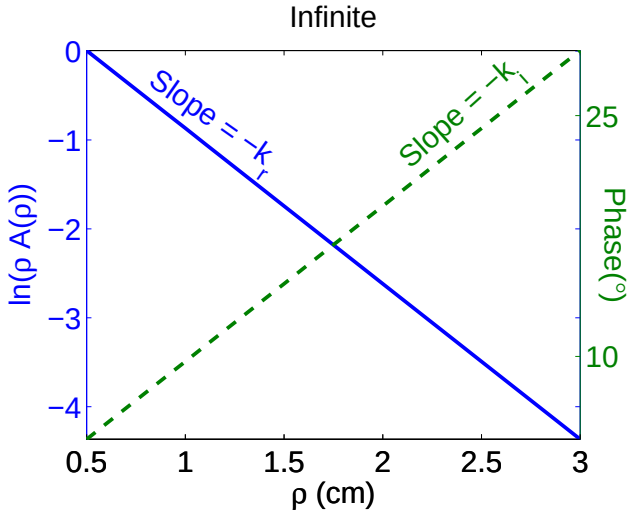

Fig. 2.3 The phase shift,(green dashed line), and $\ln(A\rho)$, (blue solid line), are plotted as the function of distance from the source in an infinite turbid medium. The slopes reveal $-k_i$ and $-k_r$ (effective attenuation coefficient, μ_{eff}), from which μ_a and $\mu_s{}'$ can be calculated using equations 2.4 and 2.5.

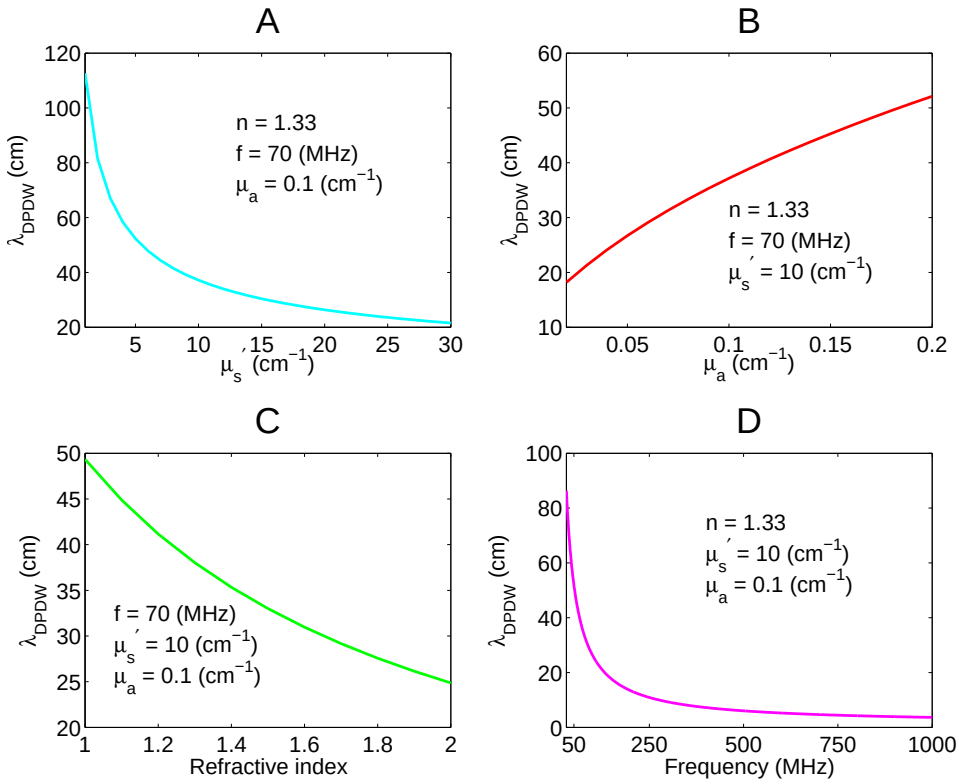

Fig. 2.4 The dependency of DPDW wavelength (λ_{DPDW}) on optical properties of the medium and modulation frequency. [A] The reverse relation of DPDW's wavelength and reduced scattering coefficient (μ_s') of the medium. [B] In the medium with higher absorption (μ_a), the wavelength of DPDW is larger. [C] In the medium with higher index of refraction, the wavelength of DPDW smaller. [D] The wavelength of DPDW has reverse relation with the modulation frequency.

detector separations on the optical properties of tissue. In figure 2.5-A the relation between amplitude and μ_s' is presented. In small values of μ_s' and small source-detector separations increase of μ_s' lead to rise in amplitude. While in larger μ_s' and larger source-detector separations higher μ_s' results to lower amplitude. Figure 2.5-B shows the reverse relation between absorption in the medium and the amplitude of DPDW. Similarly, Figure 2.5-c shows increase in ratio of index of refraction lead to decrease in intensity. Finally, the amplitude The amplitude decreases with increase of modulation frequency. (figure 2.5-D).

Due to multiple scattering in tissues by getting further from the source the phase increases. The dependency of phase on the medium optical properties as well as source modulation frequency over different source-detector separations is demonstrated in figure 2.6. While phase has reverse relation with the absorption coefficient (μ_a) of the medium, it has direct relation with reduced scattering coefficient (μ_s'), index of refraction (n) and modulation frequency (ω).

2.4 Green's function solution to diffusion equation for semi-infinite boundary conditions

In NIRS, the most commonly used model approximate tissue as a homogeneous semi-infinite medium. In order to find the diffusion equation Green's function we have used method of images (figure 2.7). The extrapolated zero boundary condition is satisfied by introducing a negative image point source at $z_s = -(2z_b + l_{tr})$. The fluence rate curve is approximated by its tangent line at z = 0, and the Φ= 0 intercept of this curve is found to occur z = -z_b. Equation 2.6 is the Green's function

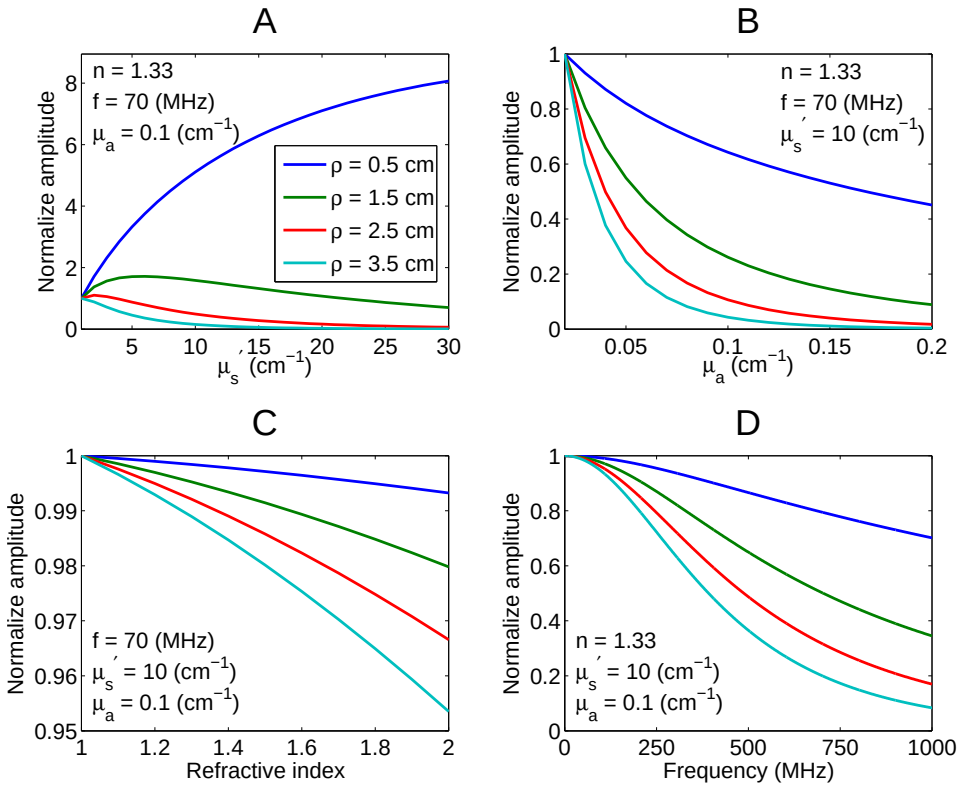

Fig. 2.5 The dependency of amplitude of different source-detector separations on the optical properties of tissue. [A] The relation between amplitude and μ_s': in small values of μ_s' and small source-detector separations increase of μ_s' lead to rise in amplitude. While in larger μ_s' and larger source-detector separations higher μ_s' results to lower amplitude. Figure [B] The inverse relation between absorption in the medium and the amplitude of DPDW in all source-detector separations. [C] The increase of ratio of refraction of the medium to the outside lead to decrease intensity. [D] The amplitude decreases with increase of modulation frequency.

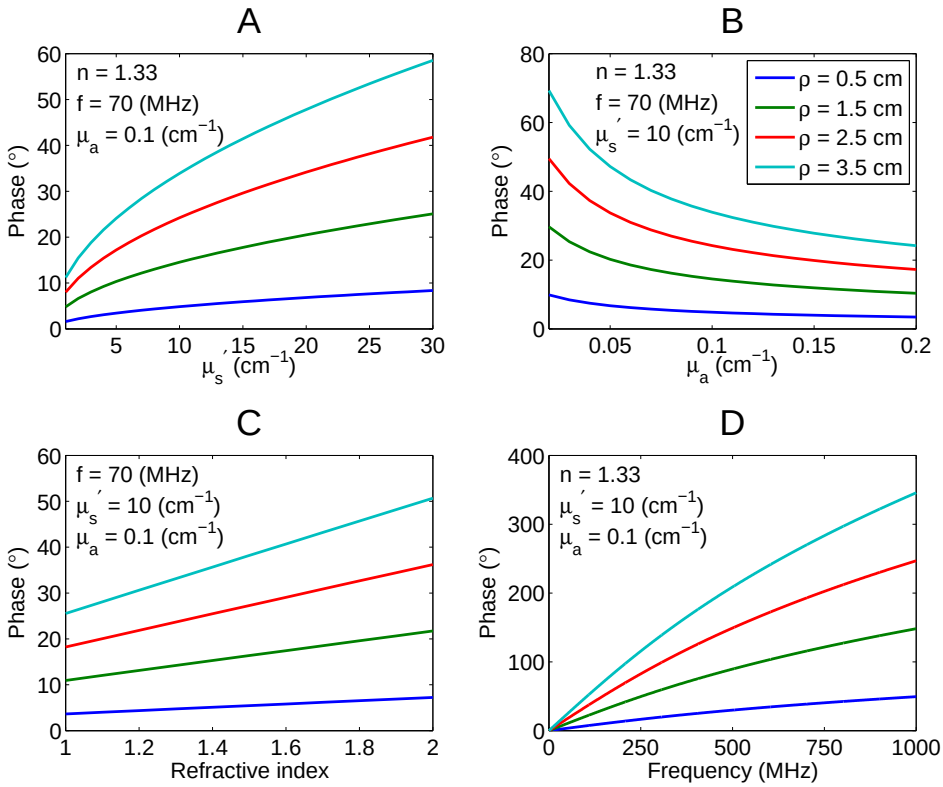

Fig. 2.6 The dependency of phase on the medium optical properties and source modulation frequency over different source-detector separations. [A] Phase has direct relation with the reduced scattering coefficient (μ_s') of the medium. [B] There is a reverse relation between phase and the absorption coefficient of the medium. [C] Medium with higher index of refraction causes larger phase values. [D] DPDWs with higher source modulation frequency have larger phase values.

solution to diffusion equation for semi-infinite boundary conditions[2].

$$G(\rho) = \frac{1}{4\pi}[\frac{exp(-kr_1)}{r_1} - \frac{exp(-kr_b)}{r_b}] \tag{2.6}$$

where:

$$\begin{aligned} r_1 &= \sqrt{\rho^2 - {l_{tr}}^2} \\ r_b &= \sqrt{\rho^2 + (l_{tr} + 2z_b)^2} \\ l_{tr} &= \frac{1}{{\mu_s}'} \\ z_b &= 2l_{tr}\,\frac{1 + R_{eff}}{1 - R_{eff}} \\ k &= \sqrt{\frac{(\mu_a v - iw)}{D}} \\ D &= \frac{\nu}{(\mu_a + {\mu_s}')} \end{aligned}$$

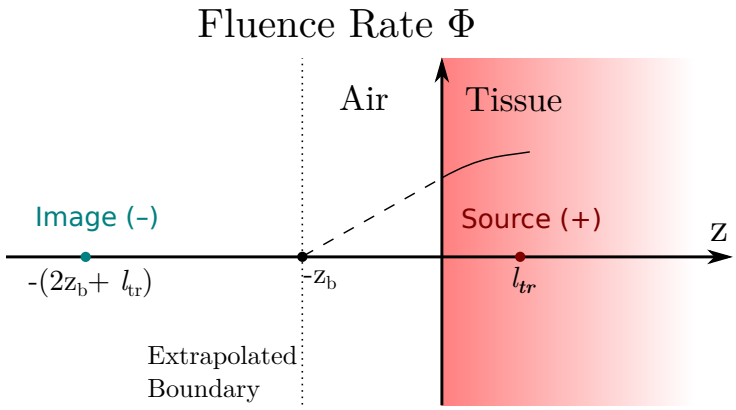

Fig. 2.7 The extrapolated zero boundary condition is satisfied by introducing a negative image point source at $z_s = -(2z_b + l_{tr})$. The fluence rate curve is approximated by its tangent line at z = 0, and the Φ= 0 intercept of this curve is found to occur z = -z_b.

Here ρ is distance between source and detector, w is the intensity modulation frequency. l_{tr} is the mean distance that photon propagation direction becomes randomize. z_b is the extrapolated zero boundary and D is the photon diffusion coefficient. R_{eff} is the effective reflection coefficient to account for the index mismatch between tissue and air.

The absolute value of photon fluence is corresponding to amplitude and angle part is the detected phase. Equation 2.6 can be fit exactly, but in the approximation of $\rho \gg (l_{tr} + 2z_b)$. In this case the solution simplifies to:

$$U(\rho) = A(\rho)e^{i\theta(\rho)},$$

$$\ln(\rho^2 A(\rho)) = -k_r\rho + \ln A_0, \tag{2.7}$$

$$\theta(\rho) = -k_i\rho + \theta_0. \tag{2.8}$$

The equations 2.7 and 2.8 makes it possible to fit exactly for k_i and k_r and calculate μ_a and ${\mu_s}'$. Figure 2.8 shows that the slope of $\ln(A(\rho)\rho^2)$ versus ρ in semi-infinite boundary conditions is k_r. Similarly, the slope of phase versus ρ is k_r. In CW measurements where we do not have information about the phase by exact fitting for k_r one can have information about effective attenuation coefficient (μ_{eff}).

Patterson et al. [147] described the analytical solution of the diffusion equation (equation 2.1 for TRS. They have shown that the reflectance in a semi-infinite homogeneous medium for the time domain is described by:

$$R(t,\rho) = (4\,\pi\,D\,\nu)^{-\frac{3}{2}}\,{\mu_s}'^{-1}\,t^{-\frac{5}{2}}\,exp\left[-\mu_a\,\nu\,t\right]\,exp\left[-\frac{\rho^2 + {\mu_s}'^{-2}}{4\,D\,\nu\,t}\right]. \tag{2.9}$$

Photon penetration depth In experiments the detection of light can be in transmission or reflection geometry. In all of my studies reported

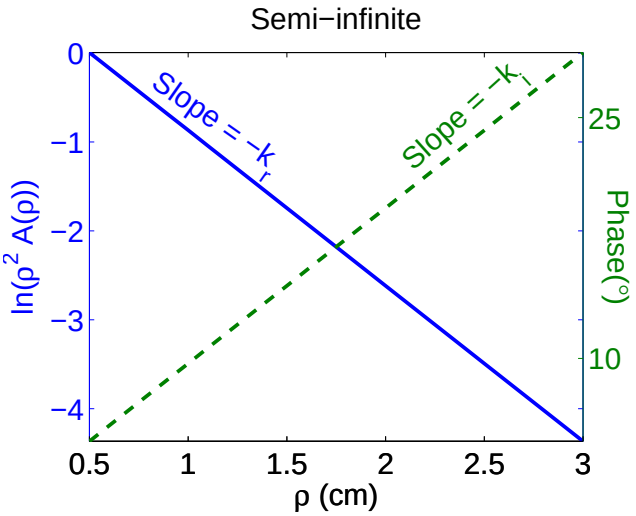

Fig. 2.8 The phase (green dashed line) and $\ln(A(\rho)\rho^2)$ (blue solid line) are plotted as the function of distance from the source in semi-infinite boundary condition. The slopes reveal $-k_i$ and $-k_r$ (effective attenuation coefficient, μ_{eff}), from which μ_a and $\mu_s{}'$ can be calculated using equations 2.4 and 2.5.

through this manuscript, reflection geometry has been deployed. In the reflection geometry the probed medium has a "banana" shape which is demonstrated in figure 2.9. The simulated medium has $\mu_a = 0.1$ cm^{-1}, $\mu_s{}' = 10$ cm^{-1} and $\rho = 2.5$ cm. As a rule of thumb, the mean light

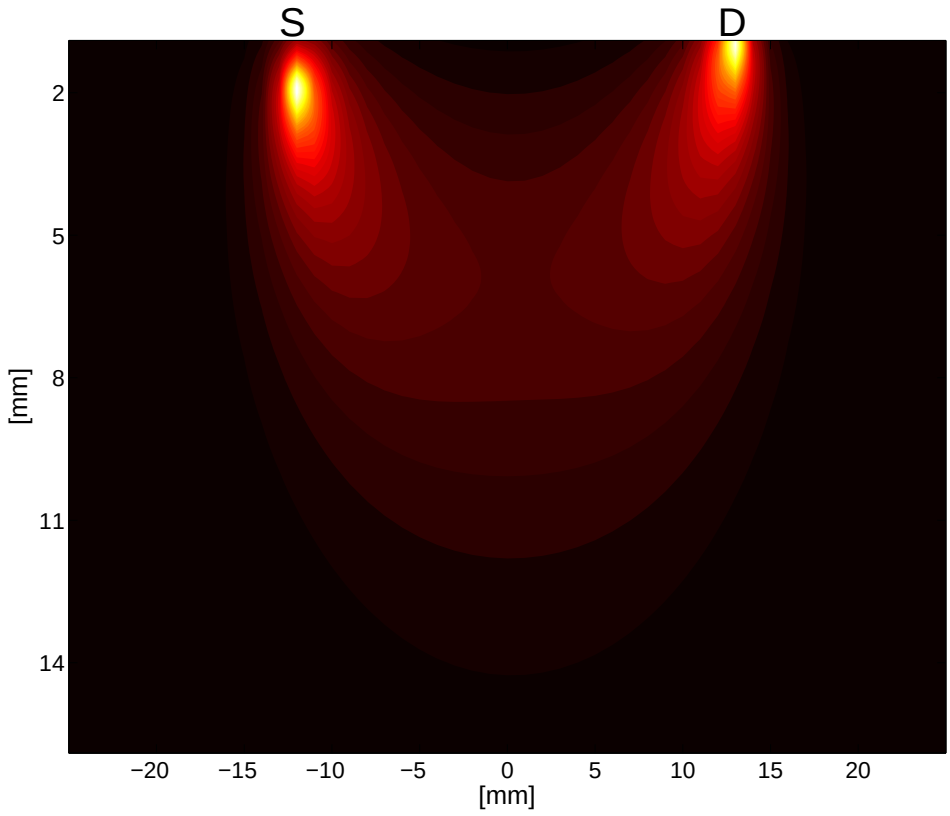

Fig. 2.9 The "banana patterns" showing the sampled volumes in the reflection geometry. As a rule of thumb, the mean light penetration depth in the reflection geometry is in the order of half of source-detector separation ($\rho/2$). The simulated medium has $\mu_a = 0.1$ cm^{-1}, $\mu_s{}' = 10$ cm^{-1} and $\rho = 2.5$ cm.

penetration depth in the reflection geometry is in the order of half of

source-detector separation ($\rho/2$). In other words, the larger the source-detector separation, the deeper volume is probed [163]. In figure 2.10, the probability of detecting photons below certain depths is shown. The absorption coefficient (μ_a) of the simulated medium is 0.1 (cm^{-1}), and reduced scattering coefficient (μ_s') is 10 (cm^{-1}). It illustrates that larger optode distances have higher probability of photon detection in deeper volumes. For instance, in optode distance of 0.5 cm, just less than 2% of detected photons traveled deeper than 1 cm, in optode distances of 5 cm this quantity is 40%.

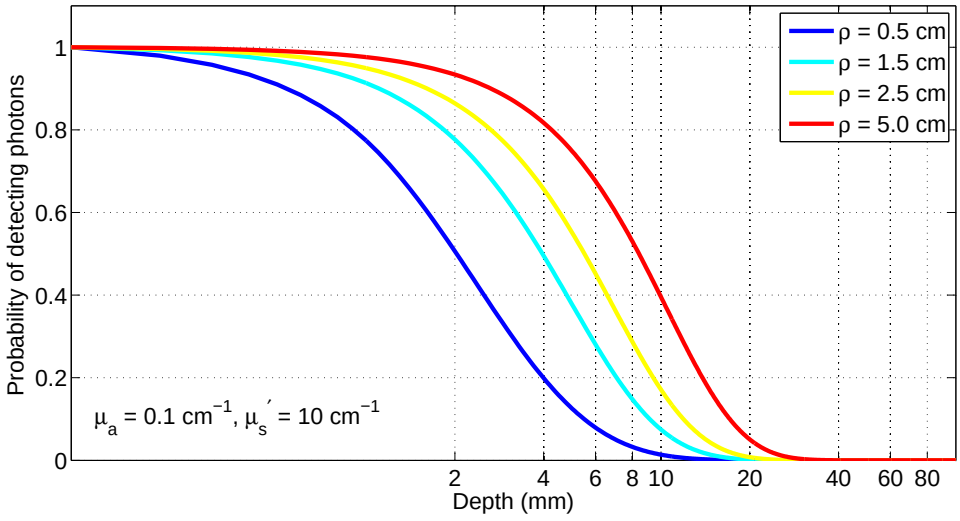

Fig. 2.10 The probability of detecting photons below certain depths. The probability function is presented for optode distances from 0.5-5 cm.

2.5 Multi-wavelength spectroscopy for determination of tissue chromophore concentrations

The tissue absorption depends linearly on the concentrations of tissue chromophores. In particular, the wavelength-dependent absorption coefficient is given by equation 2.10.

$$\mu_a(\lambda) = \sum_{i}^{nc} \epsilon_i(\lambda) c_i \tag{2.10}$$

The sum is over the different tissue chromophores. and nc is the number of chromophores assumed. $\epsilon_i(\lambda)$ is the wavelength-dependent extinction coefficient of the i^{th} chromophore obtained from the literature [164], and c_i is the concentration of the i^{th} chromophore. By equation 2.10 one can calculate concentration of oxygenated hemoglobin and deoxygenated hemoglobin (c_{HbO_2} and c_{Hb}). The total hemoglobin concentration (THC) is the sum of oxygenated and deoxygenated hemoglobin, i.e:

$$THC = c_{HbO_2} + c_{Hb}. \tag{2.11}$$

The blood oxygen saturation can be determined by:

$$SO_2 = \frac{c_{HbO_2}}{THC} \times 100. \tag{2.12}$$

Oxygen saturation and hemoglobin concentration are important biormakers in oncology, brain studies, etc. [165].

2.6 Diffuse correlation spectroscopy (DCS)

DCS measures the temporal speckle fluctuations of the scattered light, that is sensitive to the motions of scatterers such as red blood cells (RBCs) which in turn could be used to estimate microvascular blood flow [24, 25, 29, 166–168]. [2, 26–28]. The motional dynamics of the medium can be determined by measurement of intensity autocorrelation from which the electric field autocorrelation function (G_1) can be derived. The fluctuations of the speckles are primarily due to movement of scatterers. Therefore, faster motion of the scatterers can be indicated by faster fluctuations (i.e., more rapid decay of the intensity temporal autocorrelation function). The Green's function solution of the correlation diffusion equation for semi-infinite boundary conditions is [2]:

$$G_1(\rho,\tau) = \frac{3\mu_s{}'}{4\pi}[\frac{exp(-K(\tau)r_1)}{r_1} - \frac{exp(-K(\tau)r_b)}{r_b}] \tag{2.13}$$

Where τ is delay time, r_1 and r_b are described in section 2.4 and $K(\tau)$ is:

$$K(\tau) = \sqrt{3\mu_a\mu_s{}' + 6\mu_s{}'^2\kappa^2\alpha D_b\tau}. \tag{2.14}$$

α represents the fraction of photon scattering events that occur from moving particles in the medium, κ is the wave-number of light in the medium: $2\pi/\lambda$. DCS instrumentation measures the intensity temporal autocorrelation function, while the correlation diffusion equation applies to the electric field temporal autocorrelation function. To compare theory with experiment, the normalized intensity autocorrelation function (g_2) must be related to the normalized electric field temporal autocorrelation (g_1). This connection is through Siegert relation (equation 2.15).

$$g_1(\tau) = \sqrt{\frac{g_2(\tau) - 1}{\beta}} \tag{2.15}$$

β is a constant determined primarily by the collection optics of the experiment. β is approximately equal to $\frac{1}{N}$ where N is the number of detected speckles/ modes. In most of DCS studies non-polarized sources (vertical and horizontal modes) and single mode fibers are used to collect the diffused light and in this case $\beta \sim 0.5$ [169]. In experimental data β can be measured from the g_2 when τ is near to zero. Thus, g_1 is derived from the experimentally measured g_2 , and K^2 is determined by fitting to the temporal decay of g_1 (for a given source-detector separation). This information in addition to optical property information (μ_a, $\mu_s{}'$, n) provide us with determination about mean square displacement of scatterers ($< \triangle r^2(\tau) >$). The brackets represent time-averages (for experiments) or ensemble averages (for calculations). Thus by measuring the temporal fluctuations of scattered light, one obtains quantitative information about the particle motions. For the case of Brownian motion, $< \triangle r^2(\tau) >= 6D_b\tau$ and for random flow, $< \triangle r^2(\tau) >=< \triangle V^2 > \tau^2$. Here, D_b is the particle diffusion coefficient and $< \triangle V^2 >$ is the second moment of the particle speed distribution. In the study of blood flow in the microvasculature the random flow model seems the trivial choice for the dynamics of RBCs. In practice, it has been found [32–38, 46] that the Brownian model,$< \triangle r^2(\tau) >= 6D_b\tau$, fits the observed correlation decay curves better over a wide range of tissue types. It has been demonstrated in several DCS measurements that the fitted parameter αD_b (from the Brownian model) correlates well with blood flow values measured by other modalities [32–45]. Therefore we have defined αD_b as the blood flow index (BFI).

Figure 2.11 demonstrates the effect of different parameters on the shape of autocorrelation curves. This plot suggest that error in assumption of tissue μ_a or $\mu_s{}'$ will introduce error in fitted BFI [170].

Noise model for DCS: In the following chapters we have simulated DCS measurements. For numerical simulations we have added noise to

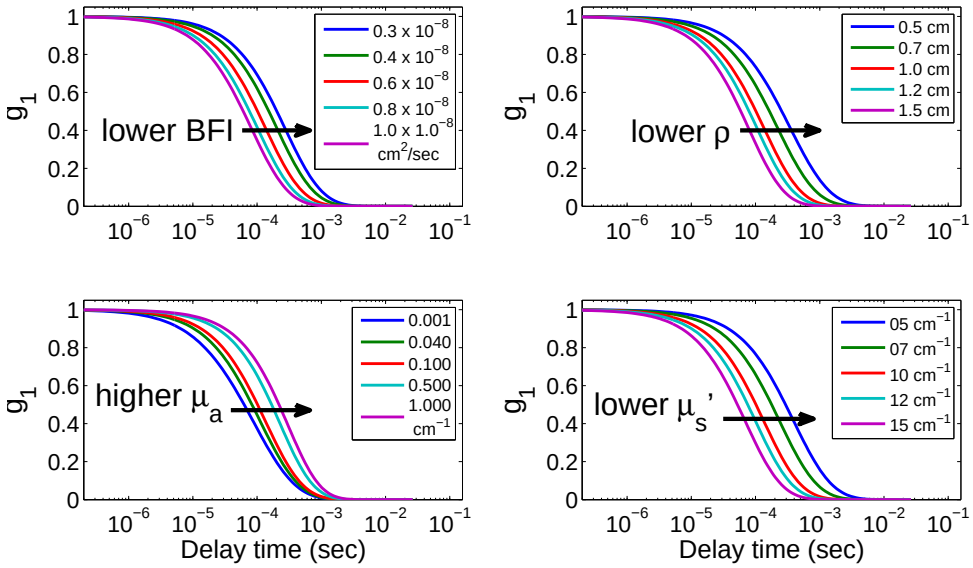

Fig. 2.11 Effect of different parameters on the shape of field autocorrelation curve. Decrease in blood flow index (BFI), source-detector separation (ρ) and scattering coefficient ($\mu_s{}'$) as well as increase in absorption coefficient (μ_a) will cause higher correlation therefore later drop of AC curve.

theoretical intensity autocorrelation. The noise model for DCS measurements is developed by Zhou et al. [76]. It has adapted the noise model for fluorescence correlation spectroscopy developed by Koppel [171]. In a DCS experiment, the normalized field autocorrelation function decays exponentially ($g_1(\tau) = e^{-\Gamma\tau}$). The optical/mechanical properties of medium and experimental conditions define the value of Γ. The standard deviation ($\sigma(\tau)$, noise) of the measured intensity AC, $g_2(\tau)$, at each delay time (τ) is estimated to be:

$$\begin{aligned}\sigma(\tau) &= \sqrt{T/t}\left[\beta^2\frac{(1+e^{-2\Gamma T})(1+e^{-2\Gamma\tau})+2m(1-e^{-2\Gamma T})e^{-2\Gamma\tau}}{1-e^{-2\Gamma T}}\right]^{\frac{1}{2}} \\ &+ \left[2<n>^{-1}\beta(1+e^{-2\Gamma\tau})+<n>^{-2}(1+\beta e^{-\Gamma\tau})\right]^{\frac{1}{2}}. \quad (2.16)\end{aligned}$$

In equation 2.16, T is the correlator bin time interval, m is the bin index corresponding to the delay time τ . In our correlator the bin time interval is T = 200 ns for the first 16 channels and is doubled every 8 channels afterwards. The average number of photons $< n >$ within bin time T (i.e. $< n >= IT$, where I is the detected photon count rate), t is the total averaging time.

Chapter 3

Hybrid broadband NIRS-DCS instrumentation for experimental oncology

3.1 Introduction

Murine models are the most popular *in vivo* models in oncology study and by definition, are an approximation of reality. The major reason that mice are used is the similarity of mouse and human genetic and this greatly increased the value of animal models for research on human disorders specially cancer [111].

Genetically engineered mouse models have significantly contributed to the understanding of cancer biology. They have proven to be useful in clinical models in which novel therapeutic strategies are tested [112, 113].

Cancer is abnormal, uncontrolled production of cells in a part of body. The high proliferating activity of malignant tissue demands more oxygen and nutrition. To fulfill this demand, cancerous tissue develops angiogenesis. Angiogenesis is the proliferation of a network of blood

vessels that penetrates into cancerous regions, supplying nutrients and oxygen and removing waste products [172–174]. The high metabolism and vascular supply make a contrast between cancerous and normal tissue hemodynamics.

By taking advantage of near infrared spectroscopy (NIRS) ability to map oxygen saturation and blood volume as well as diffuse correlation spectroscopy (DCS) for blood flow measurements, (look at section 2.5), we can study microvascular physiology noninvasively as opposed to the most common imaging modalities that allow probing of tumor morphology [6]. For example, metastatic cancers (when a cancer spreads from its original site to another area of the body, it is termed metastatic cancer), in general, have higher metabolism and higher blood volume and by NIRS and DCS techniques we can find tissues with higher metabolism and distinguish metastatic tumors from benign ones.

Furthermore, monitoring the hemodynamics changes induced by therapies can provide valuable information about the outcome of therapy. This information can be used to personalize the therapeutic plan for each patient. Many techniques have aimed to monitor the cancer therapies [175–178]. This aspect of my research focuses on monitoring of cancer therapies where we postulate that physiological changes could be observed prior to morphological changes.

3.1.1 Cancer therapies and optimizing their efficiency

The type of cancer therapy depends on the type, stage, and location of cancer as well as several other parameters. Considering condition of patient and cancer usually a combination of therapies will be applied. In cancer treatment the complete removal of the cancer without damage to the rest of the body is the goal of treatment. Sometimes this can be accomplished by surgery, but the propensity of cancers to invade

adjacent tissue or to spread to distant sites by microscopic metastasis often limits its effectiveness; chemotherapy, radiotherapy, phtodynamic therapy are prominent treatments.

Chemotherapy: It uses drugs to stop or slow the growth of cancer cells to shrink the tumors. It is often applied before surgery (neoadjuvant) or after radiation therapy or surgery to destroy remaining cancer cells from radiation therapy or surgery [179–181]. Chemotherapy may have serious side effects such as: anemia (low red blood cell count) [182] which causes lack of oxygen circulating in the body, thrombocytopenia (low platelet count) that may reason bruising or excessive bleeding, neutrogena (low white blood cell count) hair losses, eating and skin problems, etc. While certain cytotoxic side effects can be even life-threatening [183], under-dosing of patients, which may compromise the probability of cure for cancers that are curable with chemotherapy, is not acceptable. Because of the enormous consequences to cancer patients, maximizing the efficacy of chemotherapy is of prime importance.

Radiation therapy: It uses high energy radiation: X–ray, gamma, neutrons, protons, etc. to kill cancer cells and shrink tumors [184, 185]. It has two kinds:

1. internal: it has internal source of radiation like radioactive material.

2. external: it has external source of radiation like X-ray.

Unfortunately, early and late toxicity limits the deliverable intensity of radiotherapy, and might affect the long-term health related quality of life of the patient and also side effect such as: diarrhea, hair loss in the treatment area, mouth problems, nausea and vomiting, sexual changes, Swelling, trouble swallowing, urinary and bladder changes. All these issues arise an importance to optimize the efficacy of therapy [186].

Photodynamic therapy (PDT): Although this method is still mainly experimental, it is of particular interest for a photonics research group since it uses light activated drugs to destroy cells [187, 188]. In this method photosensitizer is injected to the patient. The interaction between laser light and photosensitizer makes excited singlet oxygen which can destroy cells. There are important key components that need to be optimized, for example, the drug dose and the activating light dose. It is generally a difficult problem to predict how much light would be delivered into deep tissues.

Cancer therapy monitoring and enhancement Here I outline one of our key goals which is to monitor cancer therapy to understand its fundamental effects on different types of tumors and physiological conditions as well as to suggest potential strategies that could then be tested on humans to optimize the treatment. Let's take PDT as an example. The micro-vasculature is the primary mechanism to delivers the treatment drug to the remote parts of the tissues of interest, but the selectivity (in general, unless some targeting mechanism is used) is low and the drug can kill cancer cells as well as the normal tissue and blood vessels. In fact, the destruction of blood vessels to the cancerous regions is often the goal but it has a side-effect that it may stop the delivery of the drug to the cancer tissue prematurely, hence hindering the treatment. Monitoring the blood flow during the therapy can assist us to control this situation and we can "tune" the therapy so that the blood flow is maintained long enough to ensure adequate delivery of drug to the tumor. Monitoring of microvascular blood flow is possible by means of diffuse correlation spectroscopy. In radiation therapy and PDT, oxygen plays an important role in the therapy effect. Without oxygen, the therapy is not effective and hence local, microvascular, monitoring of the oxygen is important. We can continuously measure the HbO_2 concentration by NIRS which is assumed to be an indicator of the available

oxygen locally. In the work by Yu et al. [37], it has been shown that by finding the optimum blood flow patterns during therapy and providing a feed-back mechanism to alter the light fluence/duration, we may be able to improve the efficiency of therapy. Since then similar effects have been observed in other tumor models and even was suggested in human trials of PDT [106, 109, 110, 131, 132, 142, 189].

3.2 Combination of broadband NIRS and DCS in a single probe

The murine tumors are small in size ($<$ 1 cm in diameter) (figure 3.1) therefore to perform measurement on them the maximum distance between source and detector can not be more than few millimeters (5 mm). Although time resolved spectroscopy (TRS) and frequency domain (FD) contain higher amount of information (look at figure 2.1), in such small source-detector separation the broadening of pulse in TRS and phase shift in FD is small and is difficult to be detected by current instrumentation. Therefore, we have chosen multi-distance continuous wave (CW).

In single wavelength CW measurement one can not decouple μ_a and $\mu_s{}'$, and we can just measure effective attenuation coefficient (which is called k, k_r or μ_{eff}). In order to decouple μ_a and $\mu_s{}'$ we have used broadband light source [37, 43, 58, 69, 70, 91, 92, 95, 97, 105–109, 127–129, 131, 133–135, 137]. By broadband NIRS we can measure optical properties of tissue (μ_a, $\mu_s{}'$) as well as concentration of oxygenated hemoglobin (c_{HbO_2}), deoxygenated hemoglobin (c_{Hb}), total hemoglobin concentration (THC) and oxygen saturation (SO_2) (for more details look at section 2.5). Diffuse correlation spectroscopy measures blood flow in microvasculature. Knowing blood flow changes as well as oxygen saturation and THC, one can measure changes in metabolism which is

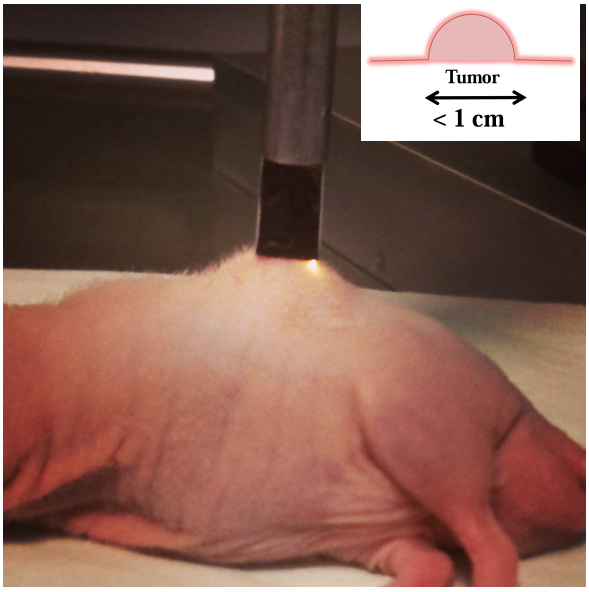

Fig. 3.1 An anesthetized nude mouse with a renal tumor and the optical probe on top of the tumor. The tumor is small in size ($<$ 1 cm in diameter) and the source-detector separation in the optical probe should be less than 5 millimeters.

an important parameter for *in-vivo* studies.

3.3 Broadband near infrared spectroscopy

In the last decades several groups have applied broadband NIRS for experimental oncology in small animals.Weersink et al. [108] are one of the first groups who have used self-calibrating probe for broadband NIRS study. To increase the speed of measurements some groups have taken advantage of two-dimensional CCD cameras for gathering simultaneous spectral and spatial information [105, 131]. The goal here was to develop an instrument with high information content (i.e. high quantification) while being easy to operate by a small probe that resembles a "pen" (figure 3.7). It should be operated by biomedical researchers. It takes advantage of white light and multi-track spectrometers for NIRS to acquire a relatively complete spectrum from multiple separations [37, 43, 58, 70, 92, 95, 97, 105–109, 127–129, 131, 133]. The goal is to acquire multi-spectral, multi-distance measurements to be used in an algorithm that uses both these aspects for both NIRS and DCS to recover the optical properties and blood flow accurately. Figure 3.2 shows that the light source is a broadband lamp. The light is delivered to the tissue through multi-mode fibers and the diffuse light is collected in different distances from the source to a 2D spectrometer. The information about intensity on each wavelength/distance is transformed a computer for post-processing.

Light Source: We want to work in physiological window (650-1000 nm), and we need a source which does not have any narrows peak in this range. For this purpose we have chosen Fused Silica Collimating Quartz Tungsten Halogen (QTH) Lamp. The chosen light is a 250W fiber illuminator from Oriel Instruments- Newport Corporation (CA,

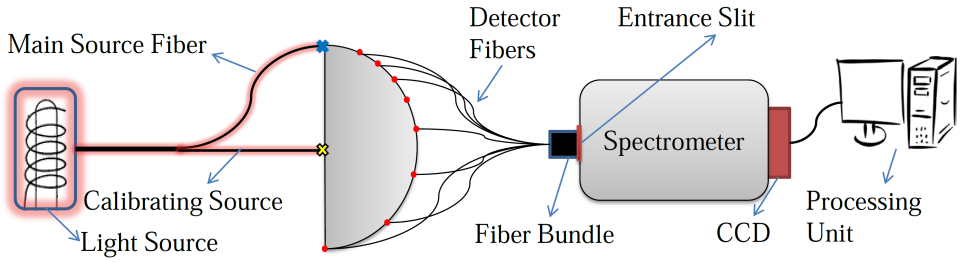

Fig. 3.2 The schematic of white-light device.The light source is a broadband lamp. The light is delivered to the tissue through multi-mode fibers and the diffuse light is collected in different distances from the source to a 2D spectrometer. The information about intensity on each wavelength/distance is transformed to a computer for post-processing.

USA). It has an internal shutter which enables us to block white-light when we want to work with the DCS laser.

Spectrometer and CCD: We planned to image eight fibers on to the CCD (rows) and many wavelengths (columns). Therefore we need a 2D CCD, i.e. spatial separation of fibers will be on one dimension of CCD and spectral separation in the other. As the detected light from point which are far from source is very weak we need to have high quantum efficiency and sensitivity as well as adequate dynamic range. Back illuminated CCDs allow incident photons to interact directly with the photosensitive silicon substrate without having to penetrate an electrode layer. This design results in increased sensitivity and quantum efficiency. But, in NIR, back illuminated CCDs experience reflections between their front and back surfaces leading to etaloning. A technique to reduce the etaloning effect is named excelon. With excelon CCDs not only the effect of etaloning will be reduced, but also the sensitivity and quantum efficiency will increase. Therefore our final choice for CCD was an excelon back illuminated CCD whose peak of quantum efficiency was

95% at 700nm. (PIXIS: 400B-eXcelon , Princeton Instrument[1]). This CCD is a 1340 × 400 imaging array, with 20 × 20 microns pixels. We can improve the resolution of spectrometer by increasing the intensity of grooves of grating. But grating with higher groove intensity can cover narrower spectral range, so there is a compromise between range of covered spectra and resolution. Resolution also depends on size of entrance slit. Smaller slits makes higher resolution but the light which can enter is lower (lower level of signal). With bigger grating we can have better spatial and spectral separation. However, the cross-talk between fibers on CCD was also an important parameter for us. We need to have the cross talk less than 1% for 8 fibers with 200μm cores. Considering all these parameters our final choice was Acton InSight-EPF from Princeton instruments with 150 g/mm grating which gives us a resolution about 5 nm covering 545-1055 nm.

3.4 Diffuse correlation spectroscopy

In this setup, DCS is employed for the measurement of blood flow. It has a single longitudinal mode laser as source(DL785-120-SO, 120mW, 785nm from Crystalaser); the coherence length (>15 m) of the laser is much longer than a typical photon path length. The laser light is delivered to the tissue through a multimode fiber with a core diameter of 200 μm (NA = 0.22). Due to necessity to detect single speckle, DCS uses single mode fibers of 5.8 μm core diameters for collection. Photon counting avalanche photodiodes (APDs) are used as detectors (SPCM-AQRH-14-FC, Pacer Internal) whose output is fed to a digital correlator (Correlator.com, NJ, USA) to obtain the autocorrelation functions. The schematic of DCS device is shown in figure 3.3.

[1]Data is retrieved from Princeton Instrument website. Last access on 30/July/2014:
“http://www.princetoninstruments.com/products/speccam/pixis/”.

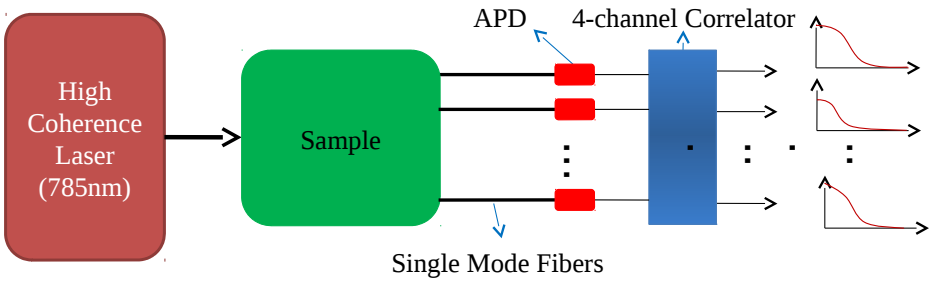

Fig. 3.3 The schematic of DCS device. A high coherent laser light is deployed as the source. The diffused light from the tissue will be delivered to the detectors (avalanche photodiodes) through single mode fibers. A correlator calculates the autocorrelation function of the detected light.

3.5 Design and construction of the hand-held probe

The probe design is based on a rigorous computational simulation which employs a physical model for semi-infinite media as its principal element. The properties of a typical tissue are given as optical properties of media. The desired probe is a semicircle (half a centimeter diameter). There is a source in one end of diameter and also a self-calibration source in the center. The detectors for NIRS are located on the circumference of this semicircle. The simplest way is to distribute all detectors evenly. but as much as we get far from the source, the changes in intensity is smaller; therefore while the first consecutive detectors (nearest detectors to the source) have a lot of difference in detected intensities, last detectors have no measurable difference. Figure 3.4 shows the simulated detected intensity of 8 uniformly distributed detectors whose intensities are calculated by applying the diffusion equation. Using HbO_2 , Hb and water as chromophores.

The positions of the detectors are determined according to several

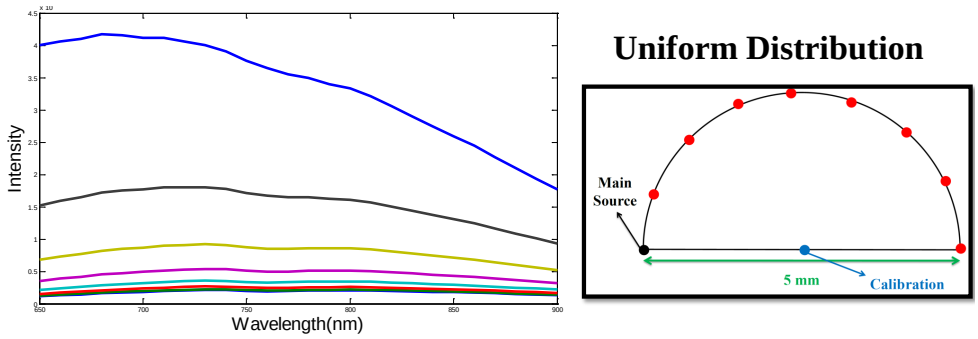

Fig. 3.4 [Left] Simulated detected intensity of 8 uniformly distributed detectors. [Right] The schematic of a probe with uniform distribution of detector.

considerations:

- Photon diffusion equation should be applicable; the distance between source and the first detector should be more than $2l_{tr}$ (l_{tr} is transport mean path).

- The detected intensities should cover the whole dynamic range of the CCD uniformly where the lowest signal level that is allowed should allow for an SNR > 10. For example, in a 16-bit CCD with ~ 500 dark counts the signal from the furthest detector should be more than 5000 counts. While the maximum count in a 16-bit camera is ~ 650000 counts. Therefore the detectors should cover a range between 5000-65000 counts.

- In order to ensure that under all conditions we can separate the changes in intensity due to changes in distance, we allow for 10% deviation due to physiology and noise in time. Therefore, the difference between detected intensities from detectors with increased separation should be more than 10%.

- For practical reasons, we limit ourselves to eight detector positions in order to ensure (with current commercially available hardware) that the inter-fiber cross-talk is less than 1% for ∼200μm detector fibers.

- The distance between following detectors cannot be less than 0.5 mm because of the size of the fibers.

Figure 3.5 illustrates the constraints for the position of detectors.

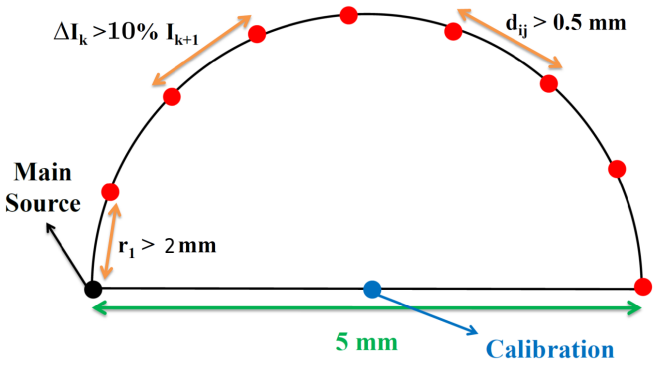

Fig. 3.5 The schematic of desired self-calibrating probe and the constraints on the detector positions.

We then simulate a large (thousands) of positions on a semi-circle using the numerical model and apply the above constraints to find out candidate positions. Their potential is tested by fitting for unknowns from forward simulations including shot-noise, CCD noise, CCD quantum efficiency, source spectrum and dark counts. The detailed description of implemented CCD noise, coupling errors, calibration and fitting data is explained in the following sections. for a range of optical properties. Our simulations have let us that for 8 fibers with source-detector separation 2.5 to 5 mm (2.5, 2.9, 3.2, 3.6, 3.9, 4.3, 4.6, 5.0 mm). The selected detector position satisfying all the above constraints we will have

the detected intensity of ith detector is least 23% more than previous one (i-1)th for average tissue properties. We note that this provides us with a better quality data than simply distributing the detectors evenly along the semi-circle since the diffusing photons are decaying exponentially with distance. Figure 3.6 shows the simulated detected intensity of 8 detector positions satisfying all the desired constraints.

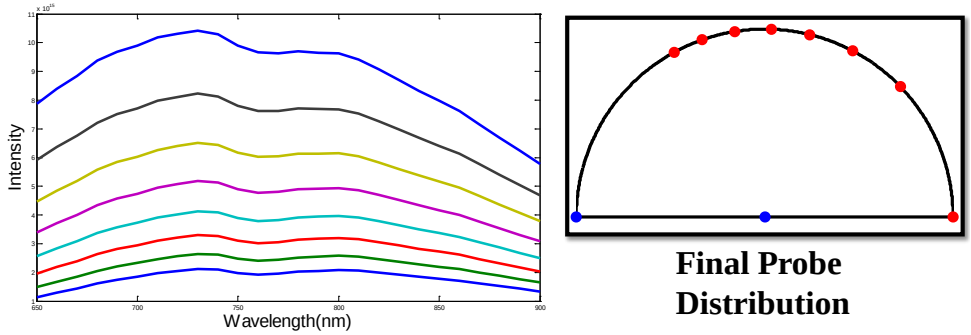

Fig. 3.6 [Left] Simulated detected intensity of 8 detector positions satisfying all the desired constraints. [Right] The schematic of a probe with final distribution of NIRS detectors.

Since we want the DCS and NIRS provide information from the same depth in the tissue, and source-detector separation is the indicator of depth, we have chosen the DCS source-detector separation same as NIRS ones.

As there are 4 APDs in the DCS setup and we need 8 source-detector separations, we have considered two DCS source which shine light in turn and two source positions with 4 detector positions results in 8 source-detector separations. All we need is finding a set of locations for these fibers on the probe such that it retrieves eight source-detector separations of NIRS probe to cover the same volume. Figure 3.7 demonstrates the final design of probe the way it will be located on the tumor.

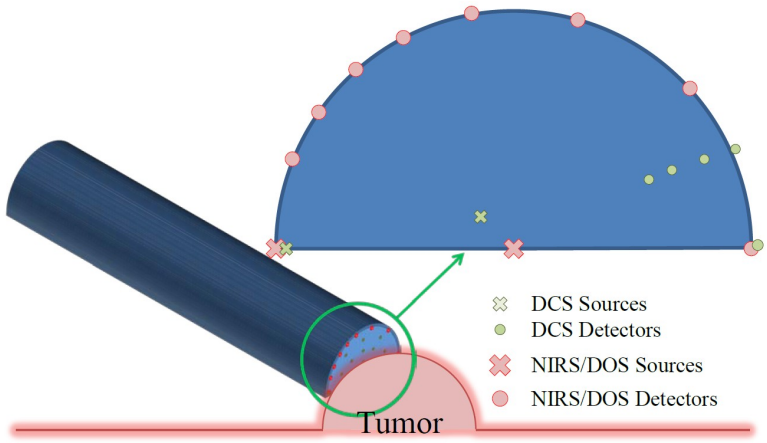

Fig. 3.7 The schematic of hand-held NIRS/DCS probe and the way it will be located on the tumor.

The designed probe was made by Fiberoptic Systems, Inc. (FSI, Simi Valley, CA. USA). The drawing of manufactured probe with all the details can be found in appendix A. Some spare single and multi-mode fibers are implemented in the fabricated probe to be used in case of fiber damage. The 8 NIRS detectors are connected to an 8 to 1 fiber bundle, and the bundle is placed on the entrance of the spectrometer. The bundle is also made by Fiberoptic Systems, Inc. The drawing of manufactured bundle can also be found in appendix A.

Figure 3.8 is a picture of the probe tip. Since the illuminated light to different fibers was not homogeneous they have different brightness. The smaller dots correspond to single mode fibers (DCS detector fibers).

3.5.1 Noise in CCD

Dark noise: Dark current is the relatively small electric current that flows when no photons are entering the device. Physically, dark cur-

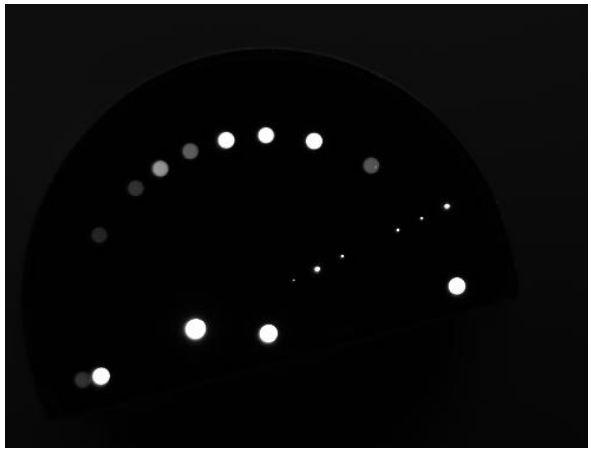

Fig. 3.8 A picture of the probe tip. Since the illuminated light to different fibers was not homogeneous they have different brightness. The smaller dots correspond to single mode fibers (DCS detector fibers).

rent is due to the random generation of electrons and holes within the depletion region of the CCD that are then swept by the high electric field. Dark current can be reduced by cooling. The cooling temperature in our CCD is -75^o C. The typical dark current at this temperature is 0.005 (e^-/pixel/sec).

Read out Noise: The readout noise of the system is due to the readout electronics of the sensor and the analogue to digital converter. Our CCD has 3 electrons readout noise at slow speeds (100 kHz) and at speeds of 2 MHz; readout noise of 12 electrons is typical.

Shot noise: Shot noise is associated with incident photon statistics. It is proportional to square root of number of photons. Shot noise is the main source of noise in this CCD. We can increase the ratio of signal to shot noise by increasing the signal. It is possible by increasing the exposure time or intensity of the light source. Since the dominant

noise in our system is the shot noise, we just consider shot noise in our simulations.

Coupling errors: In the experiments, the inherent imperfections of the fibers and deficiency of contacts between the fiber tips (sources and detectors) and the tissue due to air gaps or surface moisture cause significant errors which are known as "coupling errors" [190]. In this simulation in order to mimic experimental data, computational coupling coefficients, $F^{i,j}(\lambda)$, are introduced as follow (i is detector number and j is source number).

$$F^{i,j}(\lambda) = F_D^i(\lambda)F_S^j(\lambda) \tag{3.1}$$

Where $F_D^i(\lambda)$ is detector fiber coupling coefficient and $F_S^j(\lambda)$ is the source fiber coupling coefficient. The simulated coupling coefficients are obtained by:

$$F_D^i(\lambda) = F_D^i(\lambda)^{min} + F_D^i(\lambda)^{error} \times Rand. \tag{3.2}$$

Where $F_D^i(\lambda)^{min}$ is the minimum coupling error and $F_D^i(\lambda)^{error}$ is the difference between maximum and minimum coupling error. "Rand" is a pseudo-random number between zero and one generated by "rand" function of Matlab (Mathworks Inc, Massachusetts, USA). $F_S^j(\lambda)$ is defined in the same way as $F_D^i(\lambda)$.

Quantum efficiency: The quantum efficiency (QE) of a detector represents its response to different wavelengths of light and is defined as the percentage of photons hitting the photo-reactive surface that will produce an electron–hole pair. In figure 3.9, solid green line shows the quantum efficiency of the detectors (PIXIS: 400 B-eXcelon) which is

used in the setup [2]. In order to have more realistic data, thus, quantum efficiency, as well as CCD noise and coupling errors, should be considered in the simulated intensity. To simulated the detected intensity from each source-detector pair the Poisson noise is added to the theoretical amplitude at a specific source-detector separation (rho) and wavelength (λ). Then the quantum efficiency at λ and coupling coefficient are multiplied to the noise-added amplitude. Equation 3.3 illustrates the formula for intensity simulation. $I_m^{i,j}(\lambda)$ is related to detected intensity in i^{th} detector from j^{th} source.

$$I_m^{i,j}(\lambda) = QE(\lambda)F^{i,j}(\lambda)\ Poiss(G(\rho,\lambda)) \tag{3.3}$$

In equation 3.3 $G(\rho,\lambda)$ is the Green's function solution for diffusion equation in semi-infinite boundary condition (for more details at equation 2.6). Poiss is a random number from the Poisson distribution with mean parameter $G(\rho,\lambda)$. Poiss is produce by "poissrnd" function of Matlab.

Self-calibrating probe Our probe is designed to be self-calibrated by utilizing a center- mounted source for estimating the relative detector coupling coefficients. We need to find the calibration coefficient for detectors $D^i_{calibration}$. For calibrating the detectors, we assume a detector as base detector and calibrate the other detectors with respect to that one. For calibrating with respect to the first detector, the first detector calibration coefficient, $D^1_{calibration}$, can be assumed to be unity or kept as an constant. The self calibrating probe is based on the fact that all the detectors should represent the same intensity when calibrating source is on since they all have the same distance (2.5 mm) from the calibrating

[2]The plots is retrieved from Princeton Instrument website. Last access on 30/July/2014:
"http://www.princetoninstruments.com/products/speccam/pixis/".

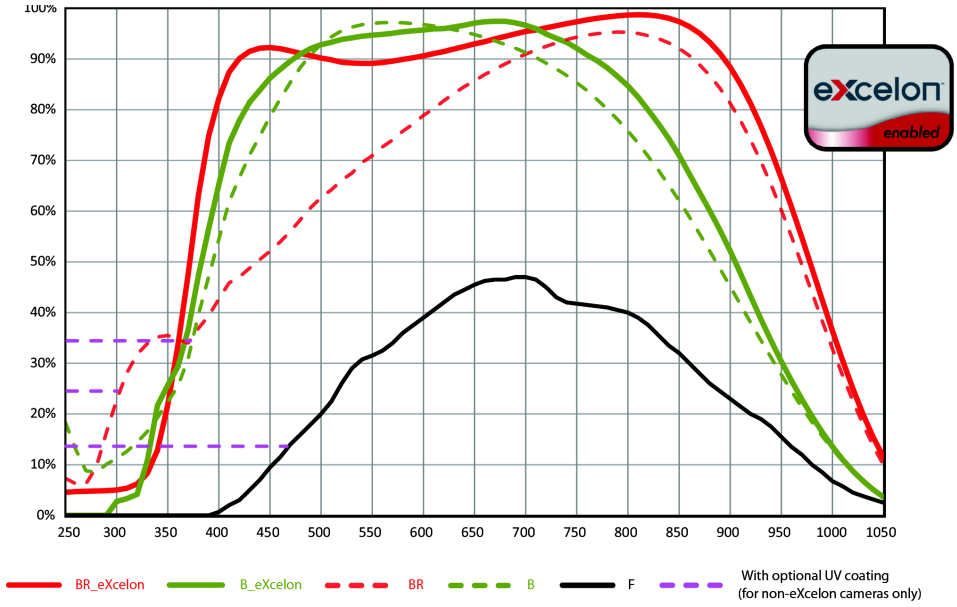

Fig. 3.9 The solid green line is quantum efficiency spectrum of the CCD that we have used in our setup (B-eXcelon). The other colors corresponds to other types of CCD cameras from Princeton Instrument.

source (first source, j = 1). In other words intensities after calibration (I_c^{i1}) should be equal and all equal to the measured intensity of the first detector (I_m^{11}).

$$I_m^{11} = I_c^{i1} = I_m^{i1} \times D^i_{calibration}$$

$$D^i_{calibration} = I_m^{11}/I_m^{i1} \tag{3.4}$$

Figure 3.10 demonstrates the effect of calibration on the measured values. All values are normalized by the first detector to cancel out the source term (I/I_{ref}). Red circles represent normalized intensities before calibration over different source-detector separations. The red circles do not follow the exponential decay. The blue triangles are the calibrate normalized intensities and they have a good agreement with the theory (fitted curve).

Figure 3.11 demonstrates how calibration improves the quality of fitting over a wide range of wavelengths (600-1000 nm) for seven source-detector separations. Similar to figure 3.10 all values are normalized by the reference detector (I/I_{ref}) to cancel out the source term. On the left the normalized intensities before calibration over wavelength do not follow the theory while the right figure shows the calibration improves the agreement of measurement and theory.

3.6 Data fitting for NIRS setup

The output of NIRS setup is the detected intensities over wavelength and source-detector separation. We go through the following procedure to obtain concentration of oxy- and deoxy- hemoglobin in *in-vivo measurements*. The intensities in all detector fibers from the main source, I_{main} were first calibrated using the calibration factors obtained from calibration source (Look at equation 3.4). The calibrated intensities

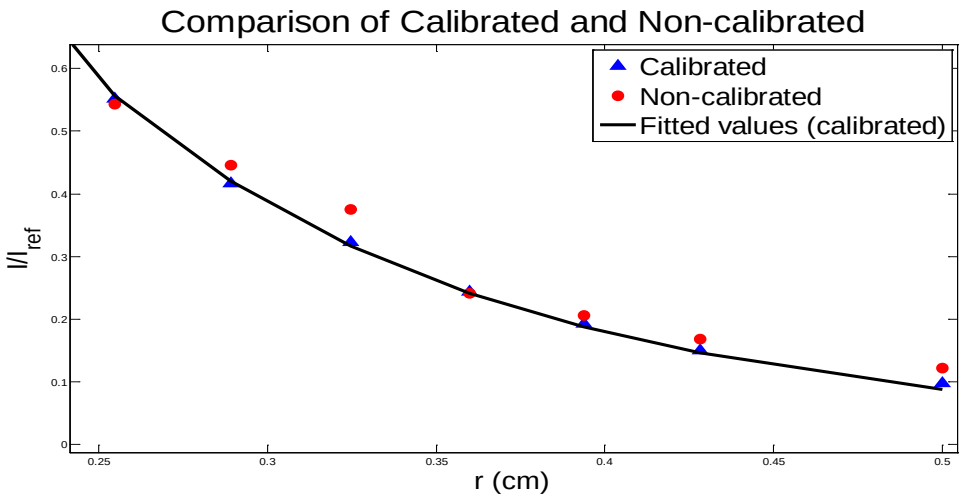

Fig. 3.10 The effect of calibration on the measured values. All values are normalized by the reference detector (I/I_ref) to cancel out the source term. Red circles represent normalized intensities before calibration over different source-detector separations. The red circles do not follow the exponential decay. The blue triangles are the calibrate normalized intensities and they have a good agreement with the theory (fitted curve).

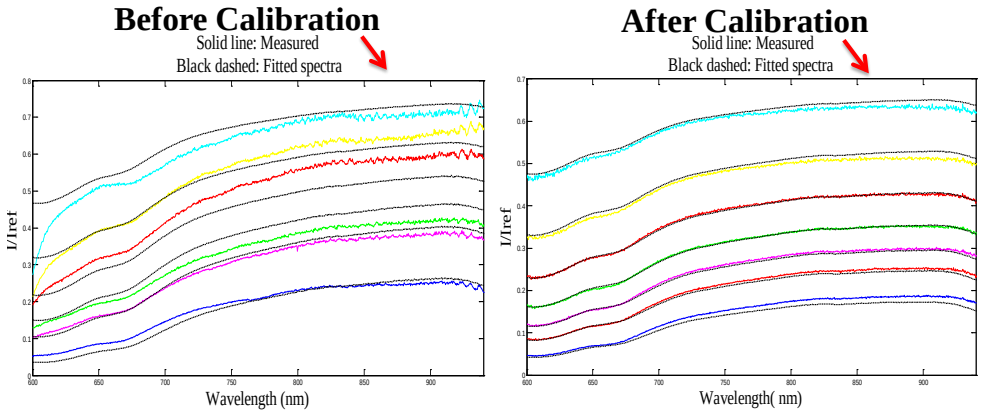

Fig. 3.11 The effect of calibration on the quality of fitting over a wide range of wavelengths (600-1000 nm) for seven source-detector separations.. All values are normalized by the first detector to cancel out the source term (I/I_ref). [Left] The normalized intensities before calibration over wavelengths do not follow the theory. [Right] The calibration improves the agreement of measurement and theory.

This adjusted light intensity, $I(\rho, \lambda)$, at a distance ρ from the main light source is proportional to the Green's function solution for diffusion equation in semi-infinite boundary condition (for more details look at equation 2.6). It has been shown that the scattered spectrum can be fitted to the effective particle size and number density, under the assumption of Mie scattering model. Alternatively, the spectra is thought to fit to a Mie-like spectra with some Rayleigh scatter influence [191, 192].

$$\mu_s{}' = A_1(\lambda)^{-b} + A_2(\lambda)^{-4} \tag{3.5}$$

The absorption coefficient μ_a is assumed to be the sum of the absorption coefficients for oxygenated and deoxygenated hemoglobin (610–800 nm from [193], 800-1000 nm from [194]) and water (from [195]) times their concentrations c_i (more details are available in section 2.5). Numerical fitting was done for A_1, A_2, b and c_i in the wavelength range 610

– 1000 nm for the ratio of the Green's functions of two fibers at the same time, $G(A_1, A_2, b, c_i, \rho_0)/G(A_1, A_2, b, ci, \rho)$. The four short separations (2.5, 2.9, 3.2, and 3.6 mm) were used for ρ_0 and the four longest (3.9, 4.3, 4.6, and 5.0 mm) for ρ. The numerical fitting was done in Matlab using a nonlinear least square method (LSQNONLIN with Levenberg-Marqardt algorithm).

3.7 Test and validation by phantom and *in-vivo* measurements

Test and validation by liquid phantom measurement: The function of the device and data analysis is validated by various tissue simulating phantom measurements. Figure 3.12 shows the results of a test on liquid phantom. The phantom is consist of water (1.9 liters) of lipofundin [196] (for the scattering) and dark green Ecoline ink (for absorption).

μ_a of diluted dark green Ecoline ink at 685 nm was measured by absorption spectroscopy and its absorption is $\sim 5.3\ cm^{-1}$. μ_a of water at 685 nm is $\sim 0.0052\ cm^{-1}$. By lipofunid titration we increased the concentration of scatterers in the medium which is expected to have direct relation with the $\mu_s{}'$ of the phantom. The titration causes volume increase which reduces the concentration of ink that lead to slightly lower μ_a. We have measured changes $\mu_s{}'$ as well as small changes in μ_a very precisely. Figure 3.12 shows the agreement of measured μ_a and $\mu_s{}'$ with the changes in ink and lipofundin concentrations.

Test and validation by *in-vivo* measurement: After successful validation on phantoms, we moved the device to animal facility of IDIBELL (Instituto de Investigación Biomédica de Bellvitge) for the measurement on the murine tumors. In the last step of validation we per-

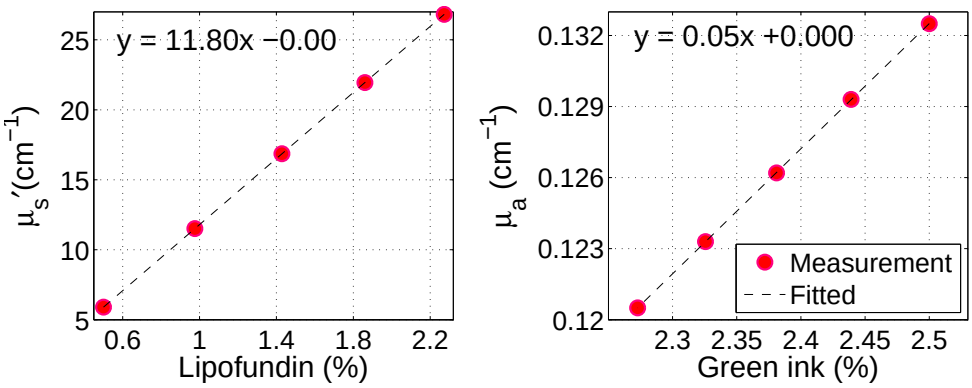

Fig. 3.12 The agreement of measured μ_a and μ_s' with the changes in ink and lipofundin concentrations in a liquid phantom. [Left] measured μ_s' increases linearly by increase of lipofundin concentration. [Right] μ_a decreases linearly by decrease in ink concentration. The measured value of absolute μ_a is in agreement with the absorption spectroscopy value.

formed a thigh cuff occlusion on a mouse to monitor the hemodynamics changes due to occlusion. Figure 3.13 shows the procedure of cuff and the location of probe on the mouse's thigh.

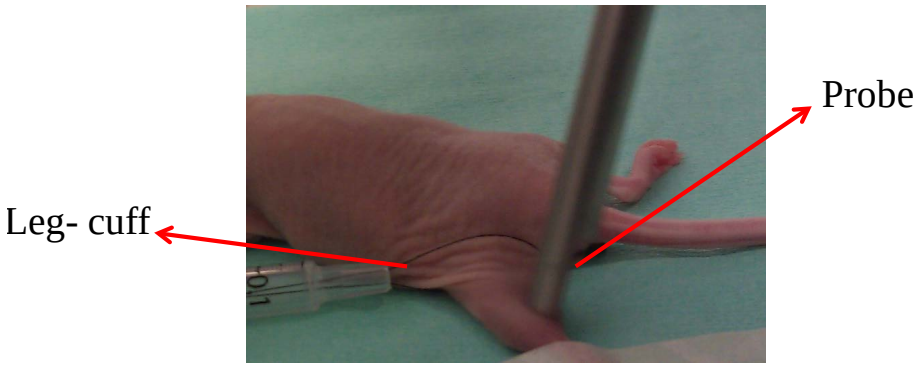

Fig. 3.13 The procedure of arterial thigh cuff occlusion and the location of probe on the mouse's thigh.

Figure 3.14 shows the hemodynamics respond to the arterial cuff occlusion on a mouse thigh. On the left side, the changes in relative blood flow is demonstrated. As expected by applying occlusion blood flow has a sharp drop and afterwards it stays constant. As it has been observed before [33, 119], there is an over shoot of blood flow caused by the release of occlusion. Figure 3.14-right shows the response of blood oxygen saturation to the cuff occlusion. After full occlusion (first dotted red line). Oxygen saturation drops gradually as expected by applying occlusion since the blood flow in the tissue will be restricted and tissue does not receive oxygenated hemoglobin. Tissue consumes the remained oxygen and the ratio of oxygenate hemoglobin to deoxygenated hemoglobin (oxygen saturation) decreases in time. Similar to previous studies [33, 119], we have observed the hyperemia after the release of occlusion

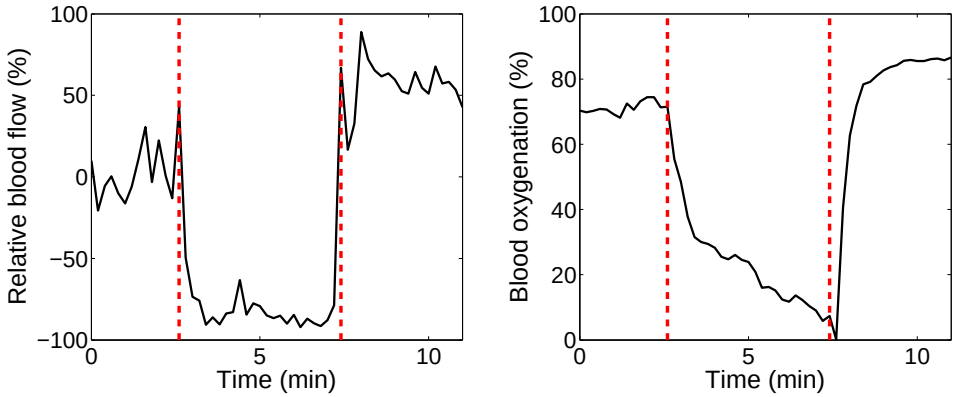

Fig. 3.14 Hemodynamics changes induced by mouse thigh cuff occlusion. Vertical lines indicate the beginning and end of the occlusion.[Left] Relative blood flow during arterial cuff occlusion. By applying the occlusion blood flow decrease and the cuff release causes and over shoot in relative blood flow. [Right] Relative blood oxygen saturation during arterial cuff occlusion on a mouse thigh. Deoxygenation during occlusion and hyperemia after the release of occlusion is observed.

Chapter 4

Monitoring the effect of antiangiogenic therapy on murine renal cell carcinoma

4.1 Introduction

Angiogenesis, the formation of new blood vessels, plays an important role in the growth and spread of cancer [172, 173, 197]. Tumors need new blood vessels that provide them with oxygen and nutrients in order to grow [198]. Access to the newly formed vessel network allows the cancer cells to invade nearby tissue, and to move throughout the body to form new colonies of cancer cells (metastases) [174, 199]. In order to develop angiogenesis, tumors undergo complicated signaling process by production of angiogenic agents such as vascular endothelial growth factor (VEGF) [200]. Inhibition of angiogenesis is emerging as a new therapeutic approach to control tumor progression [201, 202]. Several clinical trials have provided evidence that antiangiogenic therapy, alone or in combination with chemotherapy, is effective and may increase the survival of patients [203, 204]. Followed by effective phase of antiangio-

genic therapies, tumors adapt and begin regrowing via a process referred to as "evasive resistance" [205–207]. In several studies the development of nonresponsiveness to an initially efficacious anti-VEGFR therapeutic regimen in a xenotransplant model is demonstrated [208–210]. The resistance mechanism is mostly unknown, and this arises a strong demand for imaging modalities that can study the hemodynamics changes induced by therapies to identify the early signs of nonresponsiveness. In therapies on human patients early identification of nonresponders is essential to personalize the treatment and to avoid the resistance phase, which results in more aggressive tumors [211].

There are several methods to measure oxygen level of tumors, but due to invasiveness, depth of measurement, and utilized contrast/radiative agents, these methods are not ideal for continuous, repeated measurements [15]. There are also a number of techniques for the measurement of blood flow in the tissue [212]. Doppler ultrasound has been applied to measure the perfusion changes in the mouse tumors due to cancer therapy, but its information is limited to the tumor surface [213, 214]. Laser Doppler can noninvasively monitor the flow change, but the penetration depth is very low and it is limited to surface measurement [215]. Similarly, there are also imaging technologies in microvascular assessment such as laser speckle flowery or optical coherence tomography [215–217] that can image the surface of the tumor noninvasively.

Considering the limitation of current techniques for measurements of deep tissue oxygenation and blood flow, we have deployed diffuse optical spectroscopy techniques to study hemodynamics changes induced by antiangiogenic therapies on murine models. Changes in level of vascularization alters the hemodynamics of the tissue, which can be correlated to optical measurements of microvascular blood flow, blood volume or oxygen saturation [43, 98]. During last decade many researchers demonstrated that diffuse optics is a strong tool to monitor the hemodynamics

changes induced by cancer therapies and have the potential to predict therapeutic efficiency [52, 54, 95, 100, 101, 110, 142]. In this study we have deployed a hybrid diffuse optics system that measures blood flow by diffuse correlation spectroscopy (DCS) in addition to tissue oxygenation and hemoglobin concentration by diffuse optical spectroscopy (DOS).

In this work, we have observed that early changes in tumor hemodynamics induced by antiangiogenic therapies has correlation with the time that each tumor starts to resist against therapy as well as final size of tumor. These findings suggest that we can predict the output of therapy and resistance time of the tumor, time-to-progress (TTP), which are valuable information for better understanding of the tumor resistance mechanism to antiangiogenic therapy, which in human treatment may lead to personalized therapy with higher success.

4.2 Methods & materials

4.2.1 Optical device and data analysis

We have combined broadband near infrared spectroscopy and diffuse correlation spectroscopy in a single self-calibrated probe. The full description of the device and probe is given in chapter 3. In DOS setup in order to prevent edges of CCD, we have used 6 source-detector separations (2.5- 5.0 mm). DCS also utilizes 6 optode distances (2.9- 5.0 mm). We have also deployed a control probe which is located on a healthy tissue of the body (a muscle) to monitor the global hemodynamics changes during the anesthesia. In the control probe both DCS and DOS have only one source-detector pair with ~ 4 mm separation. In summary DOS measures oxygen saturation and hemoglobin concentration and DCS measures blood flow in the tissue. In every measurement, in order to have better statics of the optical properties of tumor we have re-positioned the probe 10 times and took 11 acquisitions. The detailed

description of fitting and data analysis is in section 3.6.

4.2.2 Animal models and treatment procedure

Fourteen immunosuppressed male athymic nude mice were measured in this study. Seven mice received the antiangiogenic therapy twice per week and the rest were as control group and were receiving placebo with the same frequency as treated animals.

Orthotopic implantation of renal cell carcinoma (RCC) tumors: Male athymic nude mice were purchased from Harlan Laboratories. Mice were housed and maintained in laminar flow cabinets under specific pathogen-free conditions. All the animal studies were approved by the local committee for animal care. Fresh surgical specimens of RCC were obtained after surgical resection from the Hospital Universitary de Bellvitge (L'Hospitalet de Llobregat, Barcelona, Spain) and placed in Dulbecco's Modified Eagle's Medium (DMEM), BioWhittaker, supplemented with 10% FBS (Fetal bovine serum), 50 units/mL penicilin and 50μgr/mL streptomycin sulfate. These animal models are based on orthotopic implantation of little pieces (2 x 2 x 2 mm^3) of human RCC tumor biopsies by surgical implantation into the original neoplastic organ on immunosuppressed nude mice, following studies pioneered by Dr. G. Capellá [218, 219]. Briefly, 5-weeks-old male mice weighing 18-22 gr was anesthetized by isoflurane inhalation. A small midline incision was made and the kidney was exteriorized. A piece of tumor was implanted on left kidney using prolene 7-0 surgical suture. The kidney was returned to the abdominal cavity and the incision was closed with wound clips. Different tumors were perpetuated in mice by consecutive passage according to the growth rate of each tumor type. For our study, we use a renal cell carcinoma of clear cell histology (REN 28), Fuhrman grade 4/4 and pathological staging pT3pN1.

Biological point of view: We have developed several advanced mouse models of renal cell cancer (RCC), human tumorgraft RCC mouse models, designed to better resemble the human pathology and show more parallelism in their responses to therapies (in particular when targeting components of the tumor stroma). These little human tumor biopsies grow in mice preserving the stromal architecture (even when it is replaced by mouse stroma), and they can be passaged (and expanded) to many new recipient mice by re-implanting a piece of tumor to many new animals (commented by Garber [220]). Therefore, these mouse lines preserve a stromal rich tumor structure in the growing tumors, which have a very high resemblance to the original human tumor that was in the patient (figure 4.1). Thus, these animal models allow for more relevant studies of the tumor responses to treatment than standard xenograft models because they maintain the tumor-stromal proportion, structure and many of their functional.

Legalities on animal models An animal research project protocols for the tumorgraft models have been evaluated and accepted by IDIBELL's animal research committee and have been registered and accepted by the "Animal Experimental Comission" from the local Catalan government and the "Comisión de Ètica en Experimentación Animal" from the national Spanish government (Protocol number 4899, PI:Oriol Casanovas).

Antiangiogenic treatments The antiangiogenic drug used is very specific monoclonal antibody that binds and blocks mouse-VEGFR2 signaling, named DC101. This antibody has the advantage of having a species-restricted activity, as it does neither recognize nor block human-VEGFR2 [88, 221, 222]. Therefore, when used in the tumorgraft models, we are sure that this drug is not affecting the tumor cells directly but rather it only has an antiangiogenic effect. The blocking antibody of

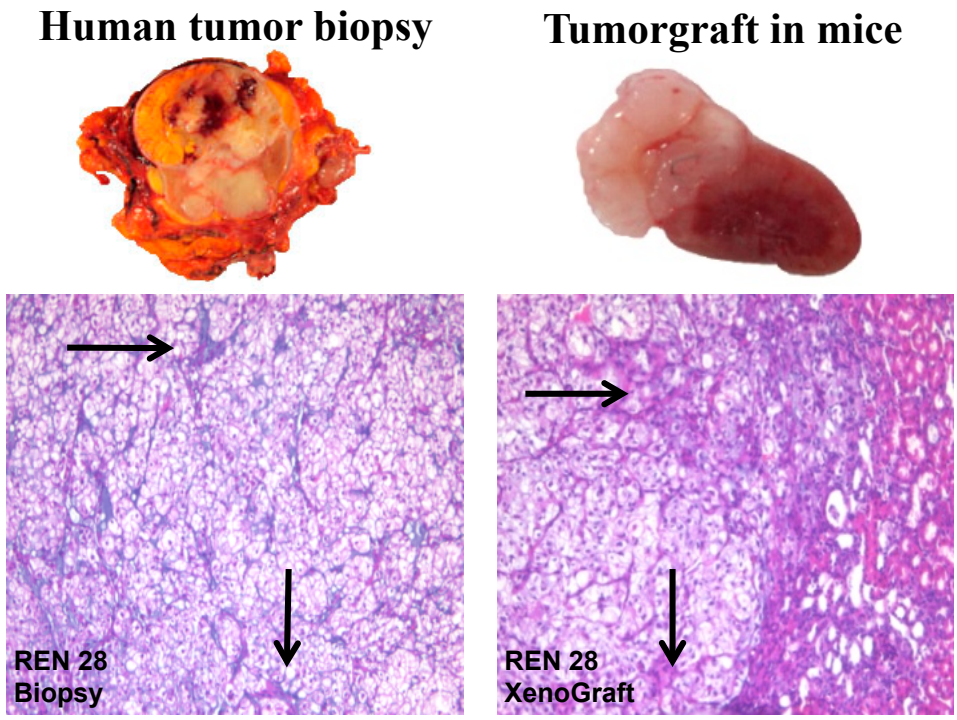

Fig. 4.1 Newly developed tumorgraft mouse model to study antiangiogenic therapies. Histological H&E sections of renal cell carcinoma (Ren28) demonstrate high similarity in the tissue structure and pattern between human primary tumor biopsy (left panel) compared to its respective mouse tumorgraft tumor (right panel). Arrows indicate stromal structures in the form of trabeculae and clusters found in both tumors (human biopsy and mouse Tumorgraft). Credits: Dr. Gabriela Alejandra Jimenez from Dr. Oriol Casanovas's lab.

VEGFR2 (DC101) can be obtained in large scale by purification from supernatants of the hybridoma DC101 in culture (modified from ATCC), and is used at the dose of 1 mg/animal by intraperitoneal injection twice a week, as previously described [209, 210]. For each mouse when the tumor volume reached $\sim 1000\ mm^3$ the therapy was started (DC101 or placebo). The mice kept receiving the therapy/placebo up to the time that due to the tumor size or mouse weight loss, we had to stop the measurement and sacrifice the animal.

4.3 Results and discussions

4.3.1 Physiological characterization of the tumor

In RCC tumors, we have measured hemodynamic properties such as oxygen saturation, total hemoglobin concentration and blood flow index. In figure 4.2, the average of these parameters over all mice measured all days on tumor and a control muscle (shoulder muscle) are presented. The blood flow index in tumor is 25.1% higher than the muscle ($P < 10^{-4}$). Measured total hemoglobin concentration in tumor is 22.8 μM lower than healthy shoulder muscle ($P < 10^{-4}$). Malignant tumors are usually expected to be hypoxic [133, 223]. In the case of RCC tumors we have observed that blood oxygen saturation in tumor is 9.1% higher than normal tissue ($P < 10^{-4}$). It may be explained by the existence of blood shunts in RCC tumors which are the closed arterioles passing throughout the tumor without having the chance of oxygen exchange [224].

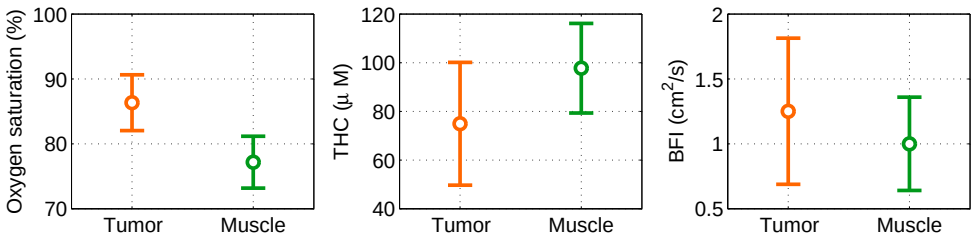

Fig. 4.2 The optically measured hemodynamic properties of the RCC tumor in comparison with a control muscle. The reported difference in all three cases are statically significant ($P < 10^{-4}$). [Left] Blood oxygen saturation in the tumor is 9.1% higher than healthy shoulder muscle. [Middle] The total hemoglobin concentration in the tumor is 22.8 μM lower than healthy shoulder muscle. [Right] The blood flow index in the tumor is 25.1% higher than healthy shoulder muscle.

4.3.2 Correlation between measured parameters by DCS and DOS

Total hemoglobin concentration (THC) and blood flow index (BFI) are measured by DOS and DCS respectively, which are independent separate devices. Figure 4.3 shows the measured values of THC and BFI for all mice (treated and control) over all days are correlated with each other. The agreement between measured physiological parameters by two independent devices validates our measurements. For treated tumors the correlation coefficient is r = 0.45 and it is statically significant ($p < 0.001$). In control tumors the correlation coefficient is r = 0.67 and it is statically significant ($p < 0.001$).

4.3.3 Early blood flow changes induced by antiangiogenic therapy

Figure 4.4 demonstrates the evolution of measured blood flow index in treated and control tumors over time. Similar plots for other optical and

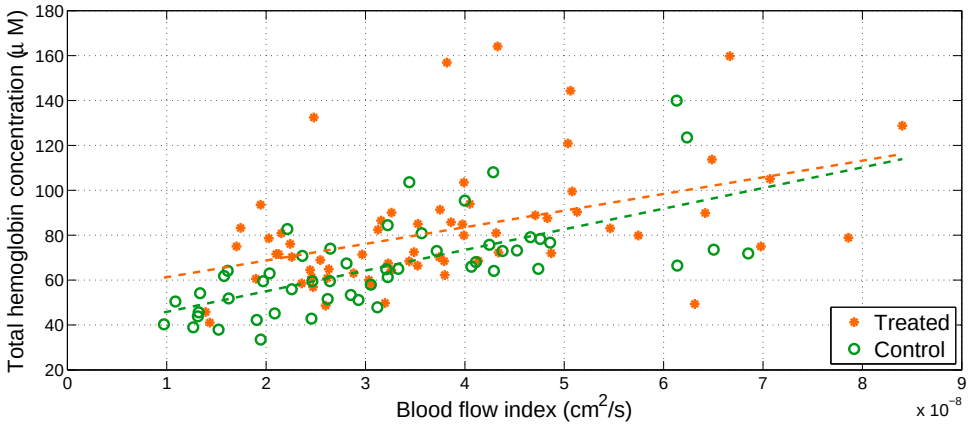

Fig. 4.3 Total hemoglobin concentration versus blood flow index over all mice in all days. The measured values from treated mice are presented by orange stars and control animals by green circle. In both control and treated groups the measured total hemoglobin concentration (from DOS) and blood flow index (from DCS) have positive correlation. For treated tumors the correlation coefficient is r = 0.45 and it is statically significant ($p < 0.001$). In control tumors the correlation coefficient is r = 0.67 and it is statically significant ($p < 0.001$).

physiological parameters such as absorption coefficient, reduced scattering coefficient, total hemoglobin concentration and oxygen saturation are presented in Appendix B. In figure 4.4, the number of measurement days for each mouse is different because they have been sacrificed in different days after start of the study. Each point is average of all 10 measured locations on the tumor. While the BFI of control animals slowly decrease, in all treated animals an initial drop of blood flow is observed. This initial decrease observed in all mice after the first session of therapy. In some of them the initial drop continues up to the second session of treatment. The initial decrease of BFI is followed by an increase in blood flow. We will investigate the correlation between the maximum decrease of blood flow (initial change of blood flow) with the outcome of the therapy following in this chapter.

4.3.4 Tumor size and time-to-progress (TTP)

Figure 4.5 shows the measured size of tumor by palpation during the therapy. The number of measurement days for each mouse is different because they have been sacrificed in different days after start of the study. The tumors of control mice grow gradually but treated tumors do not grow for one or two weeks and start to progress afterwards. The time that takes for each tumor to get resistant to the therapy and start to grow is called time-to-progress (TTP). To calculate the time of progress a threshold tumor volume is defined. The threshold volume is the average plus two times standard deviation of initial volume of all tumors. TTP of each mouse is the time that takes for the tumor to reach the threshold volume. Following in this chapter we will investigate the possibility of early prediction of TTP.

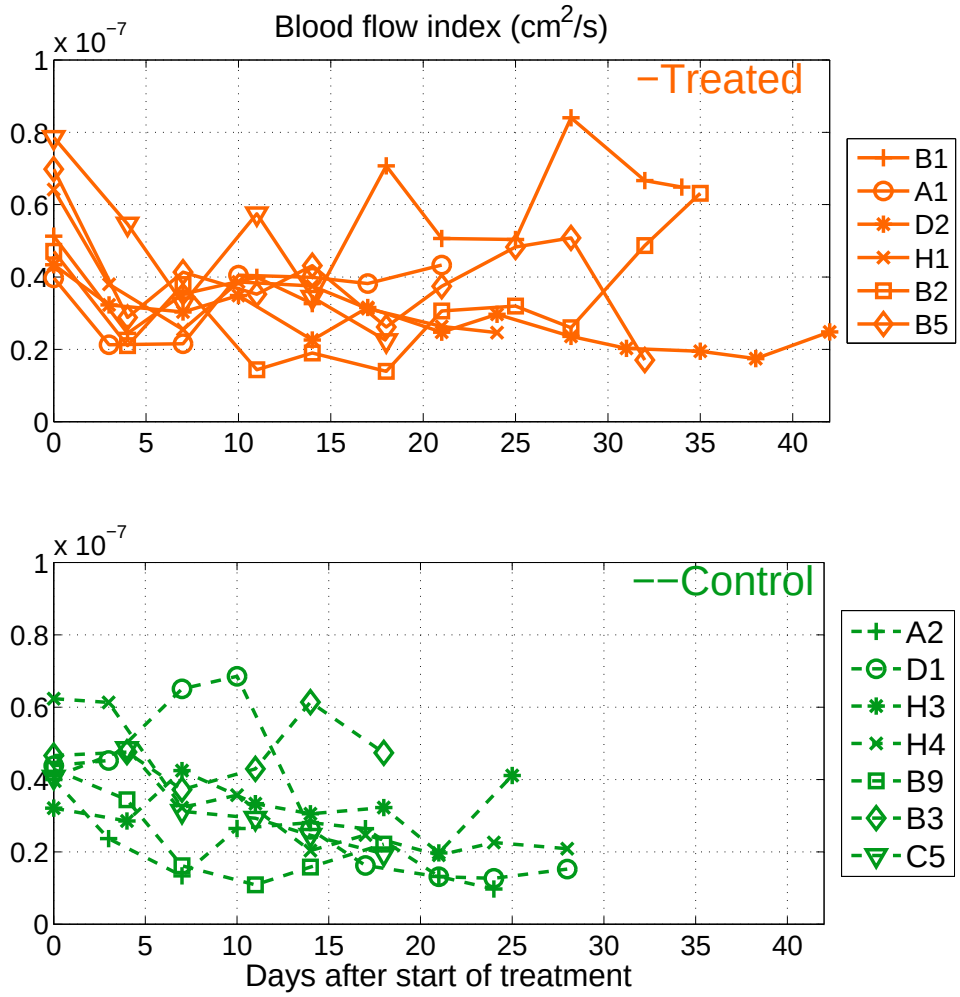

Fig. 4.4 Blood flow changes of both treated (top) and control mice (bottom) are presented over all days of measurement. The number of measurement days for each mouse is different because they have been sacrificed in different days after start of the study. All the treated animals have an initial drop in the blood flow.

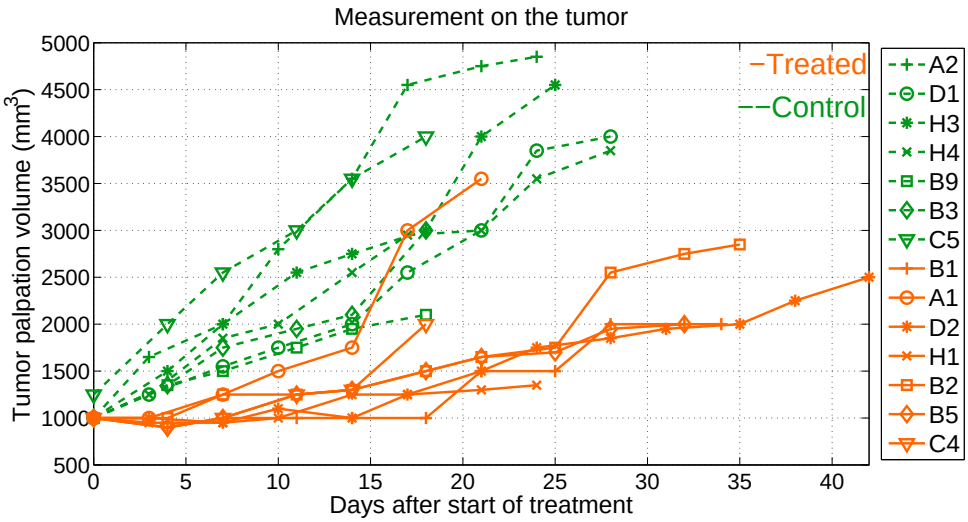

Fig. 4.5 Tumor size measured by palpation from both treated (solid orange lines) and control mice (dashed green lines) are presented over the time. The number of measurement days for each mouse is different because they have been sacrificed in different days after start of the study. The tumors of control mice grow gradually but treated tumor does not grow for one or two weeks and start to progress afterwards.

4.3.5 Extracted tumor weight and histology results

After sacrificing each mouse, the tumor was extracted for the measurement of its volume and volume and to prepare it for histological studies. The measured extracted tumor weight is for both treated and control group is presented in figure 4.6. In average the extracted tumors from the treated animals are lighter than control ones.

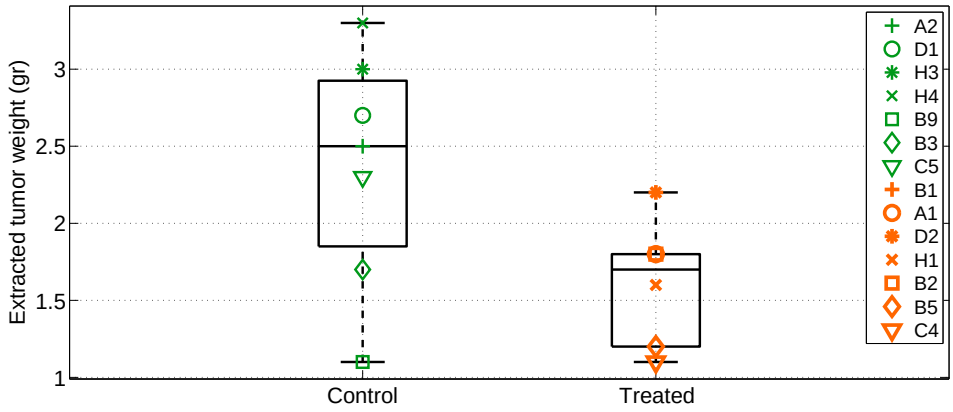

Fig. 4.6 The extracted tumor weight of treated and control group. In average the extracted tumors from the treated animals are lighter than control ones.

In this study we have used cluster of differentiation 31 (CD31) staining to measure the micro-vessel density (MVD) in the tumor. Figure 4.7 demonstrates the measured MVD in the extracted tumor measured by CD31 staining. In average tumors of treated mice have lower MVD in comparison to control group.

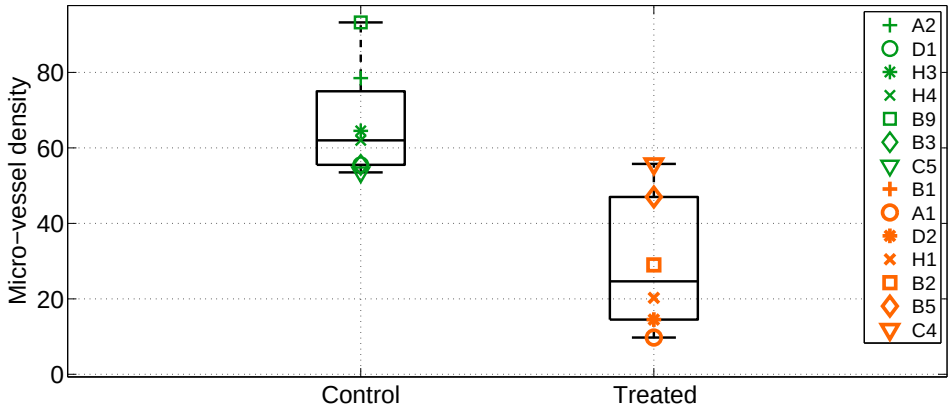

Fig. 4.7 Micro-vessel density (MVD) in the extracted tumor measured by CD31 staining. In average tumors of treated mice have lower MVD in comparison to control group.

4.3.6 Early blood flow changes correlates with extracted tumor weight and histology results

It is shown in figure 4.4 that all the treated mice showed an initial decrease in the blood flow index. In order to investigate the predictability of the optically measured data, the correlation between the maximum decrease of blood flow (initial change of blood flow) with the outcomes of the therapy are inquired. One of the standard outcomes of therapy in experimental oncology is the weight of extracted tumor. Figure 4.8 demonstrates that initial blood flow changes has a strong correlation with the the extracted tumor weight. It shows that larger drop of blood flow is an indicator of smaller tumor. The correlation coefficient r = 0.9 and p-value is equal to 0.006.

Figure 4.9 shows the correlation between the measured MVD and the initial change of blood flow index. The correlation coefficient r = -0.8 and p-value is equal to 0.04. It can be observed that mice with

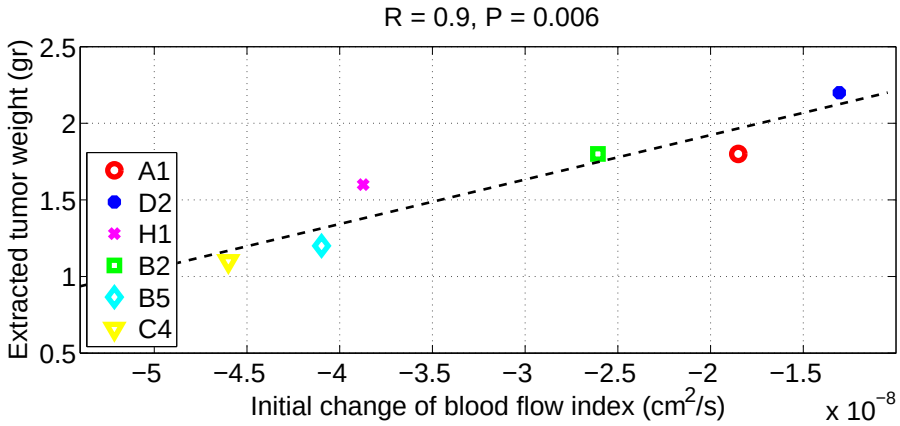

Fig. 4.8 There is a positive correlation between initial change in blood flow and the extracted tumor weight in the treated mice.

larger initial drop of blood flow have higher values of MVD.

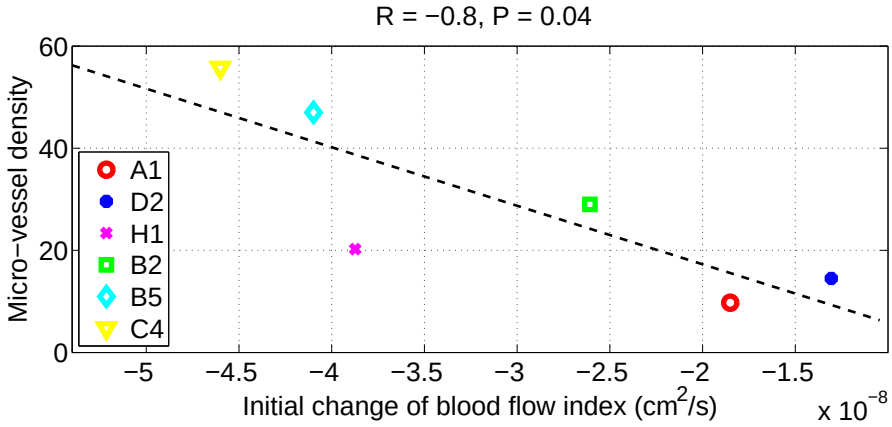

Fig. 4.9 There is a negative correlation between initial change in blood flow and the blood vessel density obtain by CD31 staining in the treated mice.

4.3.7 Early blood flow changes as a predictor of TTP

TTP is an important therapeutic factor and knowledge about it, enables the physicians to plan the duration of therapy. We have explained the procedure of calculating TTP in section 4.3.4. In this section we have investigated the correlation between TTP and initial change of blood flow index. Figure 4.10 shows a good correlation between the initial drop of blood flow index and TTP. The correlation coefficient r = 0.8 and p-value is equal to 0.03. One mouse, A_1, is an outlier in this plot and it is excluded from correlation calculation. Mice with higher drop of blood flow starts evasive resistance earlier. This results suggest the potential of optics to predict the resistance of the tumor.

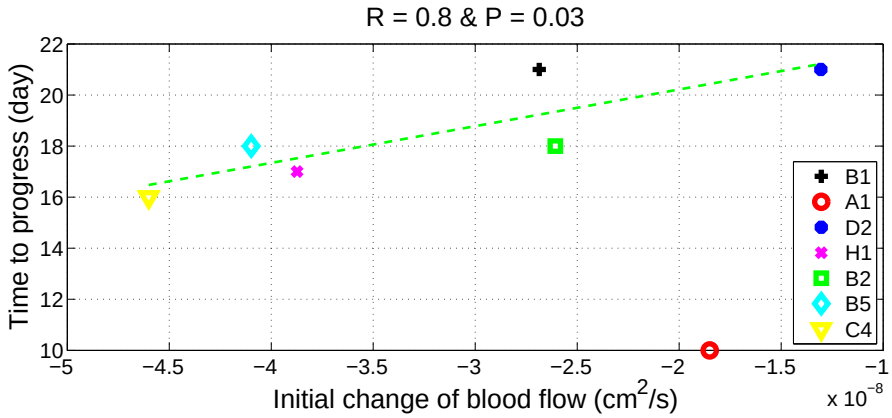

Fig. 4.10 There is a positive correlation between initial change in blood flow and the time-to-progress (TTP) in the treated tumors. One mouse, A_1, is an outlier in this plot and it is excluded from correlation calculation.

4.4 Conclusion

In this study we have applied diffuse optical spectroscopy methods for hemodynamics monitoring of the murine tumors during antiangiogenic therapy. We have shown that hemodynamics properties of the tumor alters by starting the antiangiogenic therapy. These early changes shows a strong correlation with the outcome of therapy such as tumor weight, CD31 staining and time for the tumor to get resistant. These results suggest that diffuse optics is an strong tool to understand the defense mechanisms of tumor against antiangiogenic therapy. The main weakness of this study is the limited number of mice and continuing the study with larger number of tumors may lead us to develop optical parameters to predict the success of therapy which results in personalized treatment for each subject.

Chapter 5

Noninvasive characterization of the healthy human of bone marrow using diffuse optical spectroscopies

5.1 Introduction

Hematological malignancies such as leukemias, lymphomas, and multiple myelomas are common, accounting for about ∼9% of all newly diagnosed cancers [225, 226] and most of them have a poor prognosis [227, 228]. In children and adolescents younger than twenty years, hematological malignancies are the most common type of cancer, responsible for more than 30% of all cancers [227, 228].

Most of these cancers originate in the bone marrow since this tissue is the main site of blood cell formation. In the bone marrow, hematopoietic stem cells (HSCs) differentiate into blood cells: red cells, white cells, and platelets. Mutations that inappropriately activate HSC proliferation cause an uncontrolled growth of abnormal blood cells and lead to

hematological malignancies. This high proliferating activity of HSCs induces angiogenesis in the bone marrow [229–231] and increase in angiogenesis of the bone marrow has indeed been observed in patients with progression of these malignancies [232–236]. It has also been shown that the degree of angiogenesis is an important prognostic factor [237–240], an indicator of the disease burden, and is associated with the treatment outcome [241, 242].

Therefore, it is of interest to investigate the degree of vascularization of the bone marrow which is important for better estimation of prognosis and for personalization of the therapy procedure. Measurement of angiogenesis is important for the follow up of treatment and screening during the reemission phase. In the clinical routine, the most direct and common technique of angiogenesis evaluation is histomorphological analysis of the bone marrow, basically the measurement of microvessel density. It involves a bone marrow biopsy taken from the iliac crest or the sternum. However, biopsy has several limitations: it is invasive, it has substantial inter-observer variability, and analyzes just a discrete site of the whole bone marrow [243]. Dynamic contrast enhanced magnetic resonance imaging (DCE-MRI) is also applied to investigate the degree of vascularization. Although DCE-MRI is noninvasive and has a relatively high resolution, it is expensive and utilizes contrast agents, therefore it is not suitable for screening and repeated measurements. Another clinical technique to estimate the extent of the angiogenesis is measurement of the angiogenic biomarker levels in a blood sample [244, 245]. However, the estimation of biomarkers achieved by blood extraction is not targeted to a specific tissue and angiogenesis in other organs may elevate it. Therefore, the level of angiogenesis in the bone marrow and biomarkers in the blood are not necessarily correlated [246, 247].

In experimental studies, positron emission tomography (PET) and single photon emission computed tomography (SPECT) have also been

used to measure the blood flow in the bone often as a correlate of angiogenesis [248–250]. PET has also been used to image the proteins, which are implicated in the angiogenesis procedure [251]. Despite the good sensitivity of these techniques, high cost measurements in addition to exposure to radioactive agents make them limited for repeated measurements. They have not been adopted for widespread clinical use.

Considering the importance of angiogenesis and the limitations of current techniques, we hypothesise that the noninvasive diffuse optical spectroscopy techniques might be useful and practical to study the hemodynamics of normal and malignant hemopoiesis as a potential correlate of increased angiogenesis and proliferation. Increased angiogenesis alters the hemodynamics of the tissue which can be correlated to optical measurements of microvascular blood flow, blood volume or oxygen saturation [43, 98].

Furthermore, in subjects with hematological malignancies, the high proliferating activity of the hemopoietic tissue is observed due to angiogenesis in the bone marrow [229–231]. Since high proliferation may alter the hemodynamics of the tissue as well as its scattering coefficient, diffuse optics can be potentially utilized for screening purposes to detect high risk subjects. Furthermore, the degree of angiogenesis has been considered a predictive factor of response to treatment. In this sense, it could be a promising noninvasive method for categorizing the risk of the patient before the treatment. It can also be applied to monitor the changes in bone marrow hemodynamics induced by the antiangiogenic therapies which are emerging as effective treatments against cancer [252, 253]. Following the response to the therapy may help to personalize the therapy for each subject.

Diffuse optical spectroscopy is a noninvasive method that does not use ionizing radiation or contrast agents [2]. The device and measurements are relatively inexpensive and it is a suitable method for repeated

measurements. It can be combined with other modalities such as MRI [99] for simultaneous measurements to provide complementary information.

While the bulk of diffuse optics in biomedicine was used on soft tissue, the feasibility of applying optical methods on human bone tissue have been investigated in several works [121, 122, 144, 153, 254–270]. Furthermore, it has been demonstrated that bone is an active tissue whose hemodynamics is responsive to physiological changes such as cuff occlusion [144].

Accessibility of the target tissue is the key concern in noninvasive diffuse optical measurements since it can mostly measure the upper (∼1-5 cm) layers of tissue. In adults hematopoietic tissue exist mostly in flat bones such as the pelvic girdle and the sternum. Manubrium, the broad, upper part of the sternum is a common site for bone marrow biopsy as it is accessible and rich in hematopoietic marrow [271]. We have identified it to be also suitable for noninvasive diffuse optical probes since it is quite superficial with no overlying muscles and is sufficiently thick for adequate probing. Therefore, we have applied diffuse optical spectroscopy to measure the hemodynamics of the healthy manubrium noninvasively by combining two diffuse optical methods; time resolved spectroscopy (TRS) [51, 90, 150, 154] and diffuse correlation spectroscopy (DCS) [2, 96] in a single probe. This combination enabled us to measure the concentration of oxygenated and deoxygenated hemoglobin as well as the blood flow index alongside the tissue reduced scattering coefficient. In the future, with appropriate modeling, this may enable us to calculate the rate of metabolic oxygen extraction. By this method, we characterize the optical properties (absorption and scattering coefficients) and physiological properties (hemoglobin concentration, oxygen saturation and blood flow index) of healthy bone marrow by noninvasive measurement of thirty two healthy subjects. We also investigate the effect of the

location of the probed site on the manubrium, body mass index (BMI), gender, thickness of the overlying tissue and age on the distribution of the measured parameters. Our hypothesis was that the properties of health tissue has a relatively narrow distribution which would enable us to detect the changes due to pathologies. It can be used for screening purposes in order to detect subjects with a high risk of malignancy and it is repeatable which would make it a potential tool to monitor the effect of the therapy. The results of this study is published in Farzam et al. [157].

5.2 Methods & materials

5.2.1 Study population and the measurement protocol

All protocols and devices were approved by the ethical committee of Hospital Clínic de Barcelona where all subjects were measured. Thirty-two healthy subjects were recruited for this study (15 females and 17 males) and each subject has signed a written informed consent. Since bone marrow properties depend on age [272, 273], in order to have a more homogeneous group of people, an age range between 25-40 years old was defined as the inclusion criteria [1]. Adolescents are of great interest to the study of hematological malignancies due to the high prevalence in that population. However, due to ethical concerns related to informed consent of minors, we have excluded them from this preliminary study.

The subjects were requested to fill a basic health questionnaire where they were asked about their history of anemia, diabetes, lung diseases, kidney diseases, hypertension, hyperlipidemia, atrial fibrillation, con-

[1] Nevertheless, two subjects near to range limits (24 and 42 years old) were measured and were included in the study population.

gestive heart failure, coronary artery diseases, previous myocardial infraction and smoking. Each subject reported whether they have any other diseases and their current medications. Subjects with the history of any type of malignant neoplasms or severe anemia were excluded from this study. Among all subjects, two of them were under medication for thyroiditis and one subject for asthma. These medications do not have any known impact on the bone marrow hemodynamics, therefore, we have included these subjects in the study. There were also three smokers among the subjects who were included in the data, which may affect the systemic hemodynamics. In Table C.1, Table C.2, and Table C.3 they are labeled by a star sign. Furthermore, before (in a few cases, after) the optical measurement, the vital signs (heart rate, arterial blood pressure and arterial oxygen saturation) were measured to assure that the subject is in normal health condition and to explore any correlations with the results. The vital records are summarized in Table 5.1 and the physical characteristics in Table 5.2. Body mass index (BMI) is calculated by dividing the weight [kg] by square of the height [m]. The thickness of the tissue overlying manubrium skin was estimated by the caliper skinfold measurement. These two parameters are highlighted since they may effect the optical measurement.

Table 5.1 Vital records of the recruited subjects: median ($1^{st} - 3^{rd}$ quartile).

	Arterial oxygen saturation (%)	Heart rate (bpm)	Systolic pressure* (mmHg)	Diastolic pressure (mmHg)
All	99 (97, 99)	74 (66, 84)	119 (114, 136)	71 (67, 76)
Females	99 (99, 99)	78 (69, 88)	117 (102, 118)	71 (68, 75)
Males	98 (97, 99)	73 (65, 80)	135 (120, 140)	72 (67, 80)

* The difference between males and females is statistically significant ($P < 0.05$).

Table 5.2 Physical characteristics of the recruited subjects: median ($1^{st} - 3^{rd}$ quartile).

	Age* (year)	Weight* (kg)	Height* (cm)	BMI* (kg/m^2)	Skinfold/2 (mm)
All	30 (27, 33)	74 (58, 84)	172 (164, 180)	23.3 (21.6, 26.7)	4.7 (3.9, 6.2)
Females	29 (27, 30)	58 (53, 62)	163 (160, 169)	21.4 (20.7, 23.4)	4.4 (3.6, 4.8)
Males	32 (27, 35)	79 (73, 86)	180 (177, 183)	24.5 (23.3, 26.8)	5.1 (4.3, 7.0)

* Difference between males and females is statistically significant ($P < 0.05$).

For the measurements, the subjects were asked to sit comfortably on a chair with the head tilted back. A hematologist with experience in bone marrow biopsies located the manubrium and marked the outside borders to guide the positioning of the optical probe. The height of each manubrium was divided into four regions from top to bottom (neck to breast) labeled as one to four. The markings and the probe placement are illustrated in Figure 5.1. On each location, three measurements were performed.

5.2.2 Device and probe

The custom-built TRS instrument consists of three pulsed lasers (Becker & Hickl, Berlin, BHLP-700) emitting at 687, 785 and 830 nm with pulse widths of 400, 350, and 450 pico-seconds respectively for each wavelength and a repetition rate of 50 MHz. The pulses are sent to the tissue using a 10 meter long fiber with a 90° bent tip and a core diameter of $62.5\,\mu m$ ($NA = 0.275$). The diffuse light was collected by a custom made bundle that consists of 54 graded index multimode

[1]Retrieved and adopted on December 30, 2013, from: "http://commons.wikimedia.org/wiki/File:Manubrium_lateral.png"

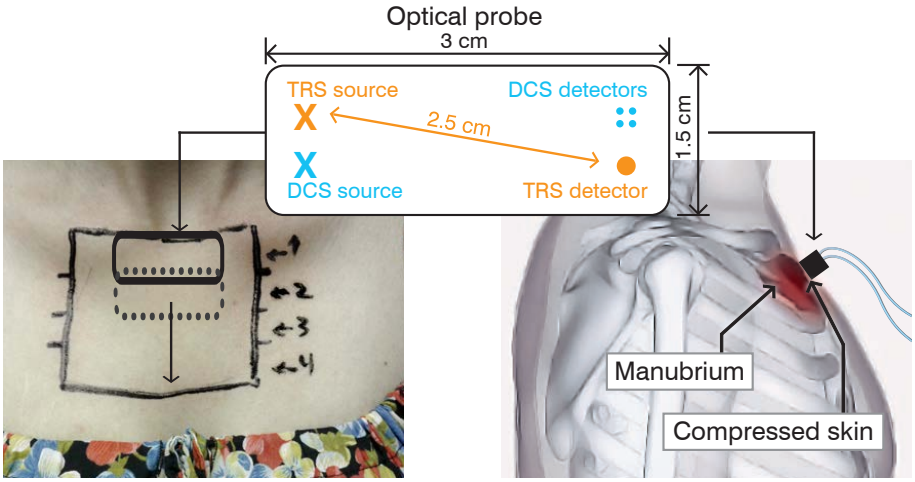

Fig. 5.1 (Left) The photograph of the manubrium of a female subject. The lines show the outer border of the bone marked by a hematologist. The height is measured and divided into four regions. The dashed/solid rectangles indicate the approximate probe positions. (Right) The location of sternum in the upper part of the skeleton. The drawing is adopted from the Wikimedia Commons.[1] The probe is pressed to the manubrium so that the skin on the contact area is compressed. (Top) The schematic of the probe with one source and one detector for TRS (source-detector separation = 2.5 cm) and one source and four detectors for the DCS device (source-detector separation = 2.5 cm).

fibers and delivered to a hybrid photo multiplier tube (PMT, Becker & Hickl,Berlin, HPM-100-50). A standard time-correlated single photon counting (TCSPC) setup (Becker & Hickl, Berlin, Simple-Tau 130) is used to record and store the distribution of the time of flights of the diffuse photons [150].

The DCS part of the setup uses a single longitudinal mode laser as the source (CrystaLaser, Reno, NV, USA) at 785 nm whose coherence length (> 15 m) is much longer than the distribution of typical photon path lengths. The laser light is delivered to the tissue through a multimode fiber with a core diameter of $200\,\mu m$ ($NA = 0.22$). Since DCS uses single mode fibers of $5.8\,\mu m$ core diameters for collection which limits the detected photon count rate, we bundle four fibers together to improve the signal-to-noise ratio. Four photon counting avalanche photodiodes are used as detectors (Excelitas, Quebec, Canada) whose output is fed to a digital correlator (Correlator.com, New Jersey, USA) to obtain the autocorrelation functions. Details of the DCS system is discussed in various reviews [2, 27].

Time resolved spectroscopy (TRS) and diffuse correlation spectroscopy (DCS) are combined in a single probe as illustrated in Figure 5.1. For both, TRS and DCS, we use a source-detector separation of 25 mm. For each location there were three acquisitions with an averaging time of three seconds for DCS and three seconds per wavelength for TRS amounting to approximately 12 seconds per measurement.

5.2.3 Data analysis

The experimental data is fitted with a solution of the diffusion approximation for a semi-infinite homogeneous medium [147] to extract the values of the reduced scattering ($\mu_s{}'$) and absorption (μ_a) coefficients for each wavelength. For more details look at chapter 2, section 2.4, equation 2.9.

In this process the theoretical curve is convoluted with the instrument response function. The fitting range includes the points with a number of counts higher than 80% of the peak value on the rising edge of the curve and 1% on the tail. The fitting was performed by "fminsearch" function of Matlab (Mathworks Inc, Massachusetts, USA). The relation between absorption coefficient with concentration of chromophores is presented in at chapter 2, section 2.5, equation 2.10. In this study oxy, deoxy and water were assumed as the only absorbers in manubrium. The water concentration in the bone was assumed to be 30% [274] and oxy- and deoxy-hemoglobin concentrations were measured (c_{HbO_2}, c_{Hb}).

The total hemoglobin (THC) concentration and oxygen saturation information are calculated from concentration of oxygenated hemoglobin (c_{HbO_2}) and deoxygenated hemoglobin (c_{Hb}) (look at section 2.5).

The theory behind DCS technique and the measurement of blood flow index (BFI) is described at chapter 2, section 2.6. For the DCS fitting we have used the "fminsearch" function of Matlab. The measured μ_a and $\mu_s{}'$ by TRS for each subject (averaged over all locations and acquisitions) was introduced as an input for DCS analysis.

5.2.4 Statistical analysis

As a first step, we have explored the measured parameters to check if the data has a normal distribution. The normality was tested using a two sided "Shapiro Wilk" test. We have cross-checked the results of "Shapiro Wilk" test by quantile-quantile plots. Both tests were in agreement with each other.

For each measured parameter (μ_a, $\mu_s{}'$, THC, blood flow index, and oxygen saturation) the median as well as $1^{st} - 3^{rd}$ quartile values are reported.

To examine the correlation between different measured parameters we have fitted a linear mixed effects (LME) model [275, 276] using pack-

ages “lme4” [277] and “lme4test” [278] in R (open source statistical computing language [279]). This method was utilized since it does not have a strict normality assumption [275]. In all the analysis, the normality of the residuals were examined visually and no obvious deviations from normality were revealed. We rejected results in which the full model did not differ significantly from the null model.

To test the dependency of the optical parameters on the location of the probe we have fitted an LME with the location as the fixed effect. The subject was considered as the random effect in this model. In this analysis, the first location is considered as the reference.

The correlation between measured physiological parameters (blood flow, blood volume and oxygen saturation) were also investigated by LME. Since we have observed a dependency of measured parameters on the location of probe, here both location and measured parameter were fixed effects and subject was the random effect.

We have applied LME model to study the effect of BMI, skinfold value, and age of the subjects on the measured physiological parameters. In these models the parameter under the investigation (BMI, skinfold, age) and the location of the measurement were the fixed effects and the subject was the random effect.

Furthermore, the effect of gender on the measured parameters was examined. Since we have observed a difference between BMI of males and females and a significant effect of BMI on the measured parameters, we have considered gender, BMI and location as the fixed effects. Here the subject was the random effect.

At the end, in order to investigate the effect of our assumptions on the results, we have calculated the hemodynamic parameters (THC and oxygen saturation) assuming different concentrations of chromophores (bone mineral and lipid). The difference between the distribution of physiological parameters under different assumptions was investigated

by student's t-test. Throughout this study, "p-values" less than 0.05 were considered statistically significant to reject the null hypothesis.

5.3 Results

5.3.1 The distribution of the measured optical and physiological parameters

Figure 5.2 shows the histogram of the distribution of the measured parameters for all subjects over four locations on the sternum. The Shapiro-Wilk test shows that the values of measured THC and blood oxygen saturation are normally distributed while the blood flow index does not have a normal distribution. For all three wavelengths μ_a values are normally distributed and $\mu_s{}'$ distributions were not normal.

The summary of all the measured optical and physiological parameters are listed in Table 5.3. Each parameter is presented with its median and $1^{st} - 3^{rd}$ quartile range. For completeness, the data from each individual subject is presented in Appendix C; Table C.1, Table C.2 and Table C.3.

Table 5.3 Median and inter-quartile range values for the measured physiological parameters.

	λ = 690 nm	λ = 785 nm	λ = 830 nm
μ_a (cm^{-1})	0.14 (0.12, 0.17)	0.15 (0.12, 0.17)	0.16 (0.13, 0.18)
$\mu_s{}'$ (cm^{-1})	10.1 (9.7, 10.9)	9.6 (9.0, 10.2)	8.7 (8.3, 9.5)
BFI (cm^2/s)	5.0×10^{-9} (4.2×10^{-9}, 7.4×10^{-9})		
THC (μM)	77.3 (62.2, 88.6)		
Oxygen saturation (%)	71.1 (69.5, 72.3)		

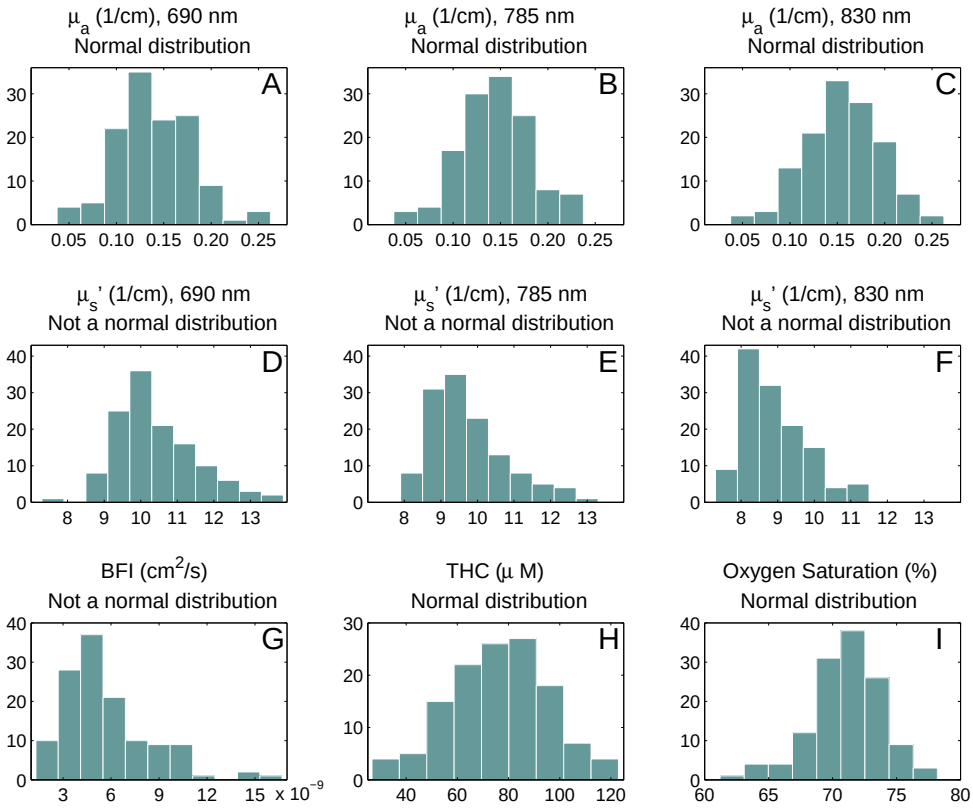

Fig. 5.2 The distribution of the measured hemodynamics over four locations on the manubrium for all subjects. (A-C) In each wavelength μ_a has a normal distribution. (D-F) $\mu_s{}'$ does not have a normal distribution in any wavelength. (G) The blood flow index is not normally distributed. (H) Total hemoglobin concentration values are normally distributed. (I) Blood oxygen saturation values are normally distributed.

5.3.2 The sensitivity of the measurements to the location of the probe

The distribution of the measured physiological parameters over four measured locations are illustrated in Figure 5.3. The intercept is the LME fitted value for the location 1 and the slope shows the change in comparison to the location 1. In Table 5.4 the fitted value for the first location (intercept) and the slope (changes between two consecutive locations) are listed. In all cases, both the intercept and the slope are statistically significantly different ($P < 0.05$) from zero indicating a clear yet small dependence on the location.

Table 5.4 The fitted value for the first location (intercept) and the slope (changes between two consecutive locations). All cases show statistically significant changes ($P < 0.05$).

	$\lambda = 690$ nm	$\lambda = 785$ nm	$\lambda = 830$ nm
μ_a (cm^{-1})	0.151 (- 0.005)	0.154 (- 0.003)	0.165 (- 0.004)
μ_s' (cm^{-1})	11.0 (-0.2)	10.2 (- 0.2)	9.4 (- 0.2)
BFI (cm^2/s)	4.8×10^{-9} ($+ 0.3 \times 10^{-9}$)		
THC (μM)	80.4 (- 1.8)		
Oxygen saturation (%)	69.8 (+ 0.4)		

5.3.3 Correlation between the measured parameters

Figure 5.4 demonstrates how measured physiological parameters are correlated with each other on a specific location (location 3). From this point on, the location is considered as a fixed effect in the LME fitting (see Section 5.2.4) leading to a positive correlation between blood flow

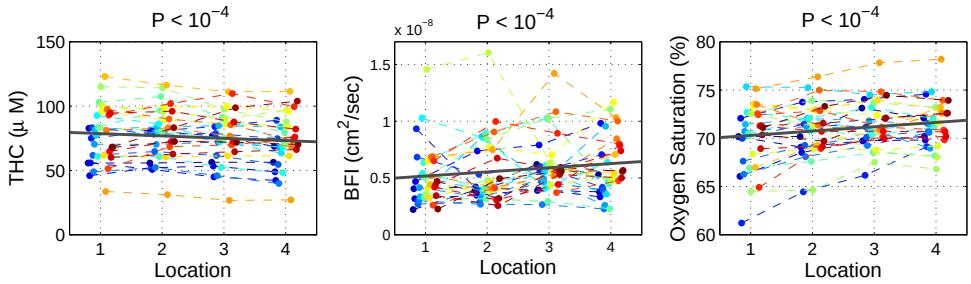

Fig. 5.3 Measured parameters for 32 subjects over 4 locations on manubrium. For clarity points are moved slightly along the x-axis ("dodging"). (Left) total hemoglobin concentration (μM). (Middle) blood flow index (cm^2/sec). (Right) oxygen saturation (%).

and total hemoglobin concentration (P = 0.01) yet the changes are small. Moreover, the subjects with higher blood flow have a higher blood oxygen saturation ($P < 10^{-4}$). The correlation between total hemoglobin concentration and oxygen saturation is not statistically significant (P = 0.1). In all the subsequent plots and analysis, we will focus on one of the central locations, location 3.

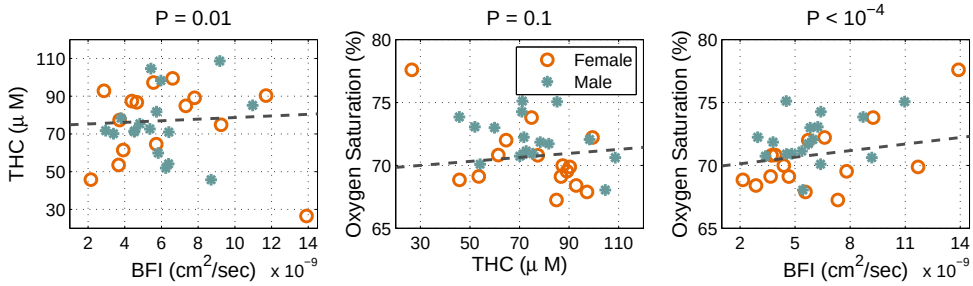

Fig. 5.4 Correlation between the measured physiological parameters. The plot represents measured values and the fitted line for the location 3 of the manubrium. (Left) Subjects with higher blood flow have higher total hemoglobin concentration. (Middle) Total hemoglobin concentration and oxygen saturation are not correlated. (Right) Subjects with higher blood flow have higher oxygen saturation.

5.3.4 The sensitivity of the measurement to the physical condition of the subjects

For each subject we have performed the skinfold measurement on the manubrium area to estimate the thickness of overlying tissue. As it is shown in Figure 5.5 there is a positive correlation between BMI and skin thickness, as may be expected, since the skinfold measurement includes the overlying adipose layer ($P < 10^{-4}$).

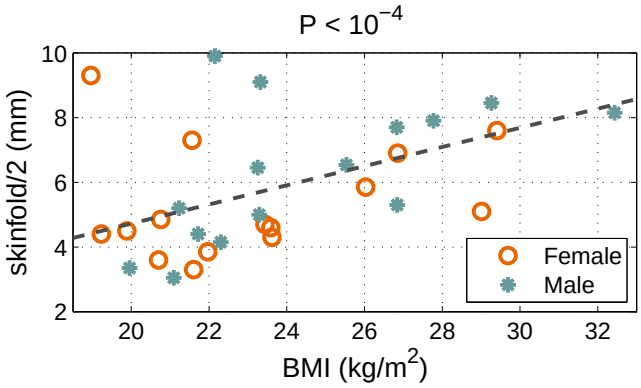

Fig. 5.5 There is a positive correlation between BMI and skinfold value on the manubrium ($P < 10^{-4}$).

Figure 5.6 compares the measured physiological parameters (THC, BFI, and oxygen saturation) with the thickness of overlying tissue (skinfold value) in a central location of the manubrium (location 3). None of the physiological parameters have shown a significant correlation to the skinfold value.

Figure 5.7 demonstrates that the measured THC and oxygen saturation are dependent on the BMI of the subject. There is a negative correlation between BMI and THC ($P < 10^{-4}$) and there is a positive correlation between BMI and the oxygen saturation ($P = 0.003$). Despite the correlations observed for the total hemoglobin concentration and the oxygen saturation, no correlation was observed between BMI

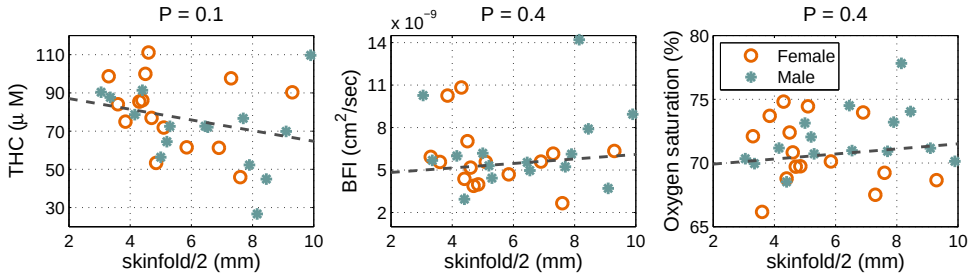

Fig. 5.6 There is no significant correlation between the skinfold value and (Left) total hemoglobin concentration. (Middle) blood flow index. (Right) oxygen saturation. The plot represents measured values and the fitted line for the location 3 of the manubrium.

and blood flow index. The plot represents measured values and the fitted line for the location 3 of the manubrium.

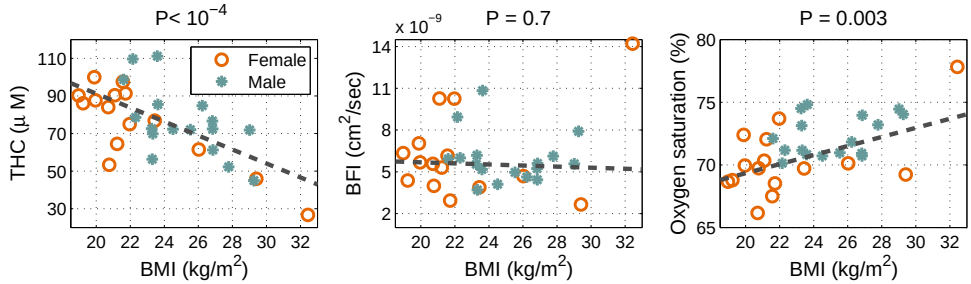

Fig. 5.7 (Left) BMI has a negative correlation with total hemoglobin concentration ($P < 10^{-4}$). (Middle) There is no significant correlation between BMI and the blood flow index ($P = 0.7$). (Right) BMI has a linear correlation with the oxygen saturation ($P = 0.003$). The plot represents measured values and the fitted line for the location 3 of the manubrium.

5.3.5 The dependency of the physiological parameters on gender

To test the dependency of the physiological parameters on the gender, we have fitted an LME model to the data. If gender is considered as the only fixed effect then the oxygen saturation in the males is 2% higher than in the females. Since BMI is an influential parameter, and two genders have significantly different BMIs (Table 5.2), both BMI and gender were considered as the fixed effects. In this case there is no significant difference between genders on any of the measured parameters ($P = 0.4$). In figure 5.8 the box-plot of measured parameters for each gender is presented.

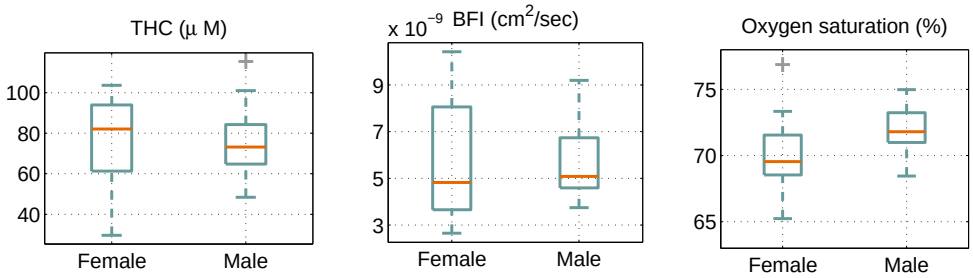

Fig. 5.8 The distribution of the measured physiological parameters by gender. (Left) total hemoglobin concentration, (Middle) blood flow index (BFI), (Right) blood oxygen saturation.

5.3.6 The dependency of the physiological parameters on age

We have chosen the subjects from a controlled range of age (24-42 years) to try to avoid the dependency of the measurement on the age of subjects. Figure 5.9 demonstrates that in the collected range of ages the measure physiological parameters do not depend on the age.

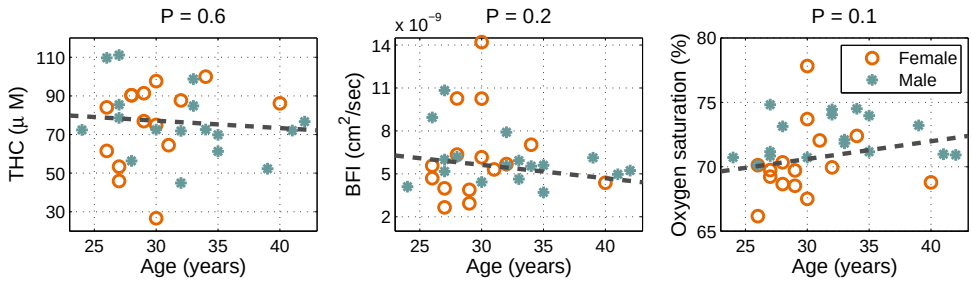

Fig. 5.9 There is no significant correlation between age and (Left) total hemoglobin concentration. (Middle) blood flow index. (Right) oxygen saturation. The plot represents measured values and the fitted line for the location 3 of the manubrium.

5.4 Discussions

In this work, we have studied the optical and physiological properties of the healthy manubrium bone as a site indicative of the red bone marrow hemodynamics in the body. We first discuss the quality of the measurements and whether the bone marrow is the main contributor to our optical signal. Then the distribution of the measured parameters on the healthy subjects is reviewed, the sensitivity of measured parameters to the location of probe on the manubrium is discussed and the correlation between measured physiological parameters and characteristics of subjects such as BMI, skinfold value, age and gender is investigated.

The quality of the measurements and the probed tissue volume: In each measurement, an experienced hematologist located the manubrium and guided the placement of the probe. We were able to obtain data with sufficient signal-to-noise ratio from each measurement and the fitting for both DCS and TRS device had good quality indicating that the data fits the model well and there are no systematic deviations from the model. The source-detector separations were 25 mm for both modalities.

Manubrium is a superficial tissue that does not have any overlying muscle. Its average size is 50×50 mm^2 with thickness of ≈ 11.2 mm in females and ≈ 12.6 mm in males [280]. The manubrium is not homogeneous in thickness and these numbers were measured on two points which represent the average of extreme values (thinnest and thickest part) of the manubrium. The thickness of combined skin and the manubrium is approximately 15.6 mm and 17.7 mm respectively for females and males. On average, the depth of optical penetration with our probe is greater than the thickness of the skin and less than the combined thickness of the skin and the manubrium. However it has been reported that manubrium in the thinnest part can be less than 10 mm [281, 282]. To study this point we have simulated a medium (data not shown) with similar optical properties as manubrium and we have calculated the probability of detecting a photon which has penetrated a certain depth. We observe that less than 20% of detected photons had penetrated more than 1 cm assuming a homogeneous medium. However, due to the presence of thymus and large vessels below the manubrium we expect a lower contribution to our signals. Finally, change of μ_a between 2 consecutive locations, on average, is $\sim$3% (Table 4). We know that manubrium is thickest on the location 1 and narrower in locations 2-3, and again gets thicker in location 4. However, μ_a drops unidirectional from location 1 to 4. This suggests that in thinner parts we are not probing different tissue. This small yet significant location dependency is not due to variation in thickness. Therefore, it is a reasonable assumption to consider manubrium bone and its rich red bone-marrow content as the the dominant contributor to our signal.

Furthermore, to double check this assumption, for one subject, we have located the manubrium by an ultrasound and compared its dimensions to the average which was well within the average and to the borders defined by the hematologist. Two sets of data were taken, one based

on the hematologist's assumptions and one guided by the ultrasound. The measured parameters in both cases did not show any significant differences (data not shown).

The distribution of the measured parameters: Bone is a relatively understudied organ for diffuse optics. It is often considered a nuisance, for example, when dealing with the measurements on the adult head [47, 51]. However, a few groups have measured *in vivo* human bones to investigate absolute values of μ_a and $\mu_s{}'$ [144, 153, 269]. The first study [153] has investigated the calcaneus bone ($\mu_a \approx 0.07$ and $\mu_s{}' \approx 14$ (cm^{-1}) for $\lambda = 785$ nm), and the second one [269] has measured the finger bone ($\mu_a \approx 0.20 - 0.25$ and $\mu_s{}' \approx 20 - 25$ (cm^{-1}) for $\lambda = 785$ nm). The last study [144] has investigated the patella bone and they have reported $\mu_a \approx 0.035$ and $\mu_s{}' \approx 5.4$ (cm^{-1}) for $\lambda = 785$ nm. The reported μ_a, $\mu_s{}'$ in this study ($\mu_a \approx 0.15$ and $\mu_s{}' \approx 9.6$ (cm^{-1}) for $\lambda = 785$ nm) is in the range of the previous measurements but, we note that, the reported values from different studies cover a wide range. This may be due to differences in the tissue and bone structure in different sites and also the limited number of subjects in all studies.

Absorption coefficient and the physiological parameters derived from it (total hemoglobin concentration and oxygen saturation) have normal distributions. The median of THC value is 77.3 (μM) with the quartile range (QR) of 62.2-88.6 (μM). This value is much higher than the measured THC in patella bone ($\approx 18\mu M$) [144]. It can be explained by the higher red marrow cellularity in manubrium in comparison to the patella. Since hematopoietic tissue is physiologically more active compared to compact bone, it has a wider vasculature niche, i.e. is better perfused, to provide it with oxygen and nutrition. Higher vascular level of the manubrium suggests higher THC values and our measurements confirm it. The median oxygen saturation of all subjects is 71.1% (QR:69.5-72.3%) which is in the range of the oxygen saturation observed

in the patella.

In contradiction to other parameters, the blood flow index does not show a normal distribution. This might be partially due to the relatively higher standard deviation of the absolute values from the DCS measurements or it may reflect the underlying physiology. We note that an overwhelming majority of the DCS studies, to date, have reported relative changes in blood flow with respect to a reference tissue or time point since the DCS results depend on the optical parameters of the tissue [2, 26, 47, 170]. Our study stands out in this aspect since we use the TRS values for more accurate analysis of the DCS data. However, DCS is a highly sensitive measurement of the local blood flow, and, in soft tissues, this may depend on the probe pressure as was documented for the scalp by [283]. We discuss this point further in the following paragraphs.

The knowledge about the range of the measured physiological parameters and their distribution enables us to define the healthy range to detect the subjects with high risk of hematological malignancies since a high proliferating activity of the hemopoietic tissue due to malignancy is related to angiogenesis [229–231] and can cause high hemoglobin concentration or high blood flow in the bone marrow. This will be the topic of our future studies.

One shortcoming of our study is that we have assumed water, oxy-, and deoxy-hemoglobin as the only major absorbers due the limited number of wavelengths that were utilized. In fact, the water concentration was kept constant at 30% [274]. Other significant absorbers in manubrium could be the lipids and the bone mineral which were not considered in the above analysis. Errors in these estimates could effect the derived parameters such as the total hemoglobin concentration and the blood oxygen saturation.

To further investigate this point, we have calculated the hemoglobin

concentrations for different assumptions of lipid and bone concentrations started from 5%, since assuming lower than 5% of lipid and bone does not practically change any of measured values. It has been shown [272, 284] that bone marrow is made up of $\sim 30-40\%$ fat in the people with same age range as the subjects of this study. To study more extreme cases we have assumed 50% fat for the upper limit of the assumed fat concentration. Previous, studies on sternum have demonstrated that it has less than 14% bone mineral in healthy subjects [285]. Here we have assumed 20% as the upper range for the mineral concentration. The spectra of the lipid and the bone mineral were obtained from Ref. [286] and Ref. [153] respectively.

Table 5.5 The effect of assuming different concentrations of lipid and bone mineral on total hemoglobin concentration and blood oxygen saturation calculations.

	THC (μM)	Oxygen saturation (%)
Only water	77.3 (62.2, 88.6)	71.1 (69.5, 72.3)
Lipid 5%	77.1 (62.4, 88.5)	71.1 (69.4, 72.3)
Lipid 50%	75.7 (60.7, 87.1)	70.7 (69.0, 72.0)
Bone 5%	76.4 (61.3, 87.7)	71.4 (69.8, 72.6)
Bone 20%	73.6 (58.6, 85.0)	72.2 (70.7, 73.6)

Manubrium is mostly red marrow with a soft and spongy inner structure which suggests that it has a low concentration of bone mineral [271, 285]. However, even assumption of 20% bone mineral does not introduce a significant difference in the distribution of measured hemoglobin concentration ($P = 0.4$) and the averaged change in the oxygen saturation is less than 1.5%. In a study on an elder group of people (67–101 years) who are expected to have a higher fat content (fat content increases by aging), the average percentage of measured fat

was 50% [284]. It demonstrates that assuming 50% as the upper limit is a reasonable assumption. Even the extreme assumption of 50% for fat content does not change significantly the distribution of measured hemoglobin concentration (P = 0.7) and oxygen saturation (P = 0.5). Table 5.5 demonstrates that assumptions of extreme values for bone or mineral concentration changes the measured THC in the range of 73.6-77.3 μM and oxygen saturation between 70.7-72.2%. For all assumed concentrations of lipid and bone, both THC and blood oxygen saturation are normally distributed.

The dependency of the measured parameters on the probe location: As it was mentioned the height of manubrium was divided to four locations and we measured the locations from top to bottom (location 1-4). The measured parameters have a slight change over the first to last location of probe (see Table 5.4). Although the change is statistically significant, it is less than 5% (between two locations).

Since all the measurements were done in the same order, to test the repeatability of the measurements when the order is changed, we have repeated the measurements on two subjects. Here, we measured the manubrium four times per subject; two measurements top to bottom and two measurements bottom to up. The results indicate that the measurement order is not an effective parameter (Figure 5.10).

Small dependency of the measured value on the location of probe suggests that in the next series of measurement on the healthy or malignant manubrium very precise locating of probe is not necessary. We can approximately put the probe on the center of manubrium. Since the measured values do not depend on the order of measurement, we can relocate the probe couple of times to have an average value of all positions near to center of manubrium for each subject.

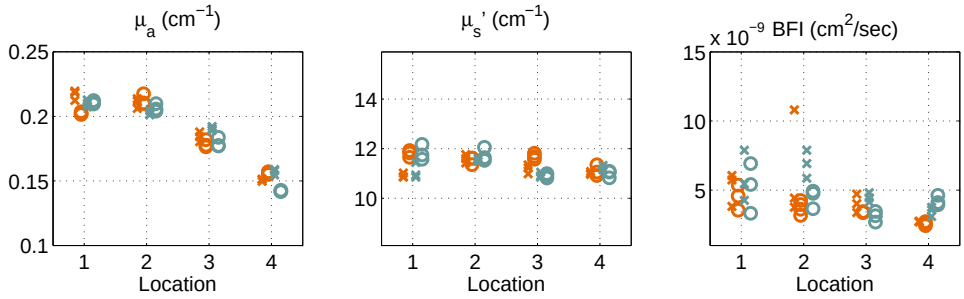

Fig. 5.10 Four measurements on four locations. Crosses are measurements from top to bottom and circles are representing measurements from bottom to top. Orange is the first measurement and blue the second time. The plot demonstrate the independency of the results on the order of measurements. (Left) Absorption coefficient. (Middle) Scattering coefficient. (Right) Blood flow index.

Correlations between the measured parameters: Figure 5.4 demonstrates the correlation between measured physiological parameters. Oxygen saturation and hemoglobin concentration increases (however the change is small) when the blood flow increases. These are within expectations. The lack of or small correlation between parameters reflects the differences in the baseline metabolism of the subjects. It strengthens our motivation to use hybrid diffuse optics for this study.

The sensitivity of the measurement on the overlying tissue and the pressure on it: In this measurement the skin-fat tissue is a non-desirable volume that is located between the optical probe and the manubrium. We try to minimize the partial volume effect of this superficial tissue. The partial volume effect problem in this study is similar to the brain measurements with less complication, because in the brain measurements there are several non-desirable layers (skin-fat, skull and cerebrospinal fluid) some of which (skull) are not directly accessible. Despite all these layers the penetration of near infrared light in the brain

is well-validated [47]. [283] demonstrated that the application of pressure to the optical probe (which is transmitted to the tissue in contact with the probe) would alter the partial volume effect contributions from the scalp and minimize them at the highest pressures. With the goal of minimizing the partial volume effect we have have applied high (but still comfortable) probe pressures. The target tissue in this study is a bone. While the probe pressure compresses the overlying tissue and alters the hemodynamics, due to the rigid structure of the manubrium we do not expect its hemodynamics to be affected by pressure. Furthermore, we have tested the effect of probe pressure on the manubrium by putting a load sensor between the manubrium and optical probe (Figure 5.11).

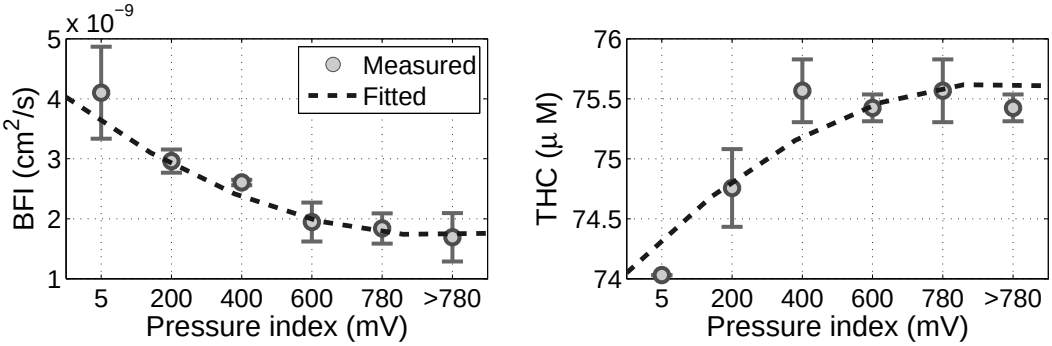

Fig. 5.11 The effect of probe pressure on the measurement of (Left) total hemoglobin concentration and (Right) blood flow index. In the low pressure regime the measured values are sensitive to the pressure increases until the pressure reaches to a threshold value. After the threshold, the increase in probe pressure does not change the measured THC or blood flow index.

In the low pressure condition, an increase in pressure led to a higher THC (lower BFI) up to a certain pressure threshold. The increased probe pressure "squeezes out" the superficial blood and, therefore, we probe a larger portion of the manubrium which has a higher THC than overlying tissue (skin and fat) and lower blood flow. This, in turn,

leads to the observed changes. After reaching the threshold, there is a plateau and pressure change does not affect the measured parameters. Therefore, in the measurement of subjects we kept the pressure at the highest possible, comfortable amount. Considering our probe design, fibers tips protrude out of the probe surface, presumably such a pressure compresses the overlying tissue on the measured area (Figure 5.1) and minimizes the skin effect. A future probe may include a calibrated load sensor to equalize this effect between subjects.

The sensitivity of the measurement to the physical condition of the subjects: Figure 5.6 demonstrates that the measured physiological parameters are not sensitive to the thickness of overlying tissue. On the other hand, skinfold values are highly correlated with BMI and people with higher BMI have lower hemoglobin concentration (Figure 5.7). This correlation can be explained by following two conjectures. First of all, it has been shown that bone mineral density (BMD) is decreased in people with higher BMI [287, 288], this decrease in BMD of bone marrow may reduce the measured absorption coefficient. As long as we are not considering bone mineral in our chromophores, this reduction is reflected in the measured hemoglobin and consequently make the THC and BMI correlated. Secondly, in a recent study [289] the correlation between serum lipid levels and bone marrow fat is observed. BMI and serum lipids also have positive correlation [290]. It can be concluded that in subjects with higher BMI, the red marrow cellularity would be lower. As red marrow is metabolically more active than marrow fat and is expected to have higher blood supply. Therefore, a lower THC is expected in the subjects with lower red marrow cellularity.

In Figure 5.6, one can observe a positive correlation between BMI and oxygen saturation. Since tissue with lower cellularity is physiologically less active, the oxygen consumption will be lower therefore the oxygen saturation increases.

However, to validate these hypotheses we need measurements with more wavelengths to be able to calculate the fat and bone mineral concentration for each subject individually. Then, we can investigate the correlation between BMI and lipid or bone concentration.

The dependency of the parameters on the gender of subjects: Optical parameters (μ_a and μ_s') as well as THC and BFI do not show any dependency on the gender of subjects while,as it is shown in figure 5.8, oxygen saturation in females is lower than males ($\approx 2\%$, $P = 0.02$). This observation can be explained as the effect of BMI on oxygen saturation. In Figure 5.7, it is shown that subjects with higher BMI have higher oxygen saturation. On the other hand, males have higher BMI in comparison to females (Table 5.2). Since BMI can influence the saturation and genders are different in BMI, we should rule out the effect of BMI. We have performed this by fitting an LME in which has BMI in addition to the gender and location of the probe as fixed effects. The results demonstrate that gender does not have a significant difference in oxygen saturation and BMI is the dominant parameter.

The dependency of parameters on the age of the subjects: Although hematological malignancies are the most common cancer in children and adolescents, due to ethical concerns we did not measure on this group of subjects. The effect of aging on the composition of bone marrow is well studied [272, 273, 291]. In this study, we have measured a narrow range of age (24-42) in order to avoid any significant dependency of measured parameters on age. The correlation plots also shows that the chosen range of age is tight enough to have no significant correlation between measured optical parameters and age.

Outlook to the future: This study aimed to characterize the optical and physiological properties of healthy bone marrow with the goal of

applying diffuse optics to study hematological malignancies. In the future, regarding this goal, we will characterize the same tissue on a group of patients with a specific type of hematological malignancy. The distribution of measured parameters on the healthy tissue will be compared with the the distribution on the malignant tissue. It is also interesting to observe the effect of antiangiogenic therapy on the measured parameters.

5.5 Conclusion

Since hematological malignancies affect the red bone marrow, we have sought to investigate a noninvasive optical technique for the manubrium as a site, rich of red bone marrow in the adults. For the first time, we have characterized the optical and hemodynamics properties of the manubrium in thirty-two healthy subjects using TRS and DCS. This study is the first step in the path of applying optics for the studies on bone marrow cancer. The distribution of optical and physiological parameters in the healthy bone marrow is demonstrated. Measuring the same parameters in the patients with hematological malignancies will illustrate the difference between distribution of measured parameters on the healthy and malignant marrow. It can be applied for screening purposes to detect subjects with high risk of hematological malignancies. We can also monitor to changes in optical and physiological parameters induced by antiangiogenic therapies to predict the effect of treatment and personalize the therapy.

Chapter 6

Hemodynamics of the human patella during rest and cuff inflation

6.1 Introduction

Tissue vascularization and local micro-vascular hemodynamics play a vital role in the health of the skeletal system. Noninvasive, quantitative and practical measurements of hemoglobin concentration, blood oxygenation, blood flow and metabolism in the bones could improve our fundamental understanding of bone function with potential applications in diagnosis and treatment of bone diseases [120–122]. However, due to the nature of the bone itself which is hard and covered by other tissues, it is difficult to investigate its circulation continuously, noninvasively and over long periods of time [250, 292]. Several groups have investigated the possibility to use near-infrared spectroscopy as a noninvasive technique to monitor hemodynamics of human bone [121, 122, 153, 255–257, 260, 261, 263, 264, 266–270]. Mechanical plethysmography is a technique based on measurement of the volume changes; applying ve-

nous occlusion to the arm causes arterial blood to enter to the forearm and accumulate there. It leads to a linear increase in the forearm volume over time. Based on a model, one can calculate the arterial flow by measuring the increased volume in a certain time interval [293]. It is a useful technique to study the bulk blood flow into an extremity.

Most of the studies that are mentioned above using near-infrared light had utilized a similar technique, photoplethysmography (PPG), to study the physiology and hemodynamics of bone. PPG is based on a simple, noninvasive device that can measure blood volume changes in the vasculature. It consists of light emitting diodes (LEDs) as source, and photodiodes as detector both working in the red or near infrared regime [294]. The emitted light interacts with tissue experiencing reflection, absorption, many scattering events, and even fluorescence [1]. The main absorbers are the hemoglobin species making the technique sensitive to the blood volume. The scattering of light, on the other hand, in tissue occurs at the cell membranes, vessel walls and at the boundaries of media with different refraction indices [295]. Therefore, blood volume and vessel wall movements, by changing absorption and scattering of the underlying tissue, can alter the detected intensity in the detectors [294, 296]. In fact, the measured PPG signal has both fluctuating ("AC") and static ("DC") components. AC is the pulsatile component and its frequency depends on the subject's heart-rate. In each cardiac cycle, the heart pumps blood into the arteries which causes increased blood volume and vessel wall movements in arterial and venous blood vessels. These changes originate the "AC" component of the PPG signal. The amplitude of the "AC" component depends on the vascular distensibility [297]. Furthermore, since oxygenated hemoglobin has a different absorption spectrum than the deoxygenated hemoglobin, .changes in blood saturation causes unequal alterations in different wavelengths. This enables PPG to follow changes in the arterial, pulsatile,

blood oxygen saturation.

The DC component varies slowly due to slow changes in scattering and absorption of tissue induced by respiration, metabolism, blood pressure or any other vasomotor activities [294]. Since specific diseases change the shape of the PPG signal, PPG can be applied to diagnose vascular diseases [298]. The potential of PPG as a diagnosis tool was noticed decades ago where measured blood volume changes by PPG was validated with simultaneous mechanical plethysmography measurement [299].

Recently some studies [121, 266, 267] have assumed another possible source for the pulsatile PPG signal from the bones; the changes in the orientation of the light scatterers, in this case the red blood cells (RBCs). They have reached this conclusion by assuming that the blood vessels in the bones do not have the possibility to change in size as bones are rigid structures. Therefore, they have suggested that the observed pulsations in the recorded light intensity from the bone measurements are due to the changes in the RBC orientations caused by blood flow changes over each cardiac cycle. Based on these results, they have applied PPG to measure blood flow changes in rigid structures such as bones [121, 266, 267]. Further experiments have confirmed this hypothesis for different human bones [254] where it was shown that the RBC count that was estimated by large source-detector separation laser Doppler flowmetry (LDF) does not change during heart pulsations while blood speed is altered. In this work, we investigate this hypothesis using a state-of-the-art frequency domain near infrared spectrometer (FD-NIRS) [140, 300] which can separate the absorption (μ_a) and scattering ($\mu_s{}'$) coefficients on the human patella. Patella is the most superficial part of the knee and since it does not have any muscle or other tissue (except skin) on top, the optical signal is dominated by the signals from this bone. In order to further confirm that the changes are due to arterial pulsations,

we apply an arterial cuff occlusion to the ipsilateral thigh. We also take advantage of the multi-wavelength system to quantify the changes in oxy- and deoxy-hemoglobin,and oxygen saturation during each cardiac cycle as well as the slower changes due to the cuff-occlusion. We compare our findings to those from the literature on leg muscles. The ultimate goal is to explore the possibility of using FD-NIRS to monitor bone hemodynamics noninvasively. The results of this study is published in Farzam et al. [144].

6.2 Methods & materials

6.2.1 Device and probe

We have used a customized, commercial frequency domain spectrometer (Imagent, ISS, USA, www.iss.com). The unit was customized to have fifteen laser sources at three wavelengths, i.e. groups of five lasers at ∼690, ∼785 and ∼830 nm that are intensity modulated at 110 MHz. Two photo multipliers (PMTs) are used to collect the light in the reflection geometry. For a review of the analysis methods for the frequency domain measurements that we utilize, see [2]. A self-calibrating probe (Figure 6.1) was utilized to obtain absolute values of the absorption and scattering coefficients at each wavelength [119]. All sources (S1, S2 ... S5) are located on the circumference of a circle with a radius of 1 cm. Detector D2 is at the center of the circle so it is at the same distance from all sources and, in ideal conditions, the intensity and the phase delay detected by D2 from all sources should be the same. Since the laser power, fiber transmissions, skin color and other factors are not the same in different source positions, the detected intensity and the phase-delay would be different. By considering one of the sources as the reference and assuming that the tissue is homogeneous, we can find calibration ("coupling coefficients") factors for all the other sources.

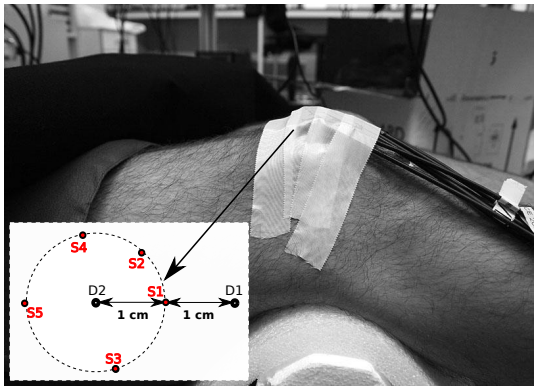

Fig. 6.1 The placement of the probe on the knee and the schematic of the self-calibrating probe with two detectors (D1, D2) and five sources (S1, S2 ... S5). The source-detector separations are from 1 to 3 cm in steps of 0.5cm.

Then these calibration factors are applied to the measured intensity and the phase delay by the main detector (D1) which is then utilized in a multi-distance fit as described below.

As shown in Figure 6.2, in order to synchronize the data acquisition with the heartbeat, the device was gated by the R-peak of the cardiac cycle from an electrocardiograph. At each trigger eight measurements, each an average of 14 acquisitions, were recorded during the cardiac cycle. This allowed us to average the pulsations from multiple cardiac cycles (up to 2000) without being dependent on the heart-rate being constant.

6.2.2 Measurement protocol

The measurements were performed on eight healthy male subjects (age 34.4 ± 9.6 years, body weight 77.6 ± 6.9 kg, and height 1.79 ± 0.07 m). Subjects were asked to lay supine and the optical probe was centered over the right patella and attached to the skin with medical tape. The

knee was bent 20 degree by means of an anatomical support placed under the popliteal fossa. A pressure cuff was placed around the right thigh. The subject's leg was then covered with a black blanket to avoid external light and to maintain a comfortable temperature. The three electrodes of the electrocardiograph (CardioLab4, Francesco Marazza, Hardware & software, Italy) were placed on the subject's chest.

The subject was asked to rest in this position for a minimum of 15 minutes before the measurements have started. The pulsatile component was studied during 30 minutes of additional rest after which the subject was allowed minimal motion for comfort. This thirty minute period is further utilized to estimate the average optical properties of the healthy patella. The second set of measurements were performed five minutes at rest and then five minutes of arterial occlusion with the cuff pressure set at 260 mmHg to ensure adequate blockage [301].

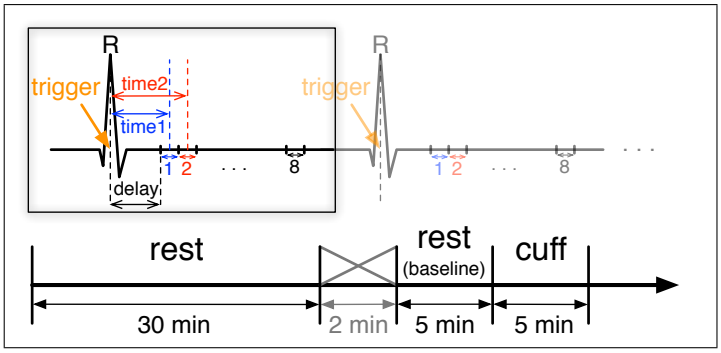

Fig. 6.2 Measurement protocol: 1) 30 minutes measurement of rest (no occlusion), 2) couple of minutes relaxing time for subject to adjust their leg, 3) 5 minutes measurements of rest as baseline (no occlusion), 4) 5 minutes cuff occlusion. The inset shows the triggering of the instrument by the "R-peak" and the eight measurements during each cardiac cycle.

6.2.3 Fitting method

Theory and calculations

We have utilized the frequency domain solutions of the photon diffusion equation in the semi-infinite geometry to obtain the wavelength (λ) and time (t) dependent optical properties of the tissue [2]. To calculate $\mu_a(\lambda, t)$ and $\mu_s{}'(\lambda, t)$ of the probed tissue volume, we fit this theory to the measured (and calibrated, see below) intensity and phase for each of the three wavelengths (690, 785, 830 nm) using a multi-distance approach. For more details look at chapter 2, section 2.4, equation 2.6. The measured absorption coefficients ($\mu_a(\lambda, t\ )$) are related to the different tissue chromophores as described at chapter 2, section 2.5, equation 2.10. Here we have assumed only water, oxy- and deoxy-hemoglobin the chromophores in the patella. The water concentration in the bone was assumed to be 15% [153, 274, 302] and oxy- and deoxy-hemoglobin concentrations were measured over time ($c_{HbO_2}(t)$ and $c_{Hb}(t)$). The total hemoglobin concentration (THC) was assumed to be sum of oxygenated and deoxygenated hemoglobin, i.e. $THC(t) = c_{HbO_2}(t) + c_{Hb}(t)$ and blood oxygen saturation ($SO_2(t) = \frac{c_{HbO_2}(t)}{c_{HbO_2}(t)+c_{Hb}(t)} \times 100$) were also calculated and reported.

Even though the frequency domain method is a well-validated and utilized method, we have tested our specific approach for self-calibration and our optimization codes using simulated data. We have simulated a medium with similar physiological properties to what we have measured on the knee–cap: THC = 20 μM, $SO_2 = 65\%$, and water concentration = 15% [153, 274, 302]. This results to μ_a = 0.042, 0.041 and 0.043 (cm^{-1}) respectively for 690, 785, and 830 nm. We also assumed that the simulated media has similar scattering properties to our values from knee measurements: $\mu_s{}'$ = 7.0, 5.0 and 4.0 (cm^{-1}) respectively for 690, 785, and 830 nm. The assumed probe geometry in this simulation is the geometry of utilized probe in the measurement of knee which is

described in Figure 6.1. Noise and random calibration coefficients were introduced to create a realistic numerical data set.

In order to test the self-calibration probe, a non-zero random number between zero and one was assigned for each source and each detector as a multiplicative amplitude calibration factor. Similarly, for phase, a random, additive calibration factor up to one radian was assumed. The simulated data for each of the source-detector pairs received these multiplicative and additive calibration factors.

Then, we have introduced random noise to the calculated in-phase and quadrature components of the simulated data. In order to estimate the required noise level for the simulation, we have studied a liquid phantom measurement with more than 2000 acquisitions. The measured noise in amplitude and phase are respectively 0.05% and 4.4×10^{-4} radian for an acquisition time of 10 $ms/channel$. The amplitude noise is in good agreement with the company specified value. Noise in the phase is proportional to the square root of acquisition time. In this study the acquisition time was 3.2 $ms/channel$. A simple calculation, gives the expected phase noise to be $\approx 7.7 \times 10^{-4}$. We have introduced 1% noise to in-phase and quadrature components of the simulated data, which produces a phase noise of $\approx 7.7 \times 10^{-3}$ and an amplitude noise of $\approx 1.7\%$. Therefore, the simulated noise in both phase and amplitude is greater than the expected values from the *in vivo* experiment. Thousand data sets were generated according to this algorithm, and we have fitted the theory to each of them separately.

The first step in the analysis was to apply the above-mentioned self-calibration method for the sources that are equidistant from one of the detectors. This allowed us to recover the relative values of all the source-calibration coefficients and introduce them to the measurements from the other detector.

The photon diffusion model is then fitted with μ_a and $\mu_s{}'$ as the

unknowns to this calibrated data by minimizing the χ^2 using non-linear least square curve fitting implemented by function "lsqcurvefit" in MATLAB (Mathworks Inc, Natick, Massachusetts, U.S.A.).

Figure 6.3 shows the results of this procedure from one example data-set. The left side shows the uncalibrated data where the effect of the calibration coefficients is visible. The middle shows the result of applying the self-calibration method where mainly the effect of the noise is visible. Overall, the result of the fitting (right column) is in good agreement with the simulated tissue properties with a less than 1% error in the calculated optical properties and the hemodynamics parameters. We have also tested the crosstalk between μ_a and $\mu_s{}'$ estimates by applying a small ($\approx 0.5\%$) change to either μ_a or $\mu_s{}'$ while the other was fixed in the simulated data. The result of fitting was precise enough to detect changes less than $\approx 0.5\%$ in one of them without seeing a cross-talk in the other. Finally, we have also applied changes to both μ_a and $\mu_s{}'$ (both increase, both decrease, one increases and the other decreases) of $\approx 0.5\%$ and the algorithm was able to separate the changes in μ_a and $\mu_s{}'$ in all of these conditions.

We note here that, despite this high level of noise (higher than the instrumental noise), the algorithm was able to resolve absorption and scattering changes from each other due to the large data-set (1000 simulations) which is the case for our studies. The real scenario has an order of magnitude less instrumental noise but more physiological noise (each cardiac cycle is not identical) and some uncertainties in the source-detector separations due to the use of a flexible probe.

Finally, in the *in vivo* data analysis, in the last step, we have removed outliers that are defined as having either the amplitude or phase more than four times the standard deviation of all points away from the mean. We have performed the removing procedure over each wavelength (3 wavelengths), each separation (5 separations) and each point (8 points)

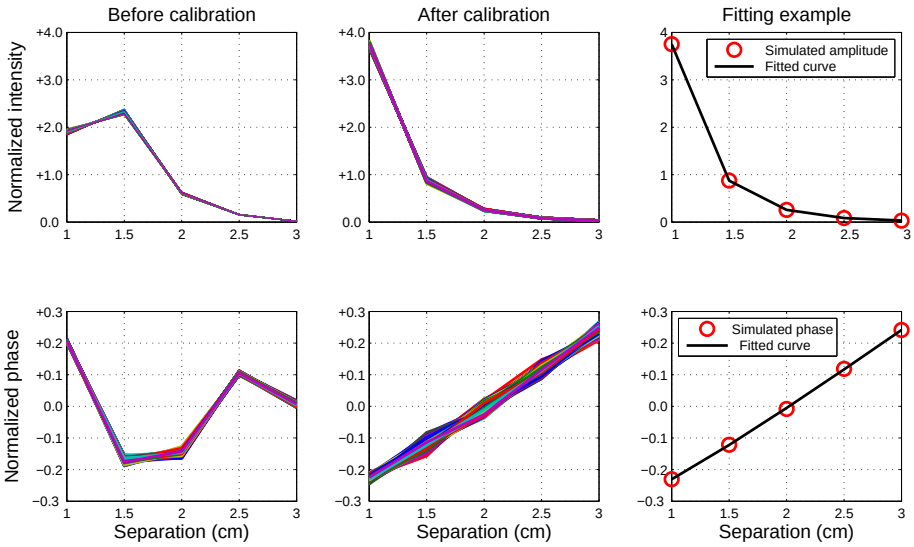

Fig. 6.3 Simulated phase and intensities ($\lambda = 690\ nm$) normalized by the mean value. Left-column: before calibration where each line corresponds to one simulated measurement. Middle-column: after self-calibration. Right-Column: demonstration of fitting quality on fitted one curve.

over all measurements (up to 2000 measurements). In case of detecting an outlier in any measurement the whole measurement (all separations, wavelengths and points corresponding to that measurement) has been removed.

6.2.4 Time-scale equalization

Even though we have gated the data acquisition by each heartbeat, since the heart-rates (HR) of different subjects are vastly different and the pulsatile changes in the signal are "squeezed" to fit these varying in-between cardiac cycles period ($Htime$ [ms]), we needed to take an additional step of a time-scale equalization in terms of the total fraction of $Htime$ for each measurement points. Furthermore, each measurement point ($n = 1, 2, \ldots, 8$) corresponds to a different cardiac cycle fraction (X_n).

There is a constant delay ($\approx 150\ ms$) between the ECG trigger and the start of measurement, which consists of the electronics delay and warm up time of the detectors. The duration of the measurement for each point is ≈ 48 ms. We assign each measurement to the middle of this 48 ms (See Figure 6.2). Therefore, each of the eight measurement point takes place at time (timen) given by $timen = ((n - 1/2) * 48 + 150)$ and corresponds to $X_n = \frac{timen}{Htime} = \frac{((n-1/2)*48+150)}{Htime}$. There after, each point is assigned to an X_n value where the maximal value, $X_8 = Hfraction$, corresponds to the maximal fraction of the in-between beats period. All data is reported in this time scale.

6.2.5 Statistical analysis

All the data were analyzed using a linear mixed effects (LME) model [275] using packages lme4 and languageR in R (open source statistical computing language, http://www.r-project.org). To assess the validity

of the mixed effects analyses, we have performed likelihood ratio tests comparing the models with fixed effects to the null models with only the random effects. We rejected results in which the model including fixed effects did not differ significantly from the null model. Throughout this chapter, we present Markov Chain Monte Carlo (MCMC-estimated) p-values that are considered significant at the $\alpha = 0.05$ level. For all fitted LMEs, the normality and homogeneity was checked by visual inspections of residuals against fitted values. The results of this study are reported in two main parts.

Hemodynamics response of the patella bone to cuff occlusion:
In this part the changes in THC (ratio) and oxygen saturation (difference) during baseline and cuff occlusion are reported. The transitional periods while the cuff was inflated/deflated were removed from the data. Then data during the baseline (denoted by BL, defined as the $\approx$ 5 minutes measurements during rest), at the immediate beginning of the cuff occlusion (denoted by CB, defined as the first 50 cardiac cycles immediately after the cuff occlusion) and at the end of the cuff occlusion (denoted by CE, defined as the last 50 cardiac cycles of the cuff occlusion periods) were calculated for each parameter. To assess changes in saturation and hemoglobin concentrations, we fit an LME model to data to compare different conditions (BL, CB, CE). In these analyzes BL was considered as the reference and changes were reported in comparison to it. While the condition was the fixed effect, subject was considered as the random effect. The intercept is the fitted value for the baseline and the slope shows the change in comparison to the baseline.

The pulsation of the optical and the physiological properties:
In this part of study, for all subjects, the change over time is assessed. To fit a model on the measured parameters, first all curves are normalized

by dividing each time point by the averaged value of the signal during the pulse – the ratio of change relative to mean is denoted with "r". In case of oxygen saturation and phase, the normalization is applied by subtracting the mean of the data during one pulse from each time point of the pulse – the change relative to mean is denoted by "Δ". Then, we have compared the shape of the normalized pulses to well characterized PPG signals. Each PPG signal has a pulse transit time (PTT), that varies between subjects, organs and even in different postures [294, 303]. After PTT, pulse rises to a peak (in some cases there is a dual-peak), and after the peak it falls down again. Since there is a time delay between start of a cardiac cycle and start of our measurement ($\approx$ the first 20% of whole cycle is missed), we do not observe PTT in our pulses. The pulse we measure starts from rising mode, meet one peak and falls down. After visual inspection of pulses and fitting different functions to them, we conclude that a sinusoidal function is sufficient to describe our signals. For each parameter we have defined a sinusoidal function to be fitted to the data from all subjects. We have applied a two step fitting. First, a sinusoidal function was fitted to data of all subjects (for each subject we averaged all pulses). We recorded the obtained phase (Φ_0). In the second step, we have defined a sinusoidal function with this known phase ($A\ sin(\Phi_0) + B$) to be used by LME. Since we are not interested in the specific shape of the cardiac cycle driven pulsations but rather their existence or absence, a sinusoidal function with two free parameters of amplitude (A) and intercept (B) is a reasonable approximation. We are most interested in whether the amplitude, A, is significantly different from zero. While the cardiac cycle fraction (time from start of a cardiac cycle) was the fixed effect, subjects were used as a random effect. We have confirmed the absence of a trend during cuff occlusion by fitting the same sinusoidal function and obtaining non-significant fits ($p > 0.05$). For each parameter we

report the measured change during one cardiac cycle by calculating the difference between maximum and minimum of fitted curve. Depending on subject heart-rate the measurement has started in different time of cardiac cycle.We have measured each subject from 150 ms after start of a cardiac cycle until 534 ms after start of cardiac cycle (Figure 6.2). We know that different subjects have different heart-rates. For example if a subject has 80 $\frac{beat}{min}$, then for him each cardiac cycle will take, on average, 750 ms. This implies that the moment we have started our measurement, it has been $\frac{150}{750} \rightarrow 20\%$ of a cardiac cycle. We will continue until 534 ms after the start of cardiac cycle which means $\frac{534}{600} \rightarrow\sim 70\%$ of cardiac cycle. Therefore, for this subject our measurement covers $20 - 70\%$ of his cardiac cycle. In different subjects, based on their heart-rate the measured range of their cardiac cycle is different. The conversion of each point to the corresponding cardiac cycle percentage is explained in section 2.4. Different cardiac cycle fractions in the start point of different subjects makes it non-trivial to define the beginning of the fitted line. We averaged the start points of all subjects and the fitting has started from the average value.

6.3 Results

An example fitting quality: Figure 6.4 shows an example of the fitted theory to the measured data from a representative subject at $\lambda = 690$ nm. The residuals are also shown indicating that the calibrated data fits the model reasonably well without any systematic deviations from the model. These fits were applied to all data points individually for each pulsation resolved data.

The characterization of the optical and physiological properties of the patella (knee-cap bone): The absolute values of mea-

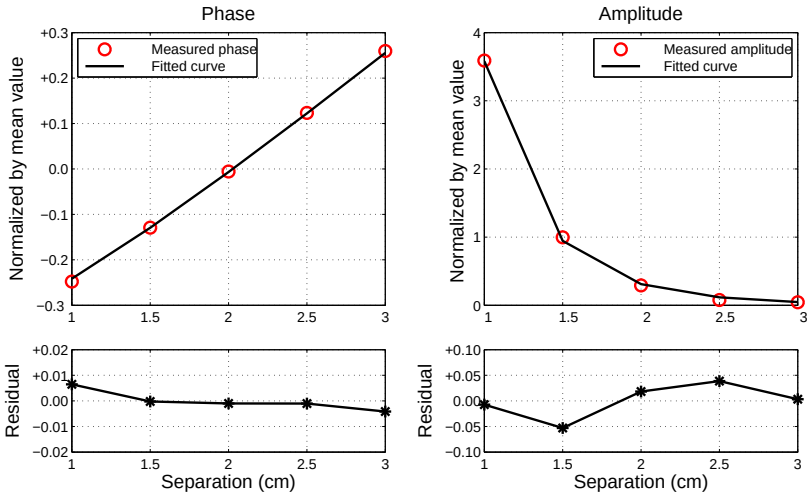

Fig. 6.4 An example of the fitted theory to the measured data from a representative subject at $\lambda = 690\ nm$. (Top) The normalized phase and amplitude and the fitted curves. (Bottom) The residuals of the fits indicating that the fits are accurate without a systematic error.

sured absorption and scattering coefficients for three wavelengths (690, 785, and 830 nm) are reported in Table 6.1. The values are averaged over eight subjects and the reported error is the standard deviation. As mentioned in the measurement protocol, all eight subjects were measured for $\approx$ 30 minutes of rest, the reported values are the averages of this time range ($\approx$ 30 minutes). In Table 6.1 the calculated values for total hemoglobin concentration and tissue oxygen saturation is reported. The measured μ_a, μ_s', THC, and SO_2 for each subject are listed in the Appendix D (Table D.1, Table D.2 and Table D.3). We have also reported the μ_a and μ_s' values after $\approx$ 4 minutes of cuff occlusion in Table D.4 and Table D.5 in the Appendix D.

The hemodynamics response of the patella to thigh cuff occlusion: Figure 6.5 shows the typical response to cuff occlusion. Oxygen

Table 6.1 The measured values of μ_a and $\mu_s{}'$ (three wavelengths), total hemoglobin concentration (THC) and oxygen saturation (SO_2) averaged over 8 subjects.

	$\lambda = 690$ nm	$\lambda = 785$ nm	$\lambda = 830$ nm
μ_a (cm^{-1})	0.038 ± 0.009	0.035 ± 0.009	0.044 ± 0.009
$\mu_s{}'$ (cm^{-1})	7.4 ± 0.8	5.4 ± 0.8	4.4 ± 0.8
THC (μM)		18 ± 4	
SO_2 (%)		65 ± 9	

saturation slightly increases after the inflation starts – presumably due to slow inflation of the cuff where the venous output is first occluded allowing inflow of arterial blood for a brief time period – and after full occlusion it drops gradually. We characterize the response according to the three periods (BL, CB and CE) as described above. When comparing the BL period, and CB, i.e. the first 50 cardiac cycles, oxygen saturation shows 3.4% increase ($p < 0.0001$) with a confidence interval (CI) of 2.8-4.0%. Although in the beginning of cuff, saturation increases, comparing BL and CE shows 8.2% (CI:7.6-8.8%) decrease in oxygen saturation at the end of the occlusion. In comparison between CB and CE, there is 11.6% (CI:12.4-10.8%) decrease in oxygen saturation during cuff occlusion.

As Figure 6.5 demonstrates that, in general, the application of the cuff causes a considerable increase. Comparing BL to CB, THC increases 13.5 μM ($CI = 12.9 - 14.1,\ p < 0.0001$). The comparison of BL to CE period, THC increase is 16.1 μM ($CI = 15.4 - 16.7,\ p < 0.0001$). THC change from CB to CE is 2.5 μM ($CI = 1.7 - 3.3,\ p < 0.0001$) which shows a slow increase during cuff inflation. The μ_a and μ_s' values after $\approx$ 4 minutes of cuff occlusion is reported in Table D.4 and Table D.5 in the Appendix.

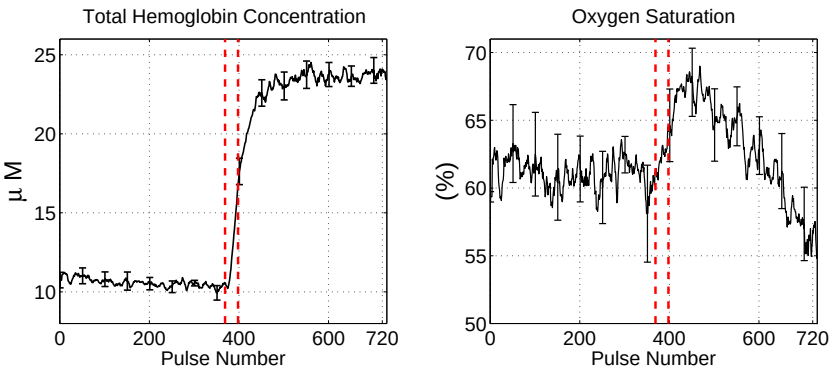

Fig. 6.5 Representative data showing the hemodynamic changes of the patella during cuff-occlusion. Vertical dashed lines from left:1^{st}– start of inflation, 2^{nd}– end of inflation. From pulse zero to the first vertical dashed line corresponds to 5 minutes, and from the first vertical dashed line to last pulse, corresponds to 5 minutes of occlusion.

The pulsatile behavior of the optical and physiological parameters during rest and arterial-occlusion: Figure 6.6 illustrates the average raw data from a representative subject . We have observed a clear pulsation of the AC amplitude ($p < 0.001$) but no significant changes in phase during rest (Left-column, $p = 0.337$). We have attributed the origin of the pulsations of the data to the cardiac cycle using the leg cuff occlusion data (right column), where, as expected, the pulsations disappeared ($p = 0.273$ & $p = 0.123$ respectively for AC amplitude and phase during cuff).

Figure 6.7 shows the pulsation of $\mu_a(t)$ and $\mu_s'(t)$ ($\lambda = 690\ nm$) during a cardiac cycle period. Dashed lines represent the behavior of each subject where for each subject all pulses were averaged. Solid line is the LME fit with the sinusoidal equation to the data of all subjects and pulses. In these figures all pulses are normalized by the mean value. Considering p-values of each fit, there are significant pulsations in both μ_a and μ_s' during rest, and applying the cuff removes the pulsations –

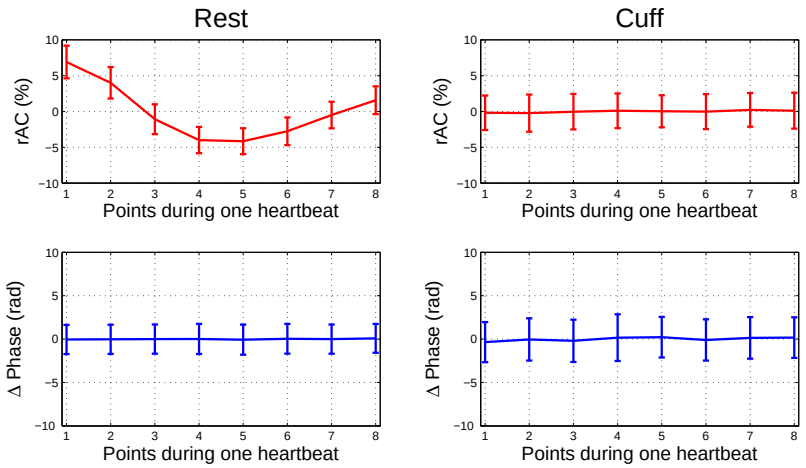

Fig. 6.6 An example of measured amplitude and phase between two consecutive pulses for $\lambda = 830$ nm and source–detector = 2cm. In this figure, the data for each pulse is normalized by the mean value, and the average of all normalized pulses is plotted. Top-left: pulsation of the AC amplitude during rest (AC amplitude decreases up to 10%), Top-right: by applying the cuff occlusion the pulsation of the AC amplitude disappears. that confirms the physiological origin of pulsations as arterial pulsations. Bottom-row: There is no pulsation in the phase during rest (left) or during occlusion (right).

there are just noisy fluctuations. Table 6.2 summarizes the changes observed in the optical properties for all three wavelengths. The reported change is the subtraction of the maximum and minimum (the minimum occurs in the first point) of the fitted sinusoidal curve. Although there are significant pulsatile behavior visible for μ_s' during rest, its amplitude is up to a factor of ten smaller than μ_a. Since subjects have different beginning of measurement (depending on their heart-rate, look at section 2.4.), defining the start of fitted curve is not trivial. Here, we have averaged beginning time of all subjects and considered the averaged value as the beginning of the fitted curve.

Table 6.2 Maximum change in fitted sinusoidal during the averaged measured cardiac cycle for all subjects for both μ_a and μ_s' in three wavelength (rest). There is no significant change in μ_a and μ_s' during cuff inflation (NA = Not Applicable).

	Rest			Cuff		
λ (nm)	690	785	830	690	785	830
$r\mu_a$	1.6% $P < 0.0001^*$	2.5% $P < 0.0001^*$	3.5% $P < 0.0001^*$	NA $P = 0.15$	NA $P = 0.57$	NA $P = 0.07$
$r\mu_s'$	0.3% $P < 0.0001^*$	0.5% $P < 0.0001^*$	0.3% $P < 0.0001^*$	NA $P = 0.62$	NA $P = 0.52$	NA $P = 0.99$
rTHC	3.1% ($P < 0.0001^*$)			NA ($P = 0.06$)		
ΔSO_2	0.7% ($P < 0.0001^*$)			NA ($P = 0.52$)		

* Significant pulsation.

Figure 6.8 shows the pulsations in the oxygen saturation and THC. In the rest period, THC increases by 3.1%, and oxygen saturation increases by 0.7% , while during occlusion the pulsation disappears and only noisy fluctuations are observed. The disappearance of the pulsation by applying cuff occlusion suggests that the origin of the observed

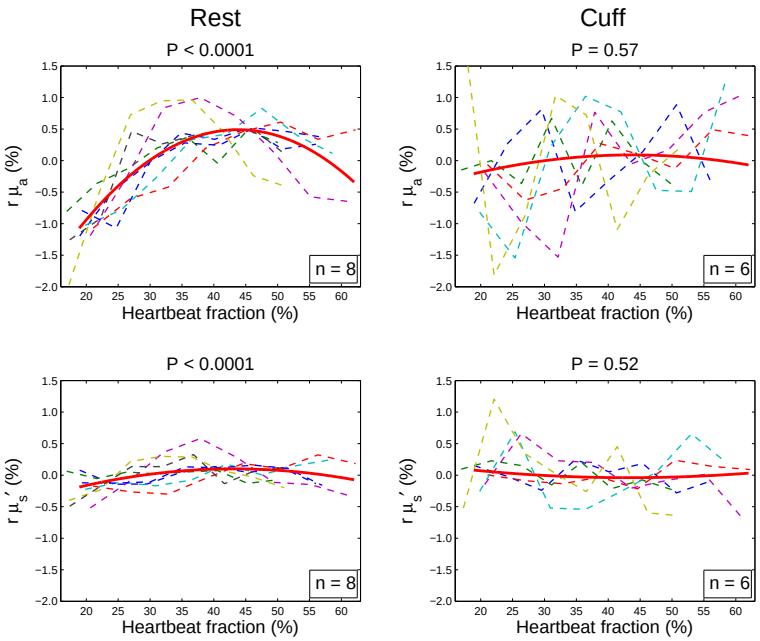

Fig. 6.7 The pulsation of $r\mu_s{}'$ and $r\mu_a$ at $\lambda = 690\ nm$ during measured fraction of a cardiac cycle at rest and noisy fluctuations of these parameters during cuff occlusion. Dashed lines are the average of all pulses for each subject and the solid line is the LME fit to all subjects and pulses. Top-left: pulsation of $r\mu_a$ during rest. Bottom-left: The pulsation of $r\mu_s{}'$ during cardiac cycle. Although it is much smaller than $r\mu_a$, it is statistically significant. Top-right: There is no pulsation in $r\mu_a$ during cuff occlusion. Bottom-right: There is no pulsation in $r\mu_s{}'$ during cuff inflation (n = number of subjects).

pulsations is the cardiac cycle.

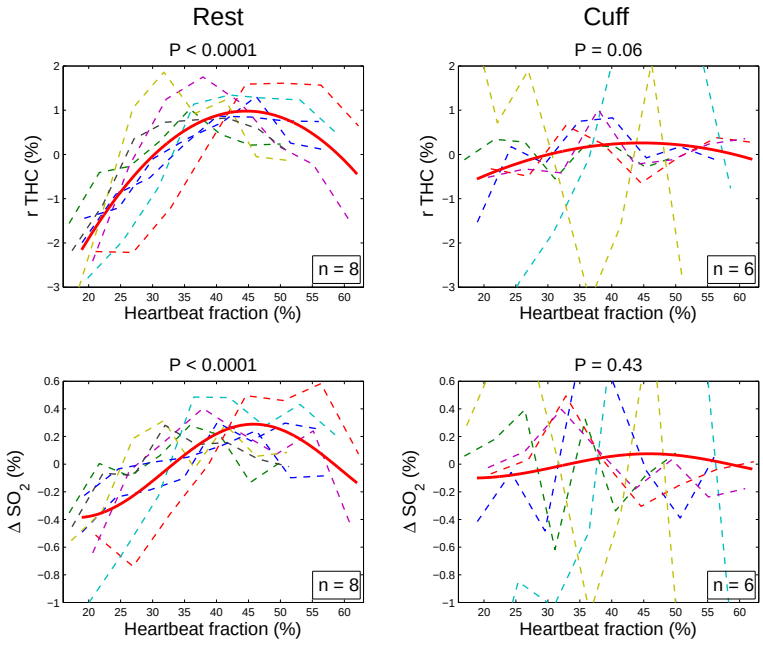

Fig. 6.8 The pulsation of rTHC and ΔSO_2 during rest and the noisy fluctuation of these parameters in occlusion time. Dashed lines are the average of all pulses for each subject and solid line is the LME sinusoidal fit to all subjects and pulses. Left: pulsation of rTHC and ΔSO_2 during rest. Right: The disappearance of the pulsation by applying cuff occlusion suggests that the origin of the measured pulsations is the cardiac cycle. n = number of subjects.

6.4 Discussion

In this work, we study the optical and physiological properties of the healthy patella bone, their pulsatile behavior in response to the cardiac cycle and their response to full arterial cuff occlusion. We now compare our study to previous reports. A few groups have measured *in vivo*

human bone tissue to investigate absolute values of μ_a and μ_s' [153, 269]. The first study has investigated the calcaneus ($\mu_a \approx 0.07$ and $\mu_s' \approx 14$ $(1/cm)$ for $\lambda = 785$ nm), and the second one has measured the finger bone ($\mu_a \approx 0.20 - 0.25$ and $\mu_s' \approx 20 - 25$ $(1/cm)$ for $\lambda = 785$ nm). The reported μ_a , μ_s' in these studies are higher than what we have observed ($\mu_a \approx 0.035$ and $\mu_s' \approx 5.4$ $(1/cm)$ for $\lambda = 785$ nm). This may be due to differences in the tissue and bone structure in different sites. The subject numbers are quite limited in all studies (including ours) and the methods are different. We stress that our findings are in the general ranges observed in healthy tissues and bones.

One of the main challenges in this study is to prove that the signals are indeed originating mainly from the bone and not the skin or other superficial tissues below the probe. This hypothesis has been studied by Naslund et al. [266] on the patella bone and it has been shown that if the source-detector separation is large enough (in their study it is 2.5 cm) and the wavelength belongs to near infrared regime (in this regime photons will experience many scattering events and the penetration depth is higher), the signal is not sensitive to the superficial tissue – the harmonic DC change due to autoregulatory activity disappears [266].

In our case, the source-detector separations varied between $10 - 30$ mm and an average patella is 45×34 mm^2 with ≈ 22.5 mm thickness [304]. Therefore, it is a reasonable assumption to consider patella bone as the dominant contributor to our signals. Roughly, the depth of optical penetration with our probe is greater than the thickness of the skin and less than the combined thickness of the skin and the patella, i.e. we are probing a tissue volume which does not extend below the patella. In the analysis we use all source–detector separations to fit the theory to the measured amplitude and phase (look at Figure 6.4). Therefore we can not compare the results of small and large separations, and only raw data

comparison is possible. The qualitative analysis of the raw amplitude data from the shortest and longest source–detector separations did not reveal any difference beyond those expected by the physics of the photon diffusion model. Detailed analysis of this is beyond the scope of this study.

We have reported our findings in two main parts, the pulsatile behavior of the patella and its response to the cuff occlusion. We now discuss the result of each part separately.

Pulsatile behavior of the optical and physiological parameters: Our focus was to investigate whether there were any changes in the absorption and the reduced scattering coefficients at all wavelengths that were suggestive of being related to the cardiac cycle. We have also investigated the resulting changes (or lack of it) in blood oxygen saturation and hemoglobin concentration.

In normal conditions, i.e. during non-occluded resting periods, a pulsatile behavior was detected in the AC amplitude. The pulsatile behavior of measured AC amplitude disappeared by applying cuff occlusion. When the cuff pressure is much higher than the arterial pressure, the arterial blood does not enter the tissue below the occluded part; then we can hypothesize that there should not be any pulsations in the signals that are related to the cardiac cycle. We have applied a cuff pressure of 260 mmHg. Since the pressure that tourniquet applies to the tissue is higher than systolic pressure, it will block the blood flow and is equivalent to full occlusion [301]. In our measurements, the pulsation of the AC amplitude disappeared during occlusion and the cardiac-cycle origin of the observed pulsatile behavior has been confirmed. The phase did not show any pulsation during rest or cuff.

The photon diffusion model tells us that the phase-delay has a direct relation with $\mu_s{}'$ increase and a reverse relation with μ_a increase. From the flat detected phase we can assume that both μ_a and $\mu_s{}'$ have changed

in the same direction, and the phase increase caused by one of them has compensated the effect of the other. Since the AC amplitude decreases during cardiac cycle, we can predict μ_a increases and therefore, $\mu_s{}'$ also increases. This was confirmed by the fitted results shown in Figure 6.7. As expected both μ_a and $\mu_s{}'$ have pulsatile behavior during each cardiac cycle, but the changes in μ_a is up to one order of magnitude bigger than $\mu_s{}'$. These changes also disappear during cuff.

Table 6.2 demonstrates that different wavelengths have different amplitude in the pulsation and the changes are wavelength-dependent. It implies a physiological origin for the pulsation. we translate the change in μ_a in different wavelengths to physiological parameters (hemoglobin concentration and oxygen saturation). In Figure 6.8, we observe that both hemoglobin concentration and oxygen saturation show pulsatile behavior during a cardiac cycle. As expected these pulsations disappeared by applying the cuff occlusion. The pulsation of the THC suggests that although the patella is a rigid bone, the vasculature in this bone can dilate and the THC can increase.

This result is in contradiction with the assumption of previous works [121, 266, 267] where they have assumed that the THC in the bone is constant and the pulsation in the bone is an indicator of the changes in blood flow. This hypothesis was further evaluated, by applying laser-Doppler flowmetry (LDF) to measure changes in RBC count and velocity in rigid bones during a cardiac cycle [254]. It has been shown that the RBC concentration is constant and this study has not detected any physiological origin for pulsations but blood velocity.

In another study it has been shown that the physiological parameters (hemoglobin concentration and oxygen saturation) can change in the rigid bone [258], the constant RBC count in latter work [254] has been explained by differentiating fast and slow changes. In slow changes, like response to cuff inflation, that we have observed in this study or in

response to changes in the bed angle, reported by Binzoni et al. [258], the interstitial fluid had some extra time to diffuse away from the bone. In this way, this volume can be replaced by the blood (dilating vessels) and an increase in THC occurs. Due to time constraints, we did not record the recovery from the deflation of the cuff in all subjects. It was, however, recorded in two subjects out of the eight which has revealed a rapid recovery to the baseline upon deflation.

In fast events such as changes during a single cardiac cycle, the pulsation may be too fast for the interstitial fluid to diffuse, and thus the number of RBC count remains constant. However, the absence of an observed physiological change in the number of RBCs during a cardiac cycle in the large-source detector separation (interoptode) LDF measurement [254], can be also caused by the non-sensitivity of LDF to small changes. It is due to the fact that LDF at large interoptode spacing is more sensitive to velocity changes than to the changes in the RBC number. Small changes in μ_a and μ_s' (in our case of 2.5% and 0.5%, respectively) implies an estimated [261, 305] increase in the probability to detect a moving RBC (this parameter is linked to the RBC count) of 2.2×10^{-4}. This increase is probably too small to be detected by the LDF method.

Further studies utilizing other optical techniques, for example using diffuse correlation spectroscopy (DCS) [2, 33, 119], that measures the blood flow in the same type of vasculature could help us to understand the details of this physiology. In fact, PPG-like measurements with DCS were utilized in forearm and wrist muscle [31] in the past to show phase differences between blood flow and blood volume.

We note that in this study the pulsatile behavior of THC is demonstrated but due to the fact that we have measured just a fraction of the cardiac cycle (between 20% and 50%), we cannot observe the whole cycle of physiological change in a complete cardiac cycle. In principle,

the instrument could be adapted to measure the whole cardiac cycle by utilizing a more complex triggering algorithm or by taking data continuously at a higher rate and carrying out a Fourier analysis to filter out the pulsatile component.

The patella bone during the rest and cuff-occlusion: We have characterized the optical and physiological properties of patella in the baseline. The absolute values of the measured absorption and scattering coefficients for three wavelengths (690, 785, and 830 nm) are calculated by averaging over eight subjects. We translate the difference between different wavelengths to physiological properties (hemoglobin concentration and oxygen saturation). The measured oxygen saturation in baseline is 65% which is in the range of healthy human tissue and bones [119, 153, 306]. The measured THC is less than skeletal muscle, $\approx 40\mu M$ [119], and calcaneus bone, $\approx 25\mu M$[153] which may still be in the range of the physiological variations between subjects since both of the earlier studies used a relatively small number of subjects.

We have also studied the physiological changes in response to arterial cuff occlusion and during occlusion. In this bone measurement THC increases during the occlusion. This is in accordance with the increase in Hb and HbO_2 previously observed in human tibia during arterial occlusion [259]. It can be explained as following; since the femoral artery is coming from thigh muscle to the knee, cuff pressure squeezes the underlying muscle and the blood in the femoral artery is pushed to the non-squeezed bones.

Oxygen saturation slightly increases after starting the cuff inflation, and by completing the inflation, it drops gradually. Because of relatively slow inflation, there was a time delay between the venous and arterial occlusion, which causes initial increase of oxygen saturation. This initial increase also caused by squeezed blood of femoral artery entering the knee. After completing the cuff inflation the amount of

oxygen in the tissue is constant and since bone is a live tissue, it consumes part of oxygen in the blood. Therefore we observe a gradual decrease of oxygen saturation. Our result of measurement on occluded bone is in agreement with previous works [259, 262]. Oxygen saturation decreases slowly during cuff inflation. In 5 minutes of occlusion, the oxygen saturation has decreased 11.3%, while in leg muscle in 3 minutes it has decreased 17.1% [119]. Therefore, the data suggests that the consumption of oxygen in bone is slower than muscle which implies a lower metabolism in bone compared to the skeletal muscle. PPG studies also demonstrate the difference between bone signal and other tissue, e.g. in occlusion measurement, there is a significant difference between bone and skin reaction to cuff deflation. While the AC component of the skin returns to baseline value, the bone shows an increase in AC component compared to the baseline [266].

An obvious shortcoming of this study is the limited number of subjects which makes the statistical statements unsubstantial. However, since the method is non-invasive and relatively straightforward to apply, this could be remedied in future studies.

6.5 Conclusion

We have demonstrated that FD-NIRS is a promising technique to study the pulsations and the physiological properties of bones and normal tissue. In the future, therefore, it may be applied to study vascular and skeletal diseases. The optical and the physiological properties of the patella were characterized, and it has been shown that the absorption and scattering coefficients in the bone are not constant during a cardiac cycle. They have "pulsatile changes". The wavelength dependency of the μ_a amplitude was translated to changes in the oxygenated and deoxygenated hemoglobin which leads to pulsation in the total hemoglobin

concentration and the oxygen saturation. We have also studied the patella bone response to cuff occlusion and a lower metabolism of the bone compared to the skeletal muscle was observed.

Chapter 7

Multi-distance DCS to simultaneously estimate the absolute optical properties and the blood flow index

7.1 Introduction

Diffuse correlation spectroscopy (DCS) or diffuse wave spectroscopy (DWS) [2, 24–30, 47, 49, 53, 54, 307], is a relatively new technique to measure blood flow in the microvasculature. It is noninvasive with high-temporal resolution (up to 100 Hz) [308] and relatively large penetration depth (up to several centimeters) [32, 56, 95, 96].

One of the main limitations of DCS is the influence of the assumed optical properties of the medium on the calculated blood flow index (BFI$\sim \alpha D_b$). Although a non-accurate absorption coefficient (μ_a) causes an error in the calculated BFI, failing to estimate the scattering coefficient accurately (μ_s') will lead to dramatic errors in calculating the blood flow [75, 170]. Since μ_a and μ_s' changes in time and location

and error in these parameters introduce error in BFI, DCS is normally applied in tandem with a near infrared spectroscopy (NIRS) techniques (hybrid devices).

In a general classification we can consider two categories in DCS application: small optode distances (eg. small animal's brain or tumors) or large optode distances (eg. human brain, breast, muscle etc.).
DCS measurements with small optode distances: In small (smaller than 20 mm) source detector separations DCS is usually combined multi-distance frequency domain NIRS [35, 71, 77, 141]. Due to proximity of source and detector, the phase shift is small and sometimes it is difficult to detect and in several cases broadband NIRS [37, 43, 134] is used.

Measurement of absolute μ_a and μ_s' in broadband spectroscopy requires relatively complicated analysis and usually the results have consider error. In small optode distances some studies have combined DCS and a continuous wave (CW) NIRS to monitor changes in optical properties [38, 44, 74].

DCS measurements with large optode distances: The large optode DCS ($>$ 20 mm) is of interest in many categories such as cancer studies (e.g, in breast) and mostly in human neurological [309–315].

In a few studies [75, 114, 155–157] DCS has been applied in conjunction with time resolved spectroscopy (TRS). The absolute values of static optical properties of the medium (μ_a and μ_s') are measured with TRS and they are used as inputs in DCS analysis. There are also hybrid devices consist of DCS and multi source-detector separation frequency domain NIRS [35, 41, 45, 71, 77, 83–85, 116, 117, 119, 132, 142, 143, 314]. Several DCS experiments were carried out with hybrid DCS and diffuse optical spectroscopy (DOS) devices but in general it is difficult with these systems to measure the absolute absorption and scattering coefficients.

Previously, it has been proposed that fitting μ_s' or μ_a simultaneously

with BFI was impractical from a single autocorrelation function [316]. Here we present an algorithm that relies on the assumption that the estimated D_b should be *independent* of the source-detector separation in homogeneous or nearly homogeneous media. It enables us to estimate the absolute value of μ_a, μ_s' and BFI simultaneously, hence minimizing the errors in the BFI estimation.

This approach was motivated by *in vivo* measurements on mouse tumors where we combine broadband CW-NIRS with DCS in a single probe [134]. The errors in the accurate estimation of μ_s' with broadband DOS was leading to BFI estimates that showed a systematic dependence on the source-detector separation 7.1. First, the dependency of blood flow on the optode distances was observed. To verify whether the separation dependency has a physiologic cause or analysis error, we have examined different assumptions of μ_s'. The slope of measured blood flow versus separation depended on the assumed μ_s'. This proves that the an analysis artifact is causing the separation dependency of measured BFI.

This observation was then repeated in homogeneous phantoms and in numerical simulations. Figure 7.2 shows how non-accurate μ_s' will lead an error in measured BFI. Similarly figure 7.3 demonstrates the effect of error in μ_a assumption in BFI estimation. The error gets more pronounced in further separations from the source. Only true assumption of optical properties (μ_a and μ_s') will lead to accurate measurement of BFI which does not depend on separation from the source. In this work we will take advantage from the multi-distance DCS (MD-DCS) to fit for static (μ_a and μ_s') as well as dynamic (BFI) properties of tissue simultaneously. The fitted μ_a and μ_s' are the unique values that makes BFI independent from source-detector separation. This multi-distance DCS fitting (MD-DCS) will improve the measurement of BFI.

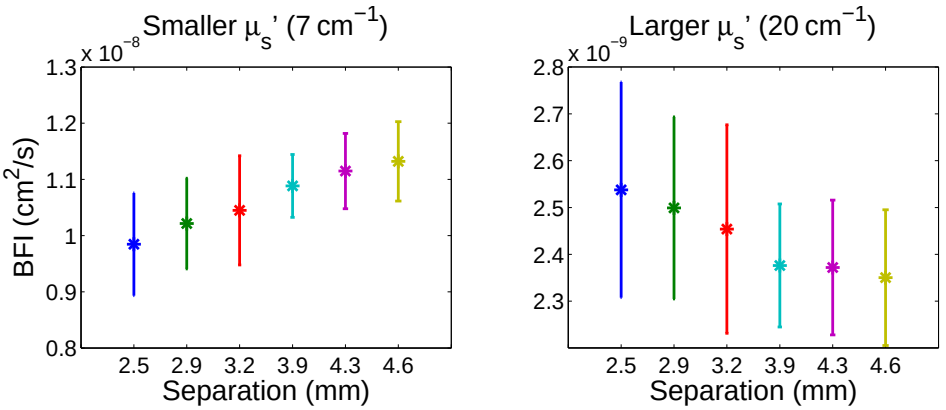

Fig. 7.1 The blood flow measurement on a mouse tumor. The measurement was performed on the mouse muscle for one hour. The plotted values are average and standard deviation over all acquisitions in time. [Left] Underestimation in $\mu_s{}'$ causes the recovered blood flow index increases with distance from the source. (positive slope). [Right] Overestimation in $\mu_s{}'$ causes the recovered blood flow index decreases with distance from the source. (negative slope).

7.2 Theory

Effective attenuation coefficient by DCS CW measurement

To determine the absorption and scattering coefficient of a media one need to modulate the source intensity (frequency domain) or use a short pulse (time domain) to study the changes in phase or pulse to calculate $\mu_s{}'$ and μ_a. In DCS measurement the light source is CW laser usually in one wavelength (785 nm) and in few cases with 2-3 wavelengths. Although we can not separate scattering and absorption coefficient of medium with such a setup, by calibrating the sources and detectors one can obtain the effective attenuation coefficient (μ_{eff}) for each wavelength (equation 7.1).

$$\mu_{eff} = \sqrt{3\mu_a\mu_s{}'} \tag{7.1}$$

μ_{eff} can be obtained by fitting to Green's function solution of dif-

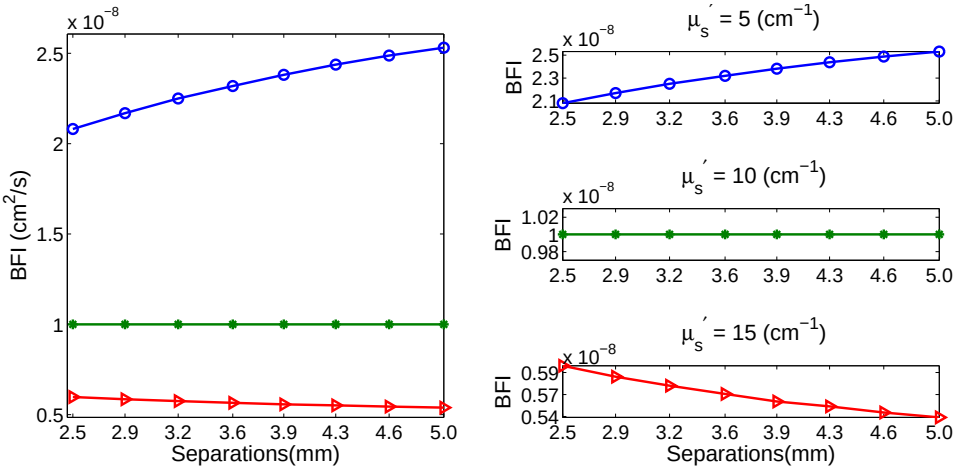

Fig. 7.2 The effect of $\mu_s{}'$ error on BFI calculation (numerical simulations). The simulated BFI $= 1 \times 10^{-8}$ $(\frac{cm^2}{sec})$ and $\mu_s{}' = 10$ (cm^{-1}), $\mu_a = 0.1$ (cm^{-1}). Left: Error in $\mu_s{}'$ causes a separation dependent error in BFI. Right-up: An underestimation in $\mu_s{}'$ leads to BFI overestimation. The error in BFI is getting larger in further separations from the source. Right-center: Only correct $\mu_s{}'$ assumption leads to obtain accurate BFI which is independent of distance from the source. Right-bottom: Overestimation in $\mu_s{}'$ results in underestimation of BFI. The error in calculated BFI gets more pronounced in larger separations from the source.

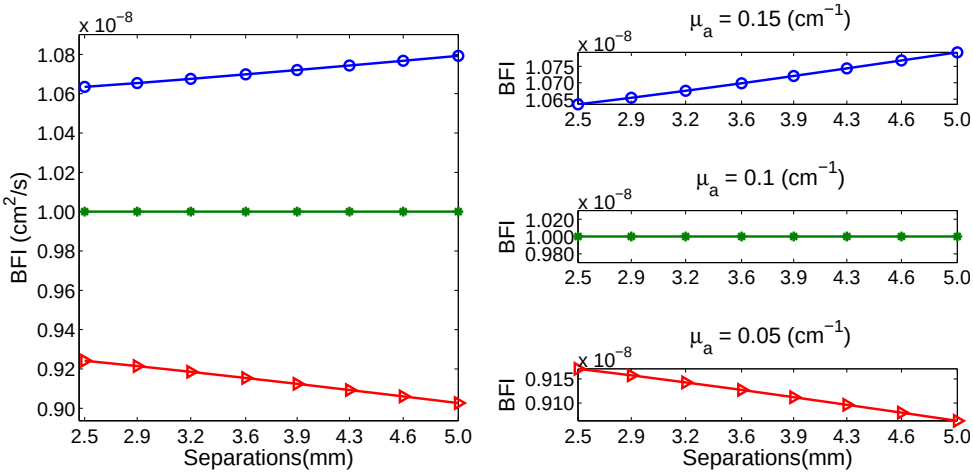

Fig. 7.3 The effect of μ_a error on BFI calculation (numerical simulations). The simulated BFI $= 1 \times 10^{-8}$ $(\frac{cm^2}{sec})$ and $\mu_s{}' = 10$ (cm^{-1}), $\mu_a = 0.1$ (cm^{-1}). Right: Error in μ_a causes a separation dependent error in BFI. Right-up: An overestimation in μ_a leads to BFI overestimation. The error in BFI is getting larger in further separations from the source. Right-center: Only correct μ_a assumption leads to obtain accurate BFI which is independent of distance from the source. Right-bottom: Underestimation in μ_a results in underestimation of BFI. The error in calculated BFI gets more pronounced in larger separations from the source.

fusion (equation 2.6) , or directly by simplified equation: $\ln(I(\rho)\rho^2) = -\mu_{eff}\rho + \ln(I_0)$ (equation 2.7, for more details look at section 2.4) where μ_{eff} is the slope of $\ln(\rho^2 I(\rho))$ versus ρ [2].

The field autocorrelation Green's function for semi-infinite boundary conditions DCS measures the temporal speckle fluctuations of the scattered light, that is sensitive to the motions of scatterers such as red blood cells which in turn could be used to estimate microvascular blood flow [24, 25, 29, 166–168]. The motional dynamics of the medium can be determined by measurement of intensity autocorrelation from which the electric field autocorrelation function (G_1) can be derived. The Green's function solution of the correlation diffusion equation for semi-infinite boundary conditions $G_1(\rho, \tau)$ can be found in section 7.2.

For DCS analysis we converted measured normalized autocorrelation (AC) g_2 to normalized field autocorrelation using Siegert relation (equation 7.2).

$$g_1(\tau) = \sqrt{\frac{g_2(\tau) - 1}{\beta}} \tag{7.2}$$

β is a constant determined primarily by the collection optics of the experiment. In our experiments we use single mode fibers to collect the scattered light. This setup makes $\beta \approx 0.5$. In order to obtain BFI, in a conventional DCS measurement, μ_a and $\mu_s{}'$ should be known through an NIRS measurement (hybrid devices), or typical values of measured tissue. Any error in assumed μ_a and $\mu_s{}'$ would be compensated by underestimation or overestimation of blood flow index.

Figure 7.4 demonstrates the non-uniqueness of autocorrelation curves. It shows media with different optical properties and BFI whose autocorrelation curves are similar. It suggest that error in assumption of μ_a and $\mu_s{}'$ introduces error in fitted BFI [170].

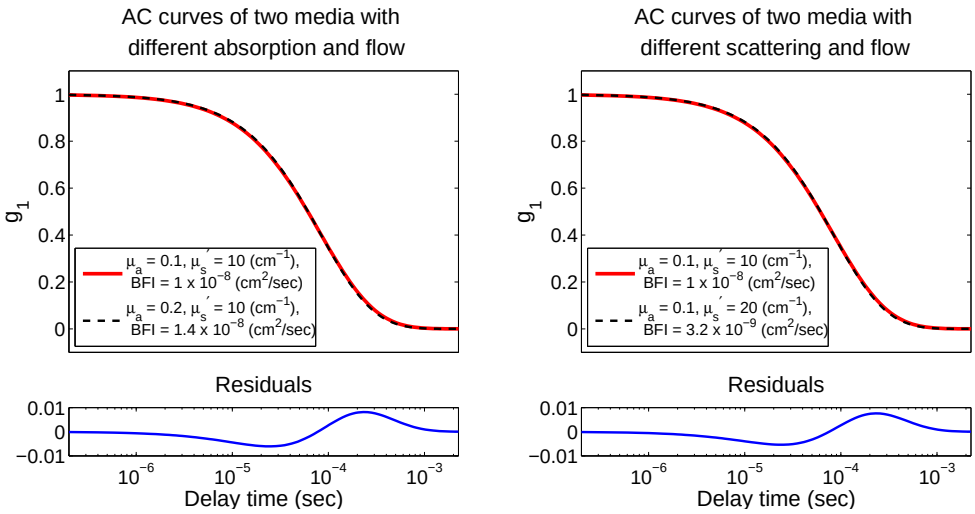

Fig. 7.4 Possibility of similar AC curves in different media. Left: The dashed black curve has higher absorption and BFI than the red curve but the AC curves are similar. Right: The dashed black curve has higher scattering and lower BFI than red curves but the AC curves are similar.

Different behavior of small and large source-detector separations Figure 7.5 shows how the separation-dependency of flow error has different behavior in small and large separations. The BFI in simulated medium is $1\times10^{-8}(\frac{cm^2}{sec})$ with $\mu_s{}' = 10\ (cm^{-1})$ and $\mu_a = 0.1\ (cm^{-1})$. We have fitted for BFI with wrong $\mu_s{}'$ assumption. As expected due to error in $\mu_s{}'$ assumption the fitted value of BFI has an error and the error depends on the separation from the source. In Figure 7.5 the error has direct relation to optode distances up to a certain distance and after that separation the error gets smaller by increasing the optode distance.

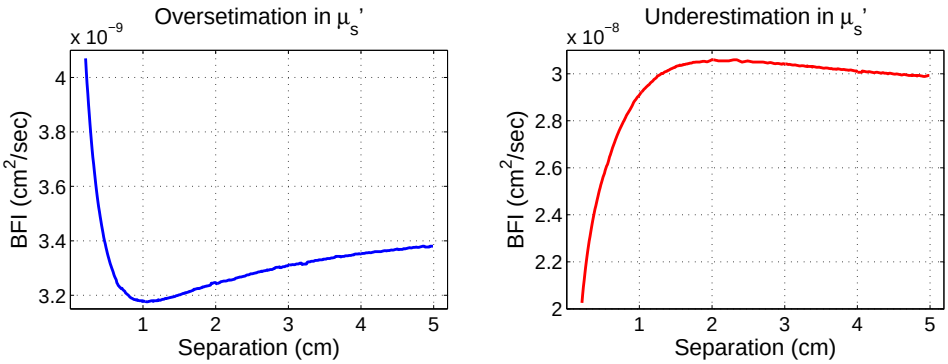

Fig. 7.5 The separation-dependency of flow error has different behavior in small and large separations. The BFI in simulated medium is $1 \times 10^{-8}(\frac{cm^2}{sec})$ with $\mu_s{}' = 10\ (cm^{-1})$ and $\mu_a = 0.1\ (cm^{-1})$. Left: The assumed $\mu_s{}'$ is overestimated ($\mu_s{}' = 20\ cm^{-1}$). The fitted BFI is lower than simulated value. The error in the fitted flow has direct relation to optode distances up to a certain distance and after that separation the error gets smaller by increasing the optode distance. Right: The assumed $\mu_s{}'$ is underestimated ($\mu_s{}' = 5\ cm^{-1}$). The fitted BFI is higher than simulated value. The error in the fitted flow has direct relation to optode distances up to a certain distance and after that separation the error gets smaller by increasing the optode distance.

In figure 7.5 it is shown that in small source-detector separation the separation dependency of BFI error due to wrong assumption of μ_a or $\mu_s{}'$ is more pronounced. Since MD-DCS fitting is based on separation

dependency of BFI, it suggests that MD-DCS to have more challenge in larges source-detector separations.

7.3 Materials and methods

The multi-distance DCS fitting (MD-DCS) As it has been discussed in section 7.2, gathering all information from different separations enables us to decouple the contribution of static (μ_a and μ_s') and dynamic (BFI) properties of the medium. For this purpose, we fit for all desired variables (μ_a, μ_s', BFI) in a single fitting algorithm. Assuming typical values for initial guess of μ_a,μ_s' and BFI the theoretical g_1 is fitted to measured/simulated g_1 over all source-detector separations. In this fitting the function to be minimized (χ^2) is defined as:

$$\chi^2 = \sum_{i=1}^{N_\rho} \sum_{j=1}^{N_\tau} \left(g_1^{theory}(\rho_i, \tau_j, D_b, \mu_s', \mu_a) - g_1^{measured}(\rho_i, \tau_j, D_b, \mu_s', \mu_a)\right)^2, \tag{7.3}$$

where ρ_i is the i^{th} source-detector separation and N_ρ is the number of source-detector separations. τ_j is the the j^{th} delay time and N_τ is the number of delay times. The iterative minimization process has been performed in Matlab by resorting to "fminsearch" function that uses Nelder-Mead method at its core, which is a derivative-free simplex method.

As described in section 7.2, multi-distance DCS measurements provide us with information on μ_{eff} of the medium. We can readily use this information in our fitting to make it more robust and efficient. Knowing μ_{eff}, we can evaluate the μ_a as

$$\mu_a = \frac{{\mu_{eff}}^2}{3\mu_s'}, \tag{7.4}$$

and simplify equation 7.3 to:

$$\chi^2 = \sum_{i=1}^{N_\rho} \sum_{j=1}^{N_\tau} (g_1^{theory}(\rho_i, \tau_j, D_b, {\mu_s}') - g_1^{measured}(\rho_i, \tau_j, D_b, {\mu_s}'))^2. \quad (7.5)$$

Numerical data generation In this study we have simulated 125 media with different 5 different μ_a (from 0.04 to 0.16 with steps of 0.03 cm^{-1}), 5 ${\mu_s}'$ (from 4 to 16 with steps of 3 cm^{-1}) and 5 D_b (from 4×10^{-9} to 16×10^{-9} with steps of 3×10^{-9} $\frac{cm^2}{sec}$). In order to increase signal to noise ratio in DCS measurements, it is common to put multiple fibers for each separation to increase the signal to noise level ratio [157, 313]. In this study we have assumed there are 16 acquisitions in each optode distance. We have used three sets of optode separations:

1. Small separations: the same optode distances as our murine probe (chapter 3) is used for small separations [134]. In this probe there are 8 non-uniformly separations from 2.5 to 5 mm (2.5, 2.9, 3.2, 3.6, 3.9, 4.3, 4.6, 5.0 mm).

2. intermediate separations: 6 optode distances from 10 mm to 20 mm with intervals of 2 mm.

3. Large separations: 8 optode distances from 20 mm to 34 mm with intervals of 2 mm.

The averaging time of one minute was kept constant for all measurements. The maximum photon count rate (1000 kHz) is assigned to smallest source-detector separations. This is the upper limit of avalanche photodiodes (APDs) which are used in experiment setup.The photon count rate decreases exponentially. The photon count rate for each optode is calculated from green function solution for photon fluence rate in semi-infinite boundary conditions [2]. In the simulated data, the minimum count rate is $\approx 15kHz$. We have simulated DCS measurements

using forward model (section 7.2). After producing the theoretical autocorrelation curve for each media and each experimental setup, we have added noise to the simulated autocorrelation curve using DCS noise model which is described in section 2.6.

Comparison to other methods: We have compared the results of MD-DCS fitting to other possible DCS analysis to show how MD-DCS will modify the quality of BFI measurements, while it is providing us with optical properties information (μ_a and $\mu_s{}'$) without any hybrid NIRS device. MD-DCS is compared with other methods.

1. Exact μ_a and $\mu_s{}'$ value: it was assumed that the exact value for absorption and scattering coefficients are known.

2. Exact μ_a and 30% error in $\mu_s{}'$: it was assumed that the exact value for absorption coefficient is known and scattering is over/under -estimated by 30%.

3. Exact μ_a and 2 (cm^{-1}) error in $\mu_s{}'$: it was assumed that the exact value for absorption coefficient is known and there is 2 (cm^{-1}) over/under -estimation of $\mu_s{}'$.

4. Deploying MD-DCS fitting assuming μ_{eff} of the medium (MD-DCS given μ_{eff}).

5. Deploying MD-DCS fitting without any information about optical properties of medium (MD-DCS without μ_{eff})

Error of fitted BFI for different absorption and scattering coefficients: To compare the error in fitted BFI by MD-DCS to other methods we need to define the error. For each of the simulated BFI there are 5 $\mu_s{}'$ and 5 μ_a. For each BFI, the error is root mean square of

the relative difference between fitted and expected values of BFI,

$$\varepsilon_{BFI} = \sqrt{\frac{1}{N}\sum_{\mu_s'}\sum_{\mu_a}\left(\frac{BFI_{fitted} - BFI_{expected}}{BFI_{expected}}\right)^2} \tag{7.6}$$

where N is the total number of different sets of μ_a μ_s' for a given BFI (in this case: $5 \times 5 = 25$).

Phantom measurements: We have performed the DCS measurements on 7 liquid phantoms which consist of water and Lipofundin MCT 20%. The probe used in these tests is the same probe as we use for mouse tumor studies [134]. In this probe there are 8 non-uniformly separations from 2.5 to 5 mm (0.25, 0.29, 0.32, 0.36, 0.39, 0.43, 0.46, 0.5 mm). I started with 160 ml of water and for each step 5 ml of lipofundinMCT 20% was added, except the last step which was 10 ml. The DCS device and probe are described in chapter 3.

In-vivo measurements: We have monitored the blood flow changes of the mouse tumors induced by antiangiogenic therapy. The details of mouse strain, tumor line and therapy is explained in section 4.2.2. The device employed in this study is described in chapter 3. In summary, we have combined broadband NIRS and DCS in a single probe. Both NIRS and DCS have 6 source-detector separations (from 2.5 to 5 mm). The mouse was measured just before the start of therapy (day-zero). The mouse received the therapy twice per week and before each drug injection we have performed optical measurements on the tumor. In every measurement, in order to have better statics of the optical properties of tumor we have re-positioned the probe 10 times and each relocating include 11 acquisitions.

In our conventional analysis, DCS takes the measured μ_a and μ_s' values from broadband NIRS device as known optical properties. Here

we have re-analyzed the DCS data by MD-DCS fitting to compare the results (μ_a, μ_s' and BFI) with the results of hybrid device (NIRS and DCS). The measured μ_{eff} values by NIRS is given to the MD-DCS fitting in each location. We averaged the intensity autocorrelation curves of all acquisitions, then for each location MD-DCS fitting provide us with μ_a, μ_s', and BFI of the location. We have averaged the fitted μ_a and μ_s' from MD-DCS method to have an average value for tumor optical properties. Afterwards given the estimated optical properties of the medium we calculate the BFI of each location. We have investigated the equality of fitted BFI of MD-DCS and traditional DCS (taking fitted μ_a and μ_s' as the input of DCS fitting) by student t-test. The "p-values" less than 0.05 were considered statically significant to reject the null hypothesis.

7.4 Results and discussions

7.4.1 Numerical simulations

In this section, the results of MD-DCS fitting on simulated data, phantom, and *in-vivo* measurements is reported.

Noise-free simulations: In the simulated data, regardless of source-detector separation, degree of absorption, scattering, or BFI, The MD-DCS fitting always works accurately and the fitted μ_a, μ_s' and BFI are exact. In the figure 7.6 the error in fitted BFI by MD-DCS and other methods is presented. The error is calculated using equation 7.6. The source-detector separation is large (2-3.4 cm) where MD-DCS fit is challenging. It can be seen that error in fitted BFI in both conditions, without and with μ_{eff} (red triangles), is 0%. This accuracy is possible only when we know the exact values of μ_a and μ_s' (black triangles). Overestimation in μ_s' induces more than 30% error in fitted

BFI, while μ_s' underestimation causes more dramatic BFI error. This

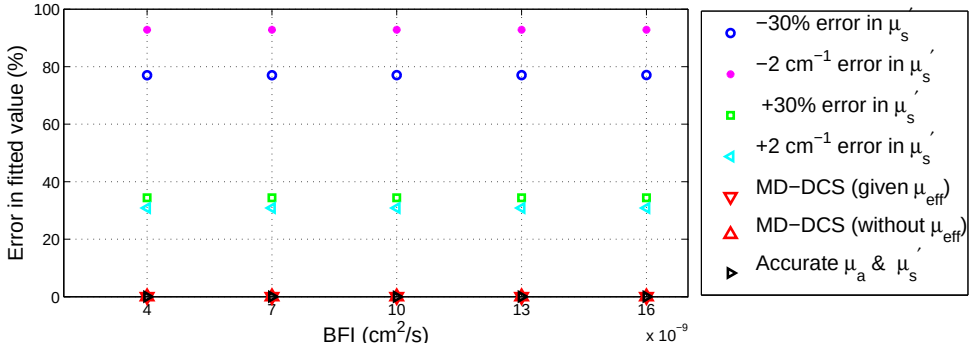

Fig. 7.6 The error in fitted BFI by MD-DCS comparing to other methods in noise-free data. The source-detector separation is large (2-3.4 cm). It can be seen that error in fitted BFI in both conditions, with and without μ_{eff} (red triangles), is 0%. This accuracy is possible only when the exact values of μ_a and μ_s' are known.

results demonstrates MD-DCS fitting in principle can decouple μ_a, μ_s' and BFI in noise-free data. To evaluate its efficiency in more realistic conditions we have added noise to the data and in each separation type the feasibility of MD-DCS fitting in the following sections is studied.

Noise-added simulations of small optode distances: To evaluate the efficiency of MD-DCS fitting the noise model is added to the simulated data (described in section 2.6). Figure 7.7 shows the values of fitted μ_s', μ_a, and BFI by MD-DCS versus the expected (simulated) values in small source-detector separations (2.5-5 mm). Each color represents one μ_s' (red: $\mu_s' = 4$, green: $\mu_s' = 7$, blue: $\mu_s' = 10$, cyan: $\mu_s' = 13$, black: $\mu_s' = 16$) and each μ_a is represents by a marker (star: $\mu_a = 0.04$, circle: $\mu_a = 0.07$, square: $\mu_a = 0.10$, cross: $\mu_a = 0.13$, triangle: $\mu_a = 0.16$). We have used dodging (moving the points slightly across the x-axis) for better representation of BFI values (BFI increases from left to right). In figure 7.7-left the fitted μ_s' by MD-DCS is presented. We

can see for all μ_as and BFIs the fitted $\mu_s{}'$ is in good agreement with expected values. In figure 7.7-middle the fitted μ_a by MD-DCS is present. For all $\mu_s{}'$s and BFIs, fitted μ_a is in good agreement with expected values. The right side of figure 7.7 demonstrates that the fitted BFI is in agreement compared with the expected values.

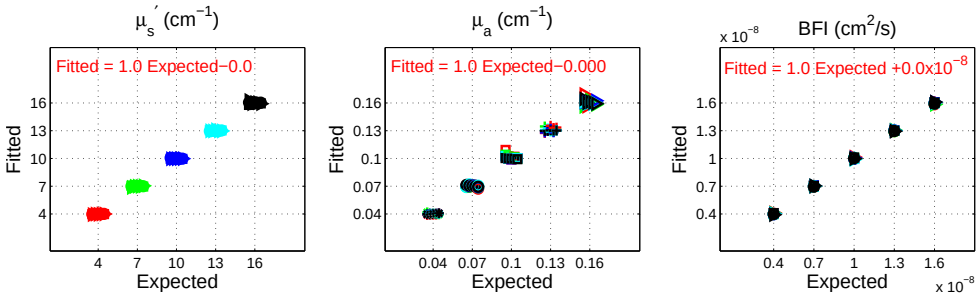

Fig. 7.7 The values of fitted $\mu_s{}'$, μ_a, and BFI by MD-DCS versus the expected (simulated) values in small source-detector separations (2.5-5 mm). The linear fitting equation of fitted values versus expected ones for each parameter is displayed. The fitted line for all parameters have slope of one and zero intercept which indicate the complete agreement of fitted and expected values. Each color represents one $\mu_s{}'$ (red: $\mu_s{}' = 4$, green: $\mu_s{}' = 7$, blue: $\mu_s{}' = 10$, cyan: $\mu_s{}' = 13$, black: $\mu_s{}' = 16$) and each μ_a is represents by a marker (star: $\mu_a = 0.04$, circle: $\mu_a = 0.07$, square: $\mu_a = 0.10$, cross: $\mu_a = 0.13$, triangle: $\mu_a = 0.16$). Dodging is used (moving the points slightly across the x-axis) for better representation of BFI values (For each $\mu_s{}'$ or μ_a, BFI increases from left to right). [Left] The fitted $\mu_s{}'$ by MD-DCS is present. For all μ_as and BFIs the fitted $\mu_s{}'$ is in good agreement with expected values. [Middle] The fitted μ_a by MD-DCS for all $\mu_s{}'$s and BFIs is in good agreement with expected values. [Right] The fitted BFI is in agreement compared with the expected values.

In the figure 7.8 the error in fitted BFI by MD-DCS comparing to the other methods in noise-added simulated data is presented. The error is calculated using equation 7.6. The source-detector separation is small (2.5-5 mm). The error in fitted BFI in both conditions, with and without μ_{eff} (red triangles), is 0%. This accuracy is possible only

when the exact values of μ_a and μ_s' are known. Overestimation in μ_s' induces ∼30% error in the fitted BFI, while μ_s' underestimation causes more dramatic BFI error.

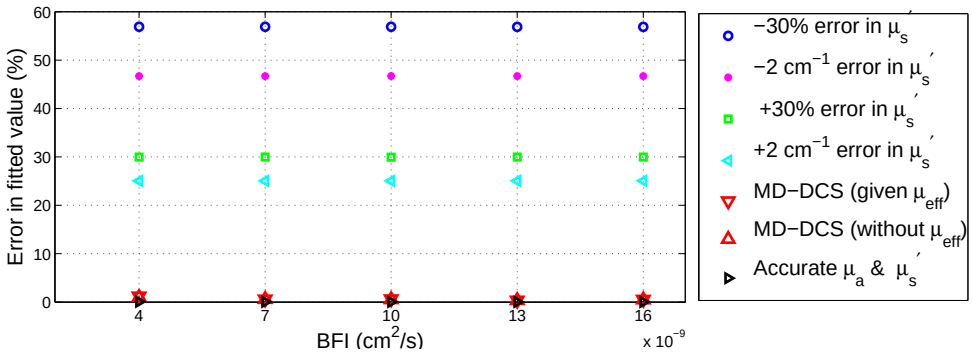

Fig. 7.8 The error in fitted BFI by MD-DCS comparing to the other methods in noise-added simulated data. The source-detector separation is small (2.5-5 mm). The error in fitted BFI in both conditions, with and without μ_{eff} (red triangles) is 0%. Overestimation in μ_s' induces ∼30% error in the fitted BFI, while μ_s' underestimation causes more dramatic BFI error.

Noise-added simulations of intermediate optode distances: As figure 7.5 suggests the MD-DCS fitting may be more challenging in larger source-detector separations. To test the efficiency of method in larger optode distances (in noise-added data), we have applied the method on intermediate separations (10-20 mm). The results are presented in figure 7.9. As in previous plots, each color represents one μ_s' (red: $\mu_s' = 4$, green: $\mu_s' = 7$, blue: $\mu_s' = 10$, cyan: $\mu_s' = 13$, black: $\mu_s' = 16$) and each μ_a is represents by a marker (star: $\mu_a = 0.04$, circle: $\mu_a = 0.07$, square: $\mu_a = 0.10$, cross: $\mu_a = 0.13$, triangle: $\mu_a = 0.16$). We have used dodging (moving the points slightly across the x-axis) for better representation of BFI values (BFI increases from left to right). In figure 7.9-left the fitted μ_s' by MD-DCS is presented. We can see

for all μ_as and BFIs the fitted μ_s' is in good agreement with expected values. In figure 7.9-middle the fitted μ_a by MD-DCS is present. For all μ_s's and BFIs, fitted μ_a is in good agreement with expected values. The right side of figure 7.9 demonstrates that the fitted BFI is in agreement compared with the expected values.

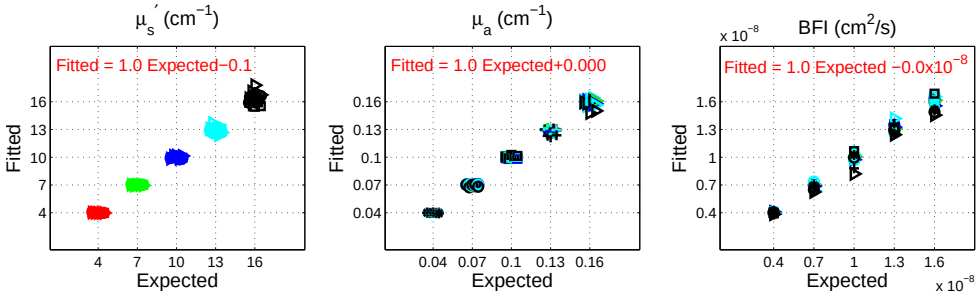

Fig. 7.9 The values of fitted μ_s', μ_a, and BFI by MD-DCS versus the expected (simulated) values in intermediate source-detector separations (10-20 mm). The linear fitting equation of fitted values versus expected ones for each parameter is displayed. Each color represents one μ_s' (red: $\mu_s' = 4$, green: $\mu_s' = 7$, blue: $\mu_s' = 10$, cyan: $\mu_s' = 13$, black: $\mu_s' = 16$) and each μ_a is represents by a marker (star: $\mu_a = 0.04$, circle: $\mu_a = 0.07$, square: $\mu_a = 0.10$, cross: $\mu_a = 0.13$, triangle: $\mu_a = 0.16$). Dodging is used (moving the points slightly across the x-axis) for better representation of BFI values (For each μ_s' or μ_a, BFI increases from left to right). [Left] The fitted μ_s' by MD-DCS is present. The fitted line of fitted μ_s' versus expected values have slope of one and intercept of -0.1 which indicate the a fair agreement between fitted and expected μ_s'. [Middle]. The fitted line of fitted μ_a versus expected values have slope of one and zero intercept which indicate the complete agreement of fitted and expected absorption coefficient. [Right] The fitted BFI is in agreement compared with the expected values (slope = 1, intercept = 0).

In the figure 7.10 the error in fitted BFI by MD-DCS comparing to the other methods in noise-added simulated data is presented. The error is calculated using equation 7.6. The source-detector separation is

small (2.5-5 mm). The error in fitted BFI in both conditions, with and without μ_{eff} (red triangles), is less than 5%. This accuracy is possible only when the exact values of μ_a and μ_s' are known. Overestimation in μ_s' induces ~30% error in the fitted BFI, while μ_s' underestimation causes more dramatic BFI error. The results of MD-DCS fitting in

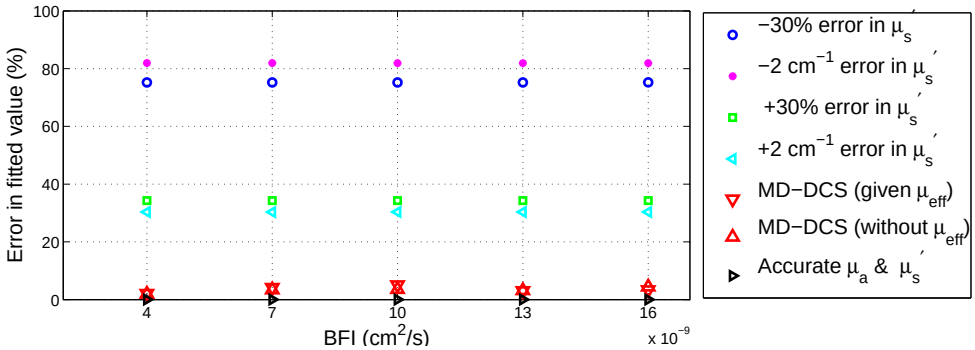

Fig. 7.10 The error in fitted BFI by MD-DCS comparing to the other methods in noise-added simulated data. The source-detector separation is intermediate (10-20 mm). The error in fitted BFI in both conditions, with and without μ_{eff} (red triangles) is less than 5%. Overestimation in μ_s' induces more than 30% error in the fitted BFI, while μ_s' underestimation causes more dramatic BFI error.

intermediate source-detector separations suggest that the fitting is rigid enough in this regime.

Noise-added simulations of large optode distances: In order to evaluate the limits of MD-DCS fitting we have enlarged the simulated optode distances to 20-34 mm. This is where the fitting loses its accuracy specially in large μ_a, μ_s', or BFI. Figure 7.11 shows the values of fitted μ_s', μ_a, and BFI by MD-DCS versus the expected (simulated) values in large source-detector separations. In Figure 7.11-left the fitted μ_s' by MD-DCS is present. The fitted line of fitted μ_s' versus expected values have slope of 1.2 and intercept of -1.2 which indicates that in

large optode distances the algorithm starts to fail specially in higher μ_s' values. In the middle plot, the fitted line of fitted μ_a versus expected values have slope of 0.8 and zero intercept and in the right plot we can see the fitted BFI is not in a good agreement compared with the expected values (slope = 0.9, intercept = 0).

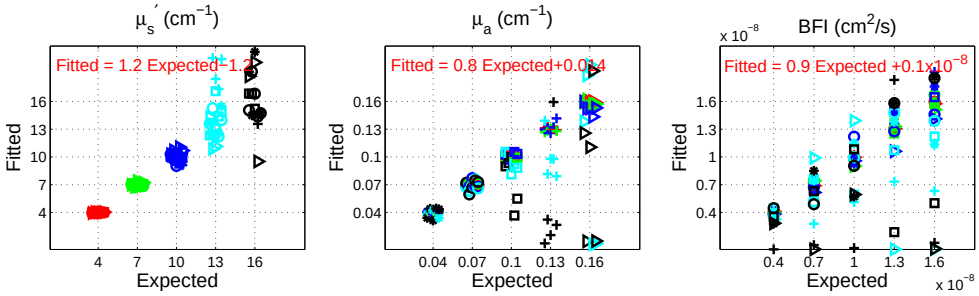

Fig. 7.11 The values of fitted μ_s', μ_a, and BFI by MD-DCS versus the expected (simulated) values in large source-detector separations (20-34 mm). The linear fitting equation of fitted values versus expected ones for each parameter is displayed. Each color represents one μ_s' (red: μ_s' = 4, green: μ_s' = 7, blue: μ_s' = 10, cyan: μ_s' = 13, black: μ_s' = 16) and each μ_a is represents by a marker (star: μ_a = 0.04, circle: μ_a = 0.07, square: μ_a = 0.10, cross: μ_a = 0.13, triangle: μ_a = 0.16). Dodging is used (moving the points slightly across the x-axis) for better representation of BFI values (For each μ_s' or μ_a, BFI increases from left to right). [Left] The fitted μ_s' by MD-DCS is present. The fitted line of fitted μ_s' versus expected values have slope of 1.2 and intercept of -1.2 which indicates that in large optode distances the algorithm starts to fail specially in higher μ_s' values. [Middle]. The fitted line of fitted μ_a versus expected values have slope of 0.8 and zero intercept which indicate that in large optode distances the algorithm starts to fail specially in higher μ_a values. [Right] The fitted BFI is in agreement compared with the expected values (slope = 0.9, intercept = 0).

The error in fitted BFI for every μ_a and μ_s' is determined by equation 7.6 and is presented in the figure 7.12 The error in fitted BFI in both conditions, with and without μ_{eff} (red triangles) is hight (between

20-45%) which is similar to induced error by 30% overestimated of μ_s'. It shows the MD-DCS fitting starts to lose its accurately in large optode distances specially in higher values of BFI.

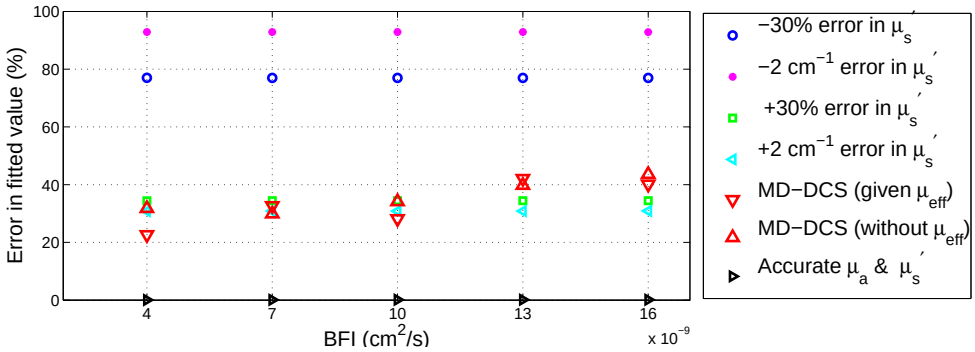

Fig. 7.12 The error in fitted BFI by MD-DCS comparing to the other methods in noise-added simulated data. The source-detector separation is large (20-34 mm). The error in fitted BFI in both conditions, with and without μ_{eff} (red triangles) is hight (between 20-45%) which is similar to induced error by 30% overestimated of μ_s'. It shows the MD-DCS fitting fails to fit accurately in large optode distances specially in higher values of BFI.

7.4.2 Results MD-DCS fitting on liquid phantom measurements

Figure 7.13 shows the results of MD-DCS fitting on liquid phantom measurements. As described in section 7.3 we have performed Lipofundin titration. Figure 7.13-left shows the measured (fitted by MD-DCS fitting) μ_s' versus expected value and their increase in each step of titration. The measured values have good agreement with expected values. The linear fitting equation of fitted values versus expected ones for each parameterμ_s' is presented (slope = 0.9, intercept = 0.4). By assuming the absorption coefficient for Lipofundin and water the absorption of all

phantoms are expected to be the same. Figure 7.13-middle shows as expected the fitted absorption coefficient of all phantoms are the same and in the range of expected μ_a for water of ($\mu_a^{785\ nm} = 0.02 - 0.03\ cm^{-1}$). Since the changes in viscosity due to Lipofundin titration is negligible, it is expected for BFI to not change by Lipofundin titration. Figure 7.13-right shows the measured (fitted by MD-DCS fitting) BFI is constant over all phantoms.

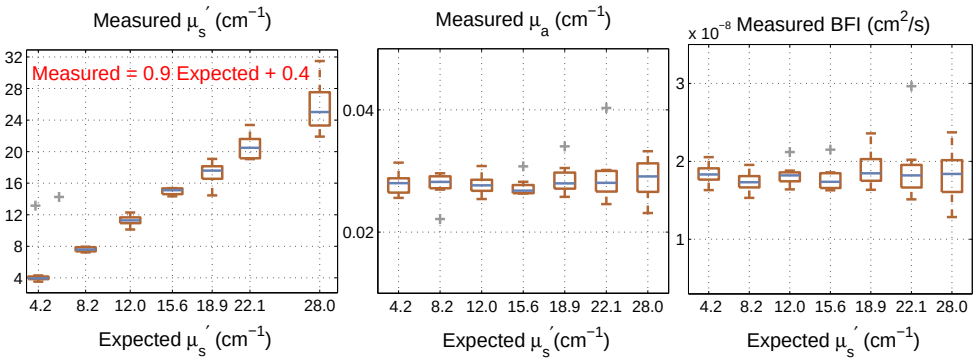

Fig. 7.13 The measured μ_a, μ_s', and BFI by MD-DCS versus expected values in liquid phantom measurement. [Left] The measured (fitted by MD-DCS fitting) μ_s' versus expected value and their increase in each step of titration. The linear fitting equation of fitted values versus expected ones for each parameter μ_s' is presented (slope = 0.9, intercept = 0.4). [Middle] The measured (fitted by MD-DCS fitting) absorption coefficient of all phantoms are the same and in the range of expected μ_a for water of ($\mu_a^{785\ nm} = 0.02 - 0.03\ cm^{-1}$). [Left] The measured (fitted by MD-DCS fitting) BFI is constant over all phantoms.

7.4.3 Results of MD-DCS fitting on *in-vivo* studies

To validate the MD-DCS technique on more realistic scenarios where we should deal with heterogeneity of the medium, we have applied the method on a mouse tumor which is a highly heterogeneous tissue. To

validate our values we have compared the fitted μ_a, μ_s', and BFI from MD-DCS to the fitted values from broadband NIRS device. The details of measurements and fittings are described in section 7.3. The results of fitting values with both methods (MD-DCS, NIRS) for all three parameters over 24 days are presented in figure 7.14. Although the fitted μ_a and μ_s' from NIRS and MD-DB deviates slightly, the fitted BFI from both fitting agrees with each other. In each day the values of BFI from MD-DCS and traditional DCS are compared and the days that the equality of mean values are statistically significant are marked by blue stars. In all days except day 8,20 and 24 the measured BFI from both methods are equal.

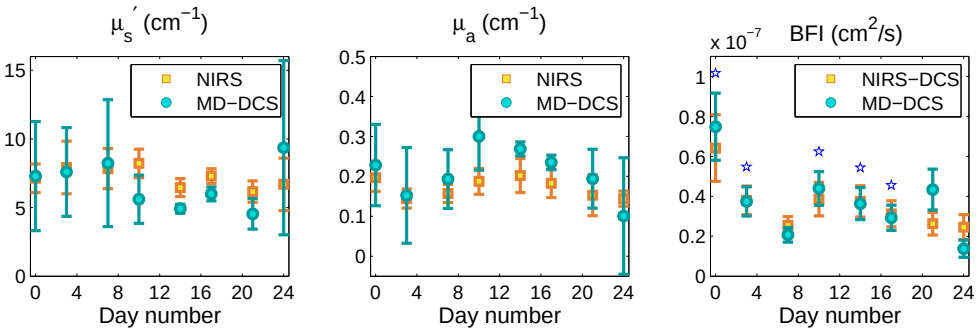

Fig. 7.14 The fitted values from both methods (MD-DCS, NIRS) for μ_s', μ_a, and BFI over 24 days in a mouse tumor. [Left] The fitted μ_s' from NIRS and MD-DCS. [Middle] The fitted μ_a from NIRS and MD-DCS. [Right] The fitted BFI from both fitting agrees with each other. In each day the values of BFI from MD-DCS and traditional DCS are compared and the days that the equality of mean values are statistically significant are marked by blue stars. In all days except day 8,20 and 24 the measured BFI from both methods are equal.

7.5 Conclusion

For the first time we have investigated the possibility of simultaneous extracting of absorption coefficient (μ_a), scattering coefficient (μ_s'), and blood flow index (BFI) of the tissue using multi-distance diffuse correlation spectroscopy (MD-DCS). We have validated MD-DCS by numerical simulations with realistic noise model. It is demonstrated that the fitting is more robust in smaller source-detector separations (from 2 mm to 20 mm). In larger source-detector separations the error in fitted parameters increases. In addition to the numerical simulations, MD-DCS is validated through measurement of tissue simulating phantoms. To validate the MD-DCS fitting in more realistic scenarios where the medium is heterogeneous, we have applied the method on a mouse tumor which is a highly heterogeneous tissue. The results suggest that multi-distance DCS can be an alternative to traditional hybrid devices (NIRS + DCS) specially in small source-detector separations where obtaining optical properties of the medium with common NIRS techniques are challenging.

Chapter 8

Conclusion

In this work, I have described the development of hybrid diffuse optical devices for noninvasive hemodynamics monitoring to be used in human and animal studies at hospitals and animal facilities.

The hybrid device is a combination of near infrared spectroscopy (NIRS) for oxygenation and diffuse correlation spectroscopy for blood flow measurements. Depending on the application and the limitations of measurement different types of NIRS technique have been deployed. The applied NIRS technique in this work are continuous wave (CW), frequency domain (FD), and time resolved spectroscopy (TRS). The advantages and limitations of each technique is described in chapter 2.

Continuous wave which is the simplest NIRS technique was deployed for measurement of murine tumors in conjunction with diffuse correlation spectroscopy in a hand-held, self-calibrated probe. The device is designed for hybrid, broadband, multi-spectral, multi-distance NIRS/DCS measurement and is validated by phantom and *in-vivo* studies. The device specification, probe design and validation results are presented in chapter 3.

The designed, constructed, and validated device has been moved to animal facility for hemodynamics monitoring in murine tumors during

antiangiogenic therapy. In this study early hemodynamics changes correlate with the outcome of therapy. These results suggest that diffuse optics have potential to play an important role to understand the mechanism of tumor defense against the antiangiogenic therapies. continuing the study with larger number of tumors may lead us to develop optical parameters to predict the success of therapy which results in personalized treatment procedure for each subject. The mice models, therapy procedure, measurement, and the measured parameters are explained in chapter 4.

In this work I have introduced diffuse optics as an potential tool to study hematological malignancies in human. The hybrid device used in this study is a combination of TRS and DCS. Since hematological malignancies affect the red bone marrow, we have characterized the manubrium as a site rich of red bone marrow in the adults. For the first time, we have characterized the optical and hemodynamics properties of the manubrium in thirty-two healthy subjects. This study is the first step in the path of applying optics for the studies on bone marrow cancer. The distribution of optical and physiological parameters in the healthy bone marrow is demonstrated in chapter 5. Measuring the same parameters in the patients with hematological malignancies will illustrate the difference between distribution of measured parameters on the healthy and malignant marrow. It can be applied for screening purposes to detect subjects with high risk of hematological malignancies. We can also monitor to changes in optical and physiological parameters induced by antiangiogenic therapies to predict the effect of treatment and personalize the therapy.

My interest in hematological malignancies and bone marrow led me to learn more about the physiology of compact bone. Lack of optical studies on bone motivated me to investigate the feasibility of optics to answer bone physiological questions. We have demonstrated that FD-

NIRS is a promising technique to study the pulsations and the physiological properties of bones and normal tissue. In the future, therefore, it may be applied to study vascular and skeletal diseases. In chapter 6, the optical and the physiological properties of the patella were characterized, and it has been shown that the absorption and scattering coefficients in the bone are not constant during a cardiac cycle. They have "pulsatile changes". The wavelength dependency of the absorption coefficient was translated to changes in the oxygenated and deoxygenated hemoglobin which leads to pulsation in the total hemoglobin concentration and the oxygen saturation. We have also studied the patella bone response to cuff occlusion and a lower metabolism of the bone compared to the skeletal muscle was observed.

Several years of experiments using hybrid devices raised a question in my mind: Can we obtained absolute value of absorption and scattering coefficients from autocorrelation curves of DCS device? To answer this question for the first time we have investigated the possibility of simultaneous extracting of absorption coefficient, scattering coefficient, and blood flow index of the tissue using multi-distance diffuse correlation spectroscopy (MD-DCS). We have validated MD-DCS by numerical simulations with realistic noise model. It is demonstrated that the fitting is more robust in smaller source-detector separations (from 2 mm to 20 mm). In larger source-detector separations the error in fitted parameters increases. In addition to the numerical simulations, MD-DCS is validated through measurement of tissue simulating phantoms. To validate the MD-DCS fitting in more realistic scenarios where the medium is heterogeneous, we have applied the method on a mouse tumor which is a highly heterogeneous tissue. The results suggest that multi-distance DCS can be an alternative to traditional hybrid devices (NIRS + DCS) specially in small source-detector separations where obtaining optical properties of the medium with common NIRS techniques

are challenging.

A major contribution of this manuscript was applying diffuse optics to answer new biological questions in experimental biology. I have introduced diffuse optics to hematological malignancies studies which also demonstrated the feasibility of applying optics in bone and bone marrow. Finally, I have demonstrated the possibility of measurement of tissue static (absolute value of blood volume and oxygenation) and dynamic (blood flow) using DCS autocorrelation curves. This can be an alternative to hybrid DCS-NIRS devices.

References

[1] A. Yodh and B. Chance. Spectroscopy and imaging with diffusing light. *Physics Today*, 48:34–40, 1995.

[2] T. Durduran, R. Choe, W. B. Baker, and A. G. Yodh. Diffuse optics for tissue monitoring and tomography. *Reports on Progress in Physics*, 73(7):076701, 2010.

[3] F. F. Jo Bsis-Vandervliet. Discovery of the near-infrared window into the body and the early development of near-infrared spectroscopy. *Journal of biomedical optics*, 4(4):392–6, 1999.

[4] F. F. Jöbsis and Others. Noninvasive, infrared monitoring of cerebral and myocardial oxygen sufficiency and circulatory parameters. *Science (New York, NY)*, 198(4323):1264, 1977.

[5] H. M. Heise. Applications of near-infrared spectroscopy in medical sciences. *Wiley-VCH Verlag GmbH*, 2002.

[6] H. Owen-Reece, M. Smith, C. E. Elwell, J. C. Goldstone, and Others. Near infrared spectroscopy. *British journal of anaesthesia*, 82:418–426, 1999.

[7] V. R. Kondepati, H. M. Heise, and J. Backhaus. Recent applications of near-infrared spectroscopy in cancer diagnosis and therapy. *Analytical and bioanalytical chemistry*, 390(1):125–39, 2008.

[8] M. F. Stiefel, A. Spiotta, V. H. Gracias, A. M. Garuffe, O. Guillamondegui, E. Maloney-Wilensky, S. Bloom, M. S. Grady, and P. D. LeRoux. Reduced mortality rate in patients with severe traumatic brain injury treated with brain tissue oxygen monitoring. *Journal of neurosurgery*, 103(5):805–11, 2005.

[9] P. K. Narotam, J. F. Morrison, and N. Nathoo. Brain tissue oxygen monitoring in traumatic brain injury and major trauma: outcome analysis of a brain tissue oxygen-directed therapy. *Journal of neurosurgery*, 111(4):672–82, 2009.

[10] J. Nortje and a. K. Gupta. The role of tissue oxygen monitoring in patients with acute brain injury. *British journal of anaesthesia*, 97(1):95–106, 2006.

[11] E. Maloney-Wilensky, V. Gracias, A. Itkin, K. Hoffman, S. Bloom, W. Yang, S. Christian, and P. D. LeRoux. Brain tissue oxygen and outcome after severe traumatic brain injury: a systematic review. *Critical care medicine*, 37(6):2057–63, 2009.

[12] P. Vaupel, D. K. Kelleher, and M. Höckel. Oxygen status of malignant tumors: pathogenesis of hypoxia and significance for tumor therapy. *Seminars in oncology*, 28(2 Suppl 8):29–35, 2001.

[13] P. Vaupel. The role of hypoxia-induced factors in tumor progression. *The oncologist*, 9 Suppl 5:10–7, 2004.

[14] M. Höckel and P. Vaupel. Tumor hypoxia: definitions and current clinical, biologic, and molecular aspects. *Journal of the National Cancer Institute*, 93(4):266–276, 2001.

[15] H. B. Stone, J. M. Brown, T. L. Phillips, and R. M. Sutherland. Oxygen in human tumors: correlations between methods of measurement and response to therapy. Summary of a workshop held November 19-20, 1992, at the National Cancer Institute, Bethesda, Maryland. *Radiation research*, 136(3):422–34, 1993.

[16] J. E. Moulder and S. Rockwell. Tumor hypoxia: its impact on cancer therapy. *Cancer and Metastasis Reviews*, 5(4):313–341, 1987.

[17] L. B. Harrison. Impact of Tumor Hypoxia and Anemia on Radiation Therapy Outcomes. *The Oncologist*, 7(6):492–508, 2002.

[18] S. Merritt, G. Gulsen, G. Chiou, Y. Chu, C. Deng, a. E. Cerussi, a. J. Durkin, B. J. Tromberg, and O. Nalcioglu. Comparison of water and lipid content measurements using diffuse optical spectroscopy and MRI in emulsion phantoms. *Technology in cancer research & treatment*, 2(6):563–9, 2003.

[19] D. J. Hawrysz and E. M. Sevick-Muraca. Developments toward diagnostic breast cancer imaging using near-infrared optical measurements and fluorescent contrast agents. *Neoplasia (New York, N.Y.)*, 2(5):388–417, 2000.

[20] V. Ntziachristos and B. Chance. Probing physiology and molecular function using optical imaging: applications to breast cancer. *Breast cancer research : BCR*, 3(1):41–6, 2001.

[21] E. M. Sevick-muraca, J. P. Houston, and M. Gurfinkel. Fluorescence-enhanced, near infrared diagnostic imaging with contrast agents. *Current opinion in chemical biology*, 6(5):642–50, 2002.

[22] D. J. Cuccia, F. Bevilacqua, A. J. Durkin, S. Merritt, B. J. Tromberg, G. Gulsen, H. Yu, J. Wang, and O. Nalcioglu. In vivo quantification of optical contrast agent dynamics in rat tumors by use of diffuse optical spectroscopy with magnetic resonance imaging coregistration. *Applied optics*, 42(16):2940–50, 2003.

[23] N. Shah, A. E. Cerussi, D. Jakubowski, D. Hsiang, J. Butler, and B. J. Tromberg. The role of diffuse optical spectroscopy in the clinical management of breast cancer. *Disease markers*, 19(2-3): 95–105, 2004.

[24] D. A. Boas and A. G. Yodh. Spatially varying dynamical properties of turbid media probed with diffusing temporal light correlation. *Journal of the Optical Society of America A*, 14(1):192, 1997.

[25] D. Boas, L. Campbell, and A. Yodh. Scattering and Imaging with Diffusing Temporal Field Correlations. *Physical Review Letters*, 75(9):1855–1858, 1995.

[26] R. C. Mesquita, T. Durduran, G. Yu, E. M. Buckley, M. N. Kim, C. Zhou, R. Choe, U. Sunar, and A. G. Yodh. Direct measurement of tissue blood flow and metabolism with diffuse optics. *Philosophical transactions. Series A, Mathematical, physical, and engineering sciences*, 369(1955):4390–406, 2011.

[27] G. Yu. Near-infrared diffuse correlation spectroscopy in cancer diagnosis and therapy monitoring. *Journal of biomedical optics*, 17(1):010901, 2012.

[28] G. Yu. Diffuse Correlation Spectroscopy (DCS): A Diagnostic Tool for Assessing Tissue Blood Flow in Vascular-Related Diseases and Therapies. *Current Medical Imaging Reviews*, 8(3):194–210, 2012.

[29] G. Maret. Diffusing-wave spectroscopy. *Current Opinion in Colloid & Interface Science*, 2(3):251–257, 1997.

[30] M. Ninck, M. Untenberger, and T. Gisler. Diffusing-wave spectroscopy with dynamic contrast variation: disentangling the effects of blood flow and extravascular tissue shearing on signals from deep tissue. *Biomedical optics express*, 1(5):1502–1513, 2010.

[31] J. Li, F. Jaillon, G. Dietsche, G. Maret, and T. Gisler. Pulsation-resolved deep tissue dynamics measured with diffusing-wave spectroscopy. *Optics express*, 14(17):7841–51, 2006.

[32] T. Durduran, G. Yu, M. G. Burnett, J. A. Detre, J. H. Greenberg, J. Wang, C. Zhou, and A. G. Yodh. Diffuse optical measurement of blood flow, blood oxygenation, and metabolism in a human brain during sensorimotor cortex activation. *Optics letters*, 29 (15):1766–8, 2004.

[33] G. Yu, T. F. Floyd, T. Durduran, C. Zhou, J. Wang, J. A. Detre, and A. G. Yodh. Validation of diffuse correlation spectroscopy for muscle blood flow with concurrent arterial spin labeled perfusion MRI. *Optics express*, 15(3):1064–75, 2007.

[34] T. Durduran, C. Zhou, E. M. Buckley, M. N. Kim, G. Yu, R. Choe, J. W. Gaynor, T. L. Spray, S. M. Durning, S. E. Mason, L. M. Montenegro, S. C. Nicolson, R. A. Zimmerman, M. E. Putt, J. Wang, J. H. Greenberg, J. A. Detre, A. G. Yodh, and D. J. Licht. Optical measurement of cerebral hemodynamics and oxygen metabolism in neonates with congenital heart defects. *Journal of biomedical optics*, 15(3):37004, 2010.

[35] S. a. Carp, G. P. Dai, D. a. Boas, M. a. Franceschini, and Y. R. Kim. Validation of diffuse correlation spectroscopy measurements of rodent cerebral blood flow with simultaneous arterial spin labeling MRI; towards MRI-optical continuous cerebral metabolic monitoring. *Biomedical optics express*, 1(2):553–565, 2010.

[36] E. M. Buckley, D. Hance, T. Pawlowski, J. Lynch, F. B. Wilson, R. C. Mesquita, T. Durduran, L. K. Diaz, M. E. Putt, D. J. Licht,

M. a. Fogel, and A. G. Yodh. Validation of diffuse correlation spectroscopic measurement of cerebral blood flow using phase-encoded velocity mapping magnetic resonance imaging. *Journal of biomedical optics*, 17(3):037007, 2012.

[37] G. Yu, T. Durduran, C. Zhou, H.-W. Wang, M. E. Putt, H. M. Saunders, C. M. Sehgal, E. Glatstein, A. G. Yodh, and T. M. Busch. Noninvasive monitoring of murine tumor blood flow during and after photodynamic therapy provides early assessment of therapeutic efficacy. *Clinical cancer research : an official journal of the American Association for Cancer Research*, 11(9):3543–52, 2005.

[38] C. Menon, G. M. Polin, I. Prabakaran, A. Hsi, C. Cheung, J. P. Culver, J. F. Pingpank, C. S. Sehgal, A. G. Yodh, D. G. Buerk, and Others. An integrated approach to measuring tumor oxygen status using human melanoma xenografts as a model. *Cancer research*, 63(21):7232–7240, 2003.

[39] R. Choe, M. E. Putt, P. M. Carlile, T. Durduran, J. M. Giammarco, D. R. Busch, K. W. Jung, B. J. Czerniecki, J. Tchou, M. D. Feldman, C. Mies, M. A. Rosen, M. D. Schnall, A. DeMichele, and A. G. Yodh. Optically measured microvascular blood flow contrast of malignant breast tumors. *PloS one*, 9(6): e99683, 2014.

[40] E. M. Buckley, N. M. Cook, T. Durduran, M. N. Kim, C. Zhou, R. Choe, G. Yu, S. Schultz, C. M. Sehgal, D. J. Licht, P. H. Arger, M. E. Putt, H. H. Hurt, and A. G. Yodh. Cerebral hemodynamics in preterm infants during positional intervention measured with diffuse correlation spectroscopy and transcranial Doppler ultrasound. *Optics express*, 17(15):12571–81, 2009.

[41] N. Roche-Labarbe, S. a. Carp, A. Surova, M. Patel, D. a. Boas, P. E. Grant, and M. A. Franceschini. Noninvasive optical measures of CBV, StO(2), CBF index, and rCMRO(2) in human premature neonates' brains in the first six weeks of life. *Human brain mapping*, 31(3):341–52, 2010.

[42] P. Zirak, R. Delgado-Mederos, J. Martí-Fàbregas, and T. Durduran. Effects of acetazolamide on the micro- and macro-vascular cerebral hemodynamics: a diffuse optical and transcranial doppler

ultrasound study. *Biomedical optics express*, 1(5):1443–1459, 2010.

[43] R. C. Mesquita, N. Skuli, M. N. Kim, J. Liang, S. Schenkel, A. J. Majmundar, M. C. Simon, and A. G. Yodh. Hemodynamic and metabolic diffuse optical monitoring in a mouse model of hindlimb ischemia. *Biomedical optics express*, 1(4):1173–1187, 2010.

[44] Y. Shang, L. Chen, M. Toborek, and G. Yu. Diffuse optical monitoring of repeated cerebral ischemia in mice. *Optics express*, 19 (21):20301–15, 2011.

[45] C. Zhou, S. a. Eucker, T. Durduran, G. Yu, J. Ralston, S. H. Friess, R. N. Ichord, S. S. Margulies, and A. G. Yodh. Diffuse optical monitoring of hemodynamic changes in piglet brain with closed head injury. *Journal of biomedical optics*, 14(3):034015, 2009.

[46] M. N. Kim, T. Durduran, S. Frangos, B. L. Edlow, E. M. Buckley, H. E. Moss, C. Zhou, G. Yu, R. Choe, E. Maloney-Wilensky, R. L. Wolf, M. S. Grady, J. H. Greenberg, J. M. Levine, A. G. Yodh, J. A. Detre, and W. A. Kofke. Noninvasive measurement of cerebral blood flow and blood oxygenation using near-infrared and diffuse correlation spectroscopies in critically brain-injured adults. *Neurocritical care*, 12(2):173–80, 2010.

[47] T. Durduran and A. G. Yodh. Diffuse correlation spectroscopy for non-invasive, micro-vascular cerebral blood flow measurement. *NeuroImage*, 85 Pt 1:51–63, 2014.

[48] J. Selb, D. a. Boas, S.-T. Chan, K. C. Evans, E. M. Buckley, and S. a. Carp. Sensitivity of near-infrared spectroscopy and diffuse correlation spectroscopy to brain hemodynamics: simulations and experimental findings during hypercapnia. *Neurophotonics*, 1(1): 015005, 2014.

[49] D. a. Goff, E. M. Buckley, T. Durduran, J. Wang, and D. J. Licht. Noninvasive cerebral perfusion imaging in high-risk neonates. *Seminars in perinatology*, 34(1):46–56, 2010.

[50] F. Scholkmann, S. Kleiser, A. J. Metz, R. Zimmermann, J. Mata Pavia, U. Wolf, and M. Wolf. A review on continuous wave

functional near-infrared spectroscopy and imaging instrumentation and methodology. *NeuroImage*, 2013.

[51] A. Torricelli, D. Contini, A. Pifferi, M. Caffini, R. Re, L. Zucchelli, and L. Spinelli. Time domain functional NIRS imaging for human brain mapping. *NeuroImage*, 85 Pt 1:28–50, 2014.

[52] D. R. Busch, R. Choe, M. a. Rosen, W. Guo, T. Durduran, M. D. Feldman, C. Mies, B. J. Czerniecki, J. Tchou, A. Demichele, M. D. Schnall, and A. G. Yodh. Optical malignancy parameters for monitoring progression of breast cancer neoadjuvant chemotherapy. *Biomedical optics express*, 4(1):105–21, 2013.

[53] D. R. Busch, R. Choe, T. Durduran, and A. G. Yodh. Towards non-invasive characterization of breast cancer and cancer metabolism with diffuse optics. *PET clinics*, 8(3):345–365, 2013.

[54] R. Choe and T. Durduran. Diffuse Optical Monitoring of the Neoadjuvant Breast Cancer Therapy. *IEEE journal of selected topics in quantum electronics : a publication of the IEEE Lasers and Electro-optics Society*, 18(4):1367–1386, 2012.

[55] D. R. Leff, O. J. Warren, L. C. Enfield, A. Gibson, T. Athanasiou, D. K. Patten, J. Hebden, G. Z. Yang, and A. Darzi. Diffuse optical imaging of the healthy and diseased breast: a systematic review. *Breast cancer research and treatment*, 108(1):9–22, 2008.

[56] J. Li, G. Dietsche, D. Iftime, S. E. Skipetrov, G. Maret, T. Elbert, B. Rockstroh, and T. Gisler. Noninvasive detection of functional brain activity with near-infrared diffusing-wave spectroscopy. *Journal of biomedical optics*, 10(4):44002, 2005.

[57] J. Li, M. Ninck, L. Koban, T. Elbert, J. Kissler, and T. Gisler. Transient functional blood flow change in the human brain measured noninvasively by diffusing-wave spectroscopy. *Optics letters*, 33(19):2233–5, 2008.

[58] S. Nioka, Q. Luo, and B. Chance. Human brain functional imaging with reflectance CWS. *Advances in experimental medicine and biology*, 428:237–42, 1997.

[59] G. Strangman, J. P. Culver, J. H. Thompson, and D. a. Boas. A Quantitative Comparison of Simultaneous BOLD fMRI and NIRS

Recordings during Functional Brain Activation. *NeuroImage*, 17 (2):719–731, 2002.

[60] B. R. White, A. Z. Snyder, A. L. Cohen, S. E. Petersen, M. E. Raichle, B. L. Schlaggar, and J. P. Culver. Resting-state functional connectivity in the human brain revealed with diffuse optical tomography. *NeuroImage*, 47(1):148–56, 2009.

[61] D. a. Benaron, S. R. Hintz, A. Villringer, D. Boas, A. Kleinschmidt, J. Frahm, C. Hirth, H. Obrig, J. C. van Houten, E. L. Kermit, W. F. Cheong, and D. K. Stevenson. Noninvasive functional imaging of human brain using light. *Journal of cerebral blood flow and metabolism : official journal of the International Society of Cerebral Blood Flow and Metabolism*, 20(3):469–77, 2000.

[62] A. M. Siegel, J. P. Culver, J. B. Mandeville, and D. a. Boas. Temporal comparison of functional brain imaging with diffuse optical tomography and fMRI during rat forepaw stimulation. *Physics in medicine and biology*, 48(10):1391–403, 2003.

[63] V. Toronov, A. Webb, J. H. Choi, M. Wolf, A. Michalos, E. Gratton, and D. Hueber. Investigation of human brain hemodynamics by simultaneous near-infrared spectroscopy and functional magnetic resonance imaging. *Medical Physics*, 28(4):521, 2001.

[64] D. a. Boas and A. M. Dale. Simulation study of magnetic resonance imaging-guided cortically constrained diffuse optical tomography of human brain function. *Applied optics*, 44(10):1957–68, 2005.

[65] D. a. Boas, A. M. Dale, and M. A. Franceschini. Diffuse optical imaging of brain activation: approaches to optimizing image sensitivity, resolution, and accuracy. *NeuroImage*, 23 Suppl 1:S275–88, 2004.

[66] D. a. Boas, T. Gaudette, G. Strangman, X. Cheng, J. J. Marota, and J. B. Mandeville. The accuracy of near infrared spectroscopy and imaging during focal changes in cerebral hemodynamics. *NeuroImage*, 13(1):76–90, 2001.

[67] M. A. Franceschini, H. Radhakrishnan, K. Thakur, W. Wu, S. Ruvinskaya, S. Carp, and D. a. Boas. The effect of different anesthetics on neurovascular coupling. *NeuroImage*, 51(4):1367–77, 2010.

[68] A. Siegel, J. J. Marota, and D. Boas. Design and evaluation of a continuous-wave diffuse optical tomography system. *Optics express*, 4(8):287–98, 1999.

[69] R. Reif, M. Wang, S. Joshi, O. A'Amar, and I. J. Bigio. Optical method for real-time monitoring of drug concentrations facilitates the development of novel methods for drug delivery to brain tissue. *Journal of biomedical optics*, 12(3):034036, 2014.

[70] S. Joshi, R. Reif, M. Wang, J. Zhang, A. Ergin, J. N. Bruce, R. L. Fine, and I. J. Bigio. Intra-arterial mitoxantrone delivery in rabbits: an optical pharmacokinetic study. *Neurosurgery*, 69(3): 706–12; discussion 712, 2011.

[71] J. P. Culver, T. Durduran, D. Furuya, C. Cheung, J. H. Greenberg, and A. G. Yodh. Diffuse optical tomography of cerebral blood flow, oxygenation, and metabolism in rat during focal ischemia. *Journal of cerebral blood flow and metabolism : official journal of the International Society of Cerebral Blood Flow and Metabolism*, 23(8):911–24, 2003.

[72] T. Durduran, M. G. Burnett, G. Yu, C. Zhou, D. Furuya, A. G. Yodh, J. A. Detre, and J. H. Greenberg. Spatiotemporal quantification of cerebral blood flow during functional activation in rat somatosensory cortex using laser-speckle flowmetry. *Journal of cerebral blood flow and metabolism : official journal of the International Society of Cerebral Blood Flow and Metabolism*, 24(5): 518–25, 2004.

[73] W. B. Baker, Z. Sun, T. Hiraki, M. E. Putt, T. Durduran, M. Reivich, A. G. Yodh, and J. H. Greenberg. Neurovascular coupling varies with level of global cerebral ischemia in a rat model. *Journal of cerebral blood flow and metabolism : official journal of the International Society of Cerebral Blood Flow and Metabolism*, 33(1):97–105, 2013.

[74] J. Luckl, W. Baker, Z.-H. Sun, T. Durduran, A. G. Yodh, and J. H. Greenberg. The biological effect of contralateral forepaw stimulation in rat focal cerebral ischemia: a multispectral optical imaging study. *Frontiers in neuroenergetics*, 2(July):1–9, 2010.

[75] M. Diop, K. Verdecchia, T.-Y. Lee, and K. St Lawrence. Calibration of diffuse correlation spectroscopy with a time-resolved

near-infrared technique to yield absolute cerebral blood flow measurements. *Biomedical optics express*, 3(6):1476–7, 2012.

[76] C. Zhou, G. Yu, D. Furuya, J. Greenberg, A. Yodh, and T. Durduran. Diffuse optical correlation tomography of cerebral blood flow during cortical spreading depression in rat brain. *Optics express*, 14(3):1125–44, 2006.

[77] C. Cheung, J. P. Culver, K. Takahashi, J. H. Greenberg, and A. G. Yodh. In vivo cerebrovascular measurement combining diffuse near-infrared absorption and correlation spectroscopies. *Physics in medicine and biology*, 46(8):2053–65, 2001.

[78] C. G. Favilla, R. C. Mesquita, M. Mullen, T. Durduran, X. Lu, M. N. Kim, D. L. Minkoff, S. E. Kasner, J. H. Greenberg, A. G. Yodh, and J. a. Detre. Optical Bedside Monitoring of Cerebral Blood Flow in Acute Ischemic Stroke Patients During Head-of-Bed Manipulation. *Stroke; a journal of cerebral circulation*, pages 1–6, 2014.

[79] T. Durduran, C. Zhou, B. L. Edlow, G. Yu, R. Choe, M. N. Kim, B. L. Cucchiara, M. E. Putt, Q. Shah, S. E. Kasner, J. H. Greenberg, A. G. Yodh, and J. A. Detre. Transcranial optical monitoring of cerebrovascular hemodynamics in acute stroke patients. *Optics express*, 17(5):3884–902, 2009.

[80] P. Zirak, R. Delgado-Mederos, L. Dinia, D. Carrera, J. Martí-Fàbregas, and T. Durduran. Transcranial diffuse optical monitoring of microvascular cerebral hemodynamics after thrombolysis in ischemic stroke. *Journal of biomedical optics*, 19(1):18002, 2014.

[81] M. Dehaes, A. Aggarwal, P.-Y. Lin, C. Rosa Fortuno, A. Fenoglio, N. Roche-Labarbe, J. S. Soul, M. A. Franceschini, and P. E. Grant. Cerebral oxygen metabolism in neonatal hypoxic ischemic encephalopathy during and after therapeutic hypothermia. *Journal of cerebral blood flow and metabolism : official journal of the International Society of Cerebral Blood Flow and Metabolism*, 34 (1):87–94, 2014.

[82] V. Jain, E. M. Buckley, D. J. Licht, J. M. Lynch, P. J. Schwab, M. Y. Naim, N. a. Lavin, S. C. Nicolson, L. M. Montenegro, A. G. Yodh, and F. W. Wehrli. Cerebral oxygen metabolism in neonates

with congenital heart disease quantified by MRI and optics. *Journal of cerebral blood flow and metabolism : official journal of the International Society of Cerebral Blood Flow and Metabolism*, 34 (3):380–8, 2014.

[83] N. Roche-Labarbe, A. Fenoglio, H. Radhakrishnan, M. Kocienski-Filip, S. a. Carp, J. Dubb, D. a. Boas, P. E. Grant, and M. A. Franceschini. Somatosensory evoked changes in cerebral oxygen consumption measured non-invasively in premature neonates. *NeuroImage*, 85 Pt 1:279–86, 2014.

[84] N. Roche-Labarbe, A. Fenoglio, A. Aggarwal, M. Dehaes, S. a. Carp, M. A. Franceschini, and P. E. Grant. Near-infrared spectroscopy assessment of cerebral oxygen metabolism in the developing premature brain. *Journal of cerebral blood flow and metabolism : official journal of the International Society of Cerebral Blood Flow and Metabolism*, 32(3):481–8, 2012.

[85] P.-Y. Lin, N. Roche-Labarbe, M. Dehaes, S. Carp, A. Fenoglio, B. Barbieri, K. Hagan, P. E. Grant, and M. A. Franceschini. Noninvasive optical measurement of cerebral metabolism and hemodynamics in infants. *Journal of visualized experiments : JoVE*, (73):e4379, 2013.

[86] E. M. Buckley, M. Y. Naim, J. M. Lynch, D. a. Goff, P. J. Schwab, L. K. Diaz, S. C. Nicolson, L. M. Montenegro, N. a. Lavin, T. Durduran, T. L. Spray, J. W. Gaynor, M. E. Putt, a. G. Yodh, M. a. Fogel, and D. J. Licht. Sodium bicarbonate causes dose-dependent increases in cerebral blood flow in infants and children with single-ventricle physiology. *Pediatric research*, 73(5):668–73, 2013.

[87] M. N. Kim, B. L. Edlow, T. Durduran, S. Frangos, R. C. Mesquita, J. M. Levine, J. H. Greenberg, A. G. Yodh, and J. a. Detre. Continuous Optical Monitoring of Cerebral Hemodynamics During Head-of-Bed Manipulation in Brain-Injured Adults. *Neurocritical care*, pages 1–11, 2013.

[88] K. Vishwanath, D. Klein, K. Chang, T. Schroeder, M. W. Dewhirst, and N. Ramanujam. Quantitative optical spectroscopy can identify long-term local tumor control in irradiated murine head and neck xenografts. *Journal of biomedical optics*, 14(5): 054051, 2009.

[89] R. Choe, S. D. Konecky, A. Corlu, K. Lee, T. Durduran, D. R. Busch, S. Pathak, B. J. Czerniecki, J. Tchou, D. L. Fraker, A. Demichele, B. Chance, S. R. Arridge, M. Schweiger, J. P. Culver, M. D. Schnall, M. E. Putt, M. a. Rosen, and A. G. Yodh. Differentiation of benign and malignant breast tumors by in-vivo three-dimensional parallel-plate diffuse optical tomography. *Journal of biomedical optics*, 14(2):024020, 2014.

[90] P. Taroni, A. Pifferi, G. Quarto, L. Spinelli, A. Torricelli, F. Abbate, A. Villa, N. Balestreri, S. Menna, E. Cassano, and R. Cubeddu. Noninvasive assessment of breast cancer risk using time-resolved diffuse optical spectroscopy. *Journal of biomedical optics*, 15(6):060501, 2010.

[91] J. S. Soares, I. Barman, N. C. Dingari, Z. Volynskaya, W. Liu, N. Klein, D. Plecha, R. R. Dasari, and M. Fitzmaurice. Diagnostic power of diffuse reflectance spectroscopy for targeted detection of breast lesions with microcalcifications. *Proceedings of the National Academy of Sciences of the United States of America*, 110(2):471–6, 2013.

[92] Z. Volynskaya, A. S. Haka, K. L. Bechtel, M. Fitzmaurice, R. Shenk, N. Wang, J. Nazemi, R. R. Dasari, and M. S. Feld. Diagnosing breast cancer using diffuse reflectance spectroscopy and intrinsic fluorescence spectroscopy. *Journal of biomedical optics*, 13(2):024012, 2008.

[93] N. Shah, A. Cerussi, C. Eker, J. Espinoza, J. Butler, J. Fishkin, R. Hornung, and B. Tromberg. Noninvasive functional optical spectroscopy of human breast tissue. *Proceedings of the National Academy of Sciences of the United States of America*, 98(8):4420–5, 2001.

[94] B. J. Tromberg, N. Shah, R. Lanning, A. Cerussi, J. Espinoza, T. Pham, L. Svaasand, and J. Butler. Non-invasive in vivo characterization of breast tumors using photon migration spectroscopy. *Neoplasia (New York, N.Y.)*, 2(1-2):26–40, 2000.

[95] C. Zhou, R. Choe, N. Shah, T. Durduran, G. Yu, A. Durkin, D. Hsiang, R. Mehta, J. Butler, A. Cerussi, B. J. Tromberg, and A. G. Yodh. Diffuse optical monitoring of blood flow and oxygenation in human breast cancer during early stages of neoadjuvant chemotherapy. *Journal of biomedical optics*, 12(5):051903, 2007.

[96] T. Durduran, R. Choe, G. Yu, C. Zhou, J. C. Tchou, B. J. Czerniecki, and A. G. Yodh. Diffuse optical measurement of blood flow in breast tumors. *Optics letters*, 30(21):2915–7, 2005.

[97] J. Q. Brown, L. G. Wilke, J. Geradts, S. a. Kennedy, G. M. Palmer, and N. Ramanujam. Quantitative optical spectroscopy: a robust tool for direct measurement of breast cancer vascular oxygenation and total hemoglobin content in vivo. *Cancer research*, 69(7):2919–26, 2009.

[98] M. G. Pakalniskis, W. A. Wells, M. C. Schwab, H. M. Froehlich, S. Jiang, Z. Li, T. D. Tosteson, S. P. Poplack, P. A. Kaufman, B. W. Pogue, and K. D. Paulsen. Tumor angiogenesis change estimated by using diffuse optical spectroscopic tomography: demonstrated correlation in women undergoing neoadjuvant chemotherapy for invasive breast cancer? *Radiology*, 259(2):365–74, 2011.

[99] V. Ntziachristos, a. G. Yodh, M. D. Schnall, and B. Chance. MRI-guided diffuse optical spectroscopy of malignant and benign breast lesions. *Neoplasia (New York, N.Y.)*, 4(4):347–54, 2002.

[100] A. Cerussi, D. Hsiang, N. Shah, R. Mehta, A. Durkin, J. Butler, and B. J. Tromberg. Predicting response to breast cancer neoadjuvant chemotherapy using diffuse optical spectroscopy. *Proceedings of the National Academy of Sciences of the United States of America*, 104(10):4014–9, 2007.

[101] D. Roblyer, S. Ueda, A. Cerussi, W. Tanamai, A. Durkin, R. Mehta, D. Hsiang, J. a. Butler, C. McLaren, W.-P. Chen, and B. Tromberg. Optical imaging of breast cancer oxyhemoglobin flare correlates with neoadjuvant chemotherapy response one day after starting treatment. *Proceedings of the National Academy of Sciences of the United States of America*, 108(35):14626–31, 2011.

[102] P. Taroni, A. Torricelli, L. Spinelli, A. Pifferi, F. Arpaia, G. Danesini, and R. Cubeddu. Time-resolved optical mammography between 637 and 985 nm: clinical study on the detection and identification of breast lesions. *Physics in medicine and biology*, 50(11):2469–88, 2005.

[103] P. Taroni, D. Comelli, A. Pifferi, A. Torricelli, and R. Cubeddu. Absorption of collagen: effects on the estimate of breast compo-

sition and related diagnostic implications. *Journal of biomedical optics*, 12(1):014021, 2014.

[104] B. J. Tromberg, A. Cerussi, N. Shah, M. Compton, A. Durkin, D. Hsiang, J. Butler, and R. Mehta. Imaging in breast cancer: diffuse optics in breast cancer: detecting tumors in pre-menopausal women and monitoring neoadjuvant chemotherapy. *Breast cancer research : BCR*, 7(6):279–85, 2005.

[105] E. L. Hull, D. L. Conover, and T. H. Foster. Carbogen-induced changes in rat mammary tumour oxygenation reported by near infrared spectroscopy. *British journal of cancer*, 79(11-12):1709–16, 1999.

[106] J. H. Woodhams, L. Kunz, S. G. Bown, and a. J. MacRobert. Correlation of real-time haemoglobin oxygen saturation monitoring during photodynamic therapy with microvascular effects and tissue necrosis in normal rat liver. *British journal of cancer*, 91 (4):788–94, 2004.

[107] H.-w. Wang, M. E. Putt, M. J. Emanuele, D. B. Shin, E. Glatstein, A. G. Yodh, and T. M. Busch. Treatment-induced changes in tumor oxygenation predict photodynamic therapy outcome. *Cancer research*, 64(20):7553–61, 2004.

[108] R. A. Weersink, J. E. Hayward, K. R. Diamond, and M. S. Patterson. Accuracy of Noninvasive in vivo Measurements of Photosensitizer Uptake Based on a Diffusion Model of Reflectance Spectroscopy. *Photochemistry and Photobiology*, 66(3):326–335, 1997.

[109] H.-W. Wang, E. Rickter, M. Yuan, E. P. Wileyto, E. Glatstein, A. Yodh, and T. M. Busch. Effect of photosensitizer dose on fluence rate responses to photodynamic therapy. *Photochemistry and photobiology*, 83(5):1040–8, 2007.

[110] T. L. Becker, A. D. Paquette, K. R. Keymel, B. W. Henderson, and U. Sunar. Monitoring blood flow responses during topical ALA-PDT. *Biomedical optics express*, 2(1):123–30, 2010.

[111] D.-J. Cheon and S. Orsulic. Mouse models of cancer. *Annual review of pathology*, 6:95–119, 2011.

[112] N. E. Sharpless and R. A. Depinho. The mighty mouse: genetically engineered mouse models in cancer drug development. *Nature reviews. Drug discovery*, 5(9):741–54, 2006.

[113] J. E. Talmadge, R. K. Singh, I. J. Fidler, and A. Raz. Murine models to evaluate novel and conventional therapeutic strategies for cancer. *The American journal of pathology*, 170(3):793–804, 2007.

[114] M. Belau, M. Ninck, G. Hering, L. Spinelli, D. Contini, A. Torricelli, and T. Gisler. Noninvasive observation of skeletal muscle contraction using near-infrared time-resolved reflectance and diffusing-wave spectroscopy. *Journal of biomedical optics*, 15(5): 057007, 2010.

[115] K. Gurley, Y. Shang, and G. Yu. Noninvasive optical quantification of absolute blood flow, blood oxygenation, and oxygen consumption rate in exercising skeletal muscle. *Journal of biomedical optics*, 17(7):075010, 2012.

[116] R. C. Mesquita, M. Putt, M. Chandra, G. Yu, X. Xing, S. W. Han, G. Lech, Y. Shang, T. Durduran, C. Zhou, A. G. Yodh, and E. R. Mohler. Diffuse optical characterization of an exercising patient group with peripheral artery disease. *Journal of biomedical optics*, 18(5):57007, 2013.

[117] Y. Shang, K. Gurley, B. Symons, D. Long, R. Srikuea, L. J. Crofford, C. a. Peterson, and G. Yu. Noninvasive optical characterization of muscle blood flow, oxygenation, and metabolism in women with fibromyalgia. *Arthritis research & therapy*, 14(6):R236, 2012.

[118] Y. Shang, T. B. Symons, T. Durduran, a. G. Yodh, and G. Yu. Effects of muscle fiber motion on diffuse correlation spectroscopy blood flow measurements during exercise. *Biomedical optics express*, 1(2):500–511, 2010.

[119] G. Yu, T. Durduran, G. Lech, C. Zhou, B. Chance, E. R. Mohler, and A. G. Yodh. Time-dependent blood flow and oxygenation in human skeletal muscles measured with noninvasive near-infrared diffuse optical spectroscopies. *Journal of biomedical optics*, 10(2): 24027, 2005.

[120] A. Klose, A. H. Hielscher, K. M. Hanson, and J. Beuthan. Two-and three-dimensional optical tomography of finger joints for diagnostics of rheumatoid arthritis. In *Proc. SPIE*, volume 3566, pages 151–160. Citeseer, 1998.

[121] J. Näslund, M. Waldén, and L.-G. Lindberg. Decreased pulsatile blood flow in the patella in patellofemoral pain syndrome. *The American journal of sports medicine*, 35(10):1668–73, 2007.

[122] V. Prapavat, W. Runge, J. Mans, A. Krause, J. Beuthan, and G. Müller. The development of a finger joint phantom for the optical simulation of early inflammatory rheumatic changes. *Biomedizinische Technik. Biomedical engineering*, 42(11):319, 1997.

[123] K. Furutsu. Diffusion equation derived from space-time transport equation. *Journal of the Optical Society of America*, 70(4):360, 1980.

[124] A. Ishimaru. *Wave propagation and scattering in random media*, volume 2. Academic press New York, 1978.

[125] R. A. J. Groenhuis, H. A. Ferwerda, and J. J. T. Bosch. Scattering and absorption of turbid materials determined from reflection measurements 1: Theory. *Applied Optics*, 22(16):2456, 1983.

[126] P. D. Kaplan, M. H. Kao, A. G. Yodh, and D. J. Pine. Geometric constraints for the design of diffusing-wave spectroscopy experiments. *Applied optics*, 32(21):3828–36, 1993.

[127] M. G. Nichols, E. L. Hull, and T. H. Foster. Design and testing of a white-light, steady-state diffuse reflectance spectrometer for determination of optical properties of highly scattering systems. *Applied Optics*, 36(1):93, 1997.

[128] J. R. Mourant, T. Fuselier, J. Boyer, T. M. Johnson, and I. J. Bigio. Predictions and measurements of scattering and absorption over broad wavelength ranges in tissue phantoms. *Applied optics*, 36(4):949–57, 1997.

[129] R. M. P. Doornbos, R. Lang, M. C. Aalders, F. W. Cross, and H. J. C. M. Sterenborg. The determination of in vivo human tissue optical properties and absolute chromophore concentrations using spatially resolved steady-state diffuse reflectance spectroscopy. *Physics in Medicine and Biology*, 44(4):967–981, 1999.

[130] J. P. Culver, R. Choe, M. J. Holboke, L. Zubkov, T. Durduran, A. Slemp, V. Ntziachristos, B. Chance, and A. G. Yodh. Three-dimensional diffuse optical tomography in the parallel plane transmission geometry: Evaluation of a hybrid frequency domain/continuous wave clinical system for breast imaging. *Medical Physics*, 30(2):235, 2003.

[131] H.-W. Wang, T. C. Zhu, M. E. Putt, M. Solonenko, J. Metz, A. Dimofte, J. Miles, D. L. Fraker, E. Glatstein, S. M. Hahn, and A. G. Yodh. Broadband reflectance measurements of light penetration, blood oxygenation, hemoglobin concentration, and drug concentration in human intraperitoneal tissues before and after photodynamic therapy. *Journal of biomedical optics*, 10(1): 14004, 2005.

[132] G. Yu, T. Durduran, C. Zhou, T. C. Zhu, J. C. Finlay, T. M. Busch, S. B. Malkowicz, S. M. Hahn, and A. G. Yodh. Real-time in situ monitoring of human prostate photodynamic therapy with diffuse light. *Photochemistry and photobiology*, 82(5):1279–84, 2007.

[133] H.-W. Wang, J.-K. Jiang, C.-H. Lin, J.-K. Lin, G.-J. Huang, and J.-S. Yu. Diffuse reflectance spectroscopy detects increased hemoglobin concentration and decreased oxygenation during colon carcinogenesis from normal to malignant tumors. *Optics express*, 17(4):2805–17, 2009.

[134] P. Farzam and T. Durduran. Design of a broadband near infrared spectroscopy (NIRS) and diffuse correlation spectroscopy (DCS) device with a self-calibrated probe for experimental oncology. In *European Conferences in Biomedical Optics*, Munich, Germany, 2011.

[135] D. J. Rohrbach, N. Rigual, E. Tracy, A. Kowalczewski, K. L. Keymel, M. T. Cooper, W. Mo, H. Baumann, B. W. Henderson, and U. Sunar. Interlesion differences in the local photodynamic therapy response of oral cavity lesions assessed by diffuse optical spectroscopies. *Biomedical optics express*, 3(9):2142–53, 2012.

[136] T. Li, Y. Lin, Y. Shang, L. He, C. Huang, M. Szabunio, and G. Yu. Simultaneous measurement of deep tissue blood flow and oxygenation using noncontact diffuse correlation spectroscopy flow-oximeter. *Scientific reports*, 3:1358, 2013.

[137] R. Choe, K. Jung, H. Kim, A. Proctor, D. Byun, P. Farzam, K. Madden, T. Durduran, and E. Brown. Quantification of early hemodynamic changes induced by cyclophosphamide on breast cancer xenografts using diffuse optics. In *Biomedical Optics 2014*, page BS3A.10, Washington, D.C., 2014. Optical Society of America, OSA. ISBN 978-1-55752-997-8.

[138] J. B. Fishkin and E. Gratton. Propagation of photon-density waves in strongly scattering media containing an absorbing semi-infinite plane bounded by a straight edge. *Journal of the Optical Society of America. A, Optics and image science*, 10(1):127–40, 1993.

[139] B. W. Pogue and M. S. Patterson. Frequency-domain optical absorption spectroscopy of finite tissue volumes using diffusion theory. *Physics in Medicine and Biology*, 39(7):1157–1180, 1994.

[140] B. Chance, M. Cope, E. Gratton, N. Ramanujam, and B. Tromberg. Phase measurement of light absorption and scatter in human tissue. *Review of Scientific Instruments*, 69(10):3457, 1998.

[141] J. P. Culver, T. Durduran, C. Cheung, D. Furuya, J. H. Greenberg, and a. G. Yodh. Diffuse optical measurement of hemoglobin and cerebral blood flow in rat brain during hypercapnia, hypoxia and cardiac arrest. *Advances in experimental medicine and biology*, 510:293–7, 2003.

[142] U. Sunar, H. Quon, T. Durduran, J. Zhang, J. Du, C. Zhou, G. Yu, R. Choe, A. Kilger, R. Lustig, L. Loevner, S. Nioka, B. Chance, and A. G. Yodh. Noninvasive diffuse optical measurement of blood flow and blood oxygenation for monitoring radiation therapy in patients with head and neck tumors: a pilot study. *Journal of biomedical optics*, 11(6):064021, 2006.

[143] E. M. Buckley, J. M. Lynch, D. a. Goff, P. J. Schwab, W. B. Baker, T. Durduran, D. R. Busch, S. C. Nicolson, L. M. Montenegro, M. Y. Naim, R. Xiao, T. L. Spray, a. G. Yodh, J. W. Gaynor, and D. J. Licht. Early postoperative changes in cerebral oxygen metabolism following neonatal cardiac surgery: effects of surgical duration. *The Journal of thoracic and cardiovascular surgery*, 145 (1):196–203, 205.e1; discussion 203–5, 2013.

[144] P. Farzam, P. Zirak, T. Binzoni, and T. Durduran. Pulsatile and steady-state hemodynamics of the human patella bone by diffuse optical spectroscopy. *Physiological measurement*, 34(8):839–57, 2013.

[145] D. T. Delpy, M. Cope, P. van der Zee, S. Arridge, S. Wray, and J. Wyatt. Estimation of optical pathlength through tissue from direct time of flight measurement. *Physics in medicine and biology*, 33(12):1433–42, 1988.

[146] S. L. Jacques. Time-resolved reflectance spectroscopy in turbid tissues. *IEEE transactions on bio-medical engineering*, 36(12): 1155–61, 1989.

[147] M. Patterson, B. Chance, and B. Wilson. Time resolved reflectance and transmittance for the non-invasive measurement of tissue optical properties. *Appl. Opt*, 28(12):2331–2336, 1989.

[148] S. Andersson-Engels, R. Berg, S. Svanberg, and O. Jarlman. Time-resolved transillumination for medical diagnostics. *Optics letters*, 15(21):1179–81, 1990.

[149] V. Ntziachristos, X. Ma, and B. Chance. Time-correlated single photon counting imager for simultaneous magnetic resonance and near-infrared mammography. *Review of Scientific Instruments*, 69 (12):4221, 1998.

[150] V. Ntziachristos, X. Ma, a. G. Yodh, and B. Chance. Multichannel photon counting instrument for spatially resolved near infrared spectroscopy. *Review of Scientific Instruments*, 70(1):193, 1999.

[151] F. E. W. Schmidt, M. E. Fry, E. M. C. Hillman, J. C. Hebden, and D. T. Delpy. A 32-channel time-resolved instrument for medical optical tomography. *Review of Scientific Instruments*, 71(1):256, 2000.

[152] P. Taroni, A. Pifferi, A. Torricelli, D. Comelli, and R. Cubeddu. In vivo absorption and scattering spectroscopy of biological tissues. *Photochemical & Photobiological Sciences*, 2(2):124, 2003.

[153] A. Pifferi, A. Torricelli, P. Taroni, A. Bassi, E. Chikoidze, E. Giambattistelli, and R. Cubeddu. Optical biopsy of bone tissue: a step toward the diagnosis of bone pathologies. *Journal of biomedical optics*, 9(3):474–80, 2004.

[154] T. Svensson, S. Andersson-Engels, M. Einarsdóttír, and K. Svanberg. In vivo optical characterization of human prostate tissue using near-infrared time-resolved spectroscopy. *Journal of biomedical optics*, 12(1):014022, 2007.

[155] K. Verdecchia, M. Diop, T.-Y. Lee, and K. St Lawrence. Quantifying the cerebral metabolic rate of oxygen by combining diffuse correlation spectroscopy and time-resolved near-infrared spectroscopy. *Journal of biomedical optics*, 18(2):27007, 2013.

[156] D. R. Busch, R. Choe, T. Durduran, D. H. Friedman, W. B. Baker, A. D. Maidment, M. A. Rosen, M. D. Schnall, and A. G. Yodh. Blood Flow Reduction in Breast Tissue due to Mammographic Compression. *Academic radiology*, 21(2):151–61, 2014.

[157] P. Farzam, C. Lindner, U. Weigel, M. Suarez, A. Urbano-Ispizua, and T. Durduran. Noninvasive characterization of the healthy human manubrium using diffuse optical spectroscopies. *Physiological measurement*, 35(7):1469–1491, 2014.

[158] J. R. Lorenzo. *Principles of diffuse light propagation: Light propagation in tissues with applications in biology and medicine*. World Scientific, 2012. ISBN 978-981-4293-76-1.

[159] M. O'Leary, D. Boas, B. Chance, and A. Yodh. Refraction of diffuse photon density waves. *Physical Review Letters*, 69(18): 2658–2661, 1992.

[160] J. M. Schmitt, A. Knüttel, and J. R. Knutson. Interference of diffusive light waves. *Journal of the Optical Society of America. A, Optics and image science*, 9(10):1832–43, 1992.

[161] D. Boas, M. O'Leary, B. Chance, and A. Yodh. Scattering and wavelength transduction of diffuse photon density waves. *Physical Review E*, 47(5):R2999–R3002, 1993.

[162] B. J. Tromberg, L. O. Svaasand, T. T. Tsay, and R. C. Haskell. Properties of photon density waves in multiple-scattering media. *Applied optics*, 32(4):607–16, 1993.

[163] M. S. Patterson, S. Andersson-Engels, B. C. Wilson, and E. K. Osei. Absorption spectroscopy in tissue-simulating materials: a theoretical and experimental study of photon paths. *Applied optics*, 34(1):22–30, 1995.

[164] S. Prahl. Optical absorption of hemoglobin. *http://omlc.ogi.edu/spectra. Accessed 2013.*

[165] D. a. Boas and M. A. Franceschini. Haemoglobin oxygen saturation as a biomarker: the problem and a solution. *Philosophical transactions. Series A, Mathematical, physical, and engineering sciences*, 369(1955):4407–24, 2011.

[166] J. W. Goodman. Some fundamental properties of speckle. *Journal of the Optical Society of America*, 66(11):1145, 1976.

[167] D. J. Durian. Penetration depth for diffusing-wave spectroscopy. *Applied optics*, 34(30):7100–5, 1995.

[168] S. A. Carp, N. Roche-Labarbe, M.-A. Franceschini, V. J. Srinivasan, S. Sakadžić, and D. A. Boas. Due to intravascular multiple sequential scattering, Diffuse Correlation Spectroscopy of tissue primarily measures relative red blood cell motion within vessels. *Biomedical optics express*, 2(7):2047–54, 2011.

[169] L. He, Y. Lin, Y. Shang, B. J. Shelton, and G. Yu. Using optical fibers with different modes to improve the signal-to-noise ratio of diffuse correlation spectroscopy flow-oximeter measurements. *Journal of biomedical optics*, 18(3):37001, 2013.

[170] D. Irwin, L. Dong, Y. Shang, R. Cheng, M. Kudrimoti, S. D. Stevens, and G. Yu. Influences of tissue absorption and scattering on diffuse correlation spectroscopy blood flow measurements. *Biomedical optics express*, 2(7):1969–85, 2011.

[171] D. Koppel. Statistical accuracy in fluorescence correlation spectroscopy. *Physical Review A*, 10(6):1938–1945, 1974.

[172] P. Carmeliet and R. K. Jain. Angiogenesis in cancer and other diseases. *Nature*, 407(6801):249–57, 2000.

[173] J. Folkman. Angiogenesis in cancer, vascular, rheumatoid and other disease. *Nature Medicine*, 1(1):27–30, 1995.

[174] L. Ellis and I. Fidler. Angiogenesis and metastasis. *European Journal of Cancer*, 32(14):2451–2460, 1996.

[175] S. K. Chang, I. Rizvi, N. Solban, and T. Hasan. In vivo optical molecular imaging of vascular endothelial growth factor for monitoring cancer treatment. *Clinical cancer research : an official journal of the American Association for Cancer Research*, 14(13): 4146–53, 2008.

[176] W. a. Weber and R. Figlin. Monitoring cancer treatment with PET/CT: does it make a difference? *Journal of nuclear medicine : official publication, Society of Nuclear Medicine*, 48 Suppl 1: 36S–44S, 2007.

[177] L. Martincich, F. Montemurro, G. De Rosa, V. Marra, R. Ponzone, S. Cirillo, M. Gatti, N. Biglia, I. Sarotto, P. Sismondi, D. Regge, and M. Aglietta. Monitoring response to primary chemotherapy in breast cancer using dynamic contrast-enhanced magnetic resonance imaging. *Breast cancer research and treatment*, 83(1):67–76, 2004.

[178] H. C. Thoeny and B. D. Ross. Predicting and monitoring cancer treatment response with diffusion-weighted MRI. *Journal of magnetic resonance imaging : JMRI*, 32(1):2–16, 2010.

[179] I. F. Faneyte, J. G. Schrama, J. L. Peterse, P. L. Remijnse, S. Rodenhuis, and M. J. van de Vijver. Breast cancer response to neoadjuvant chemotherapy: predictive markers and relation with outcome. *British journal of cancer*, 88(3):406–12, 2003.

[180] C. Vale. Neoadjuvant chemotherapy in invasive bladder cancer: a systematic review and meta-analysis. *The Lancet*, 361(9373): 1927–1934, 2003.

[181] B. A. Winter-Roach, H. C. Kitchener, and T. A. Lawrie. Adjuvant (post-surgery) chemotherapy for early stage epithelial ovarian cancer. *The Cochrane database of systematic reviews*, 3:CD004706, 2012.

[182] J. E. Groopman and L. M. Itri. Chemotherapy-Induced Anemia in Adults: Incidence and Treatment. *JNCI Journal of the National Cancer Institute*, 91(19):1616–1634, 1999.

[183] Y. Y. Hon and W. E. Evans. Making TDM work to optimize cancer chemotherapy: a multidisciplinary team approach. *Clinical chemistry*, 44(2):388–400, 1998.

[184] P. Rubin and J. P. Williams. Principles of radiation oncology and cancer radiotherapy. *Clinical Oncology. 8th ed./Ed. Rubin Ph.–Philadelphia: WB Saunders compani*, page 99, 2001.

[185] L. E. Gaspar and M. Ding. A review of intensity-modulated radiation therapy. *Current oncology reports*, 10(4):294–9, 2008.

[186] S. r. M. Bentzen. Preventing or reducing late side effects of radiation therapy: radiobiology meets molecular pathology. *Nature reviews. Cancer*, 6(9):702–13, 2006.

[187] C. A. Robertson, D. H. Evans, and H. Abrahamse. Photodynamic therapy (PDT): a short review on cellular mechanisms and cancer research applications for PDT. *Journal of photochemistry and photobiology. B, Biology*, 96(1):1–8, 2009.

[188] D. E. J. G. J. Dolmans, D. Fukumura, and R. K. Jain. Photodynamic therapy for cancer. *Nature reviews. Cancer*, 3(5):380–7, 2003.

[189] U. Sunar, D. Rohrbach, N. Rigual, E. Tracy, K. Keymel, M. T. Cooper, H. Baumann, and B. H. Henderson. Monitoring photobleaching and hemodynamic responses to HPPH-mediated photodynamic therapy of head and neck cancer: a case report. *Optics express*, 18(14):14969–78, 2010.

[190] M. Schweiger, I. Nissilä, D. A. Boas, and S. R. Arridge. Image reconstruction in optical tomography in the presence of coupling errors. *Applied optics*, 46(14):2743–2756, 2007.

[191] S. L. Jacques and B. W. Pogue. Tutorial on diffuse light transport. *Journal of biomedical optics*, 13(4):041302, 2008.

[192] a. N. Bashkatov, E. a. Genina, V. I. Kochubey, and V. V. Tuchin. Optical properties of human skin, subcutaneous and mucous tissues in the wavelength range from 400 to 2000 nm. *Journal of Physics D: Applied Physics*, 38(15):2543–2555, 2005.

[193] W. G. Zijlstra, A. Buursma, and O. W. van Assendelft. *Visible and near infrared absorption spectra of human and animal haemoglobin: determination and application*. VSP, 2000.

[194] S. Takatani and M. D. Graham. Theoretical Analysis of Diffuse Reflectance from a Two-Layer Tissue Model. *IEEE Transactions on Biomedical Engineering*, BME-26(12):656–664, 1979.

[195] L. Kou, D. Labrie, and P. Chylek. Refractive indices of water and ice in the 0.65- to 2.5-µm spectral range. *Applied optics*, 32(19): 3531–40, 1993.

[196] R. Müller and S. Heinemann. Fat emulsions for parenteral nutrition II: Characterisation and physical long-term stability of Lipofundin MCTLCT. *Clinical Nutrition*, 12(5):298–309, 1993.

[197] J. Folkman. What is the evidence that tumors are angiogenesis dependent? *Journal of the National Cancer Institute*, 82(1):4–6, 1990.

[198] J. Folkman. The role of angiogenesis in tumor growth. *Seminars in cancer biology*, 3(2):65–71, 1992.

[199] J. Folkman. Role of angiogenesis in tumor growth and metastasis. *Seminars in Oncology*, 29(6):15–18, 2002.

[200] N. Ferrara, H.-P. Gerber, and J. LeCouter. The biology of VEGF and its receptors. *Nature medicine*, 9(6):669–76, 2003.

[201] J. Folkman. Angiogenesis: an organizing principle for drug discovery? *Nature reviews. Drug discovery*, 6(4):273–86, 2007.

[202] L. Moserle, G. Jiménez-Valerio, and O. Casanovas. Antiangiogenic therapies: going beyond their limits. *Cancer discovery*, 4(1):31–41, 2014.

[203] L. Hlatky, P. Hahnfeldt, and J. Folkman. Clinical application of antiangiogenic therapy: microvessel density, what it does and doesn't tell us. *Journal of the National Cancer Institute*, 94(12): 883–93, 2002.

[204] H. Hurwitz, L. Fehrenbacher, W. Novotny, T. Cartwright, J. Hainsworth, W. Heim, J. Berlin, A. Baron, S. Griffing, E. Holmgren, N. Ferrara, G. Fyfe, B. Rogers, R. Ross, and F. Kabbinavar. Bevacizumab plus irinotecan, fluorouracil, and leucovorin for metastatic colorectal cancer. *The New England journal of medicine*, 350(23):2335–42, 2004.

[205] R. S. Kerbel, J. Yu, J. Tran, S. Man, A. Viloria-Petit, G. Klement, B. L. Coomber, and J. Rak. Possible mechanisms of acquired resistance to anti-angiogenic drugs: implications for the use of combination therapy approaches. *Cancer metastasis reviews*, 20 (1-2):79–86, 2001.

[206] H. P. Eikesdal and R. Kalluri. Drug resistance associated with antiangiogenesis therapy. *Seminars in cancer biology*, 19(5):310–7, 2009.

[207] G. Bergers and D. Hanahan. Modes of resistance to anti-angiogenic therapy. *Nature reviews. Cancer*, 8(8):592–603, 2008.

[208] G. Klement, S. Baruchel, J. Rak, S. Man, K. Clark, D. J. Hicklin, P. Bohlen, and R. S. Kerbel. Continuous low-dose therapy with vinblastine and VEGF receptor-2 antibody induces sustained tumor regression without overt toxicity. *The Journal of clinical investigation*, 105(8):R15–24, 2000.

[209] O. Casanovas, D. J. Hicklin, G. Bergers, and D. Hanahan. Drug resistance by evasion of antiangiogenic targeting of VEGF signaling in late-stage pancreatic islet tumors. *Cancer cell*, 8(4):299–309, 2005.

[210] M. Pàez-Ribes, E. Allen, J. Hudock, T. Takeda, H. Okuyama, F. Viñals, M. Inoue, G. Bergers, D. Hanahan, and O. Casanovas. Antiangiogenic therapy elicits malignant progression of tumors to increased local invasion and distant metastasis. *Cancer cell*, 15 (3):220–31, 2009.

[211] M. Braunagel, A. Graser, M. Reiser, and M. Notohamiprodjo. The role of functional imaging in the era of targeted therapy of renal cell carcinoma. *World journal of urology*, 32(1):47–58, 2014.

[212] J. Allen and K. Howell. Microvascular imaging: techniques and opportunities for clinical physiological measurements. *Physiological measurement*, 35(7):R91–R141, 2014.

[213] M. S. Gee, H. M. Saunders, J. C. Lee, J. F. Sanzo, W. T. Jenkins, S. M. Evans, G. Trinchieri, C. M. Sehgal, M. D. Feldman, and W. M. Lee. Doppler ultrasound imaging detects changes in tumor perfusion during antivascular therapy associated with vascular anatomic alterations. *Cancer research*, 61(7):2974–82, 2001.

[214] D. E. Goertz, J. L. Yu, R. S. Kerbel, P. N. Burns, and F. S. Foster. High-frequency Doppler ultrasound monitors the effects of antivascular therapy on tumor blood flow. *Cancer research*, 62 (22):6371–5, 2002.

[215] J. D. Briers. Laser Doppler , speckle and related techniques for blood perfusion mapping and imaging. *Physiological measurement*, 22(4):R35–66, 2001.

[216] B. J. Vakoc, D. Fukumura, R. K. Jain, and B. E. Bouma. Cancer imaging by optical coherence tomography: preclinical progress and clinical potential. *Nature reviews. Cancer*, 12(5):363–8, 2012.

[217] M. Draijer, E. Hondebrink, T. van Leeuwen, and W. Steenbergen. Review of laser speckle contrast techniques for visualizing tissue perfusion. *Lasers in medical science*, 24(4):639–51, 2009.

[218] G. Reyes, A. Villanueva, C. García, F. J. Sancho, J. Piulats, F. Lluís, and G. Capellá. Orthotopic xenografts of human pancreatic carcinomas acquire genetic aberrations during dissemination in nude mice. *Cancer research*, 56(24):5713–9, 1996.

[219] G. Capellá, L. Farré, A. Villanueva, G. Reyes, C. García, G. Tarafa, and F. Lluís. Orthotopic models of human pancreatic cancer. *Annals of the New York Academy of Sciences*, 880 (93):103–9, 1999.

[220] K. Garber. Personal mouse colonies give hope for pancreatic cancer patients. *Journal of the National Cancer Institute*, 99(2):105–7, 2007.

[221] C. J. Bruns, M. Shrader, M. T. Harbison, C. Portera, C. C. Solorzano, K.-W. Jauch, D. J. Hicklin, R. Radinsky, and L. M. Ellis. Effect of the vascular endothelial growth factor receptor-2 antibody DC101 plus gemcitabine on growth, metastasis and angiogenesis of human pancreatic cancer growing orthotopically in nude mice. *International journal of cancer. Journal international du cancer*, 102(2):101–8, 2002.

[222] R. T. Tong, Y. Boucher, S. V. Kozin, F. Winkler, D. J. Hicklin, and R. K. Jain. Vascular normalization by vascular endothelial growth factor receptor 2 blockade induces a pressure gradient

across the vasculature and improves drug penetration in tumors. *Cancer research*, 64(11):3731–6, 2004.

[223] P. Vaupel and A. Mayer. Hypoxia in cancer: significance and impact on clinical outcome. *Cancer metastasis reviews*, 26(2): 225–39, 2007.

[224] S. Kopetz, C. Jimenez, S.-M. Tu, and P. Sharma. Pulmonary arteriovenous fistula in a patient with renal cell carcinoma. *The European respiratory journal*, 29(4):813–5, 2007.

[225] M. Sant, C. Allemani, C. Tereanu, R. De Angelis, R. Capocaccia, O. Visser, R. Marcos-Gragera, M. Maynadié, A. Simonetti, J.-M. Lutz, and F. Berrino. Incidence of hematologic malignancies in Europe by morphologic subtype: results of the HAEMACARE project. *Blood*, 116(19):3724–34, 2010.

[226] D. Rodriguez-Abreu, A. Bordoni, and E. Zucca. Epidemiology of hematological malignancies. *Annals of oncology : official journal of the European Society for Medical Oncology / ESMO*, 18 Suppl 1(Supplement 1):i3–i8, 2007.

[227] P. Greenberg, C. Cox, M. M. LeBeau, P. Fenaux, P. Morel, G. Sanz, M. Sanz, T. Vallespi, T. Hamblin, D. Oscier, K. Ohyashiki, K. Toyama, C. Aul, G. Mufti, and J. Bennett. International scoring system for evaluating prognosis in myelodysplastic syndromes. *Blood*, 89(6):2079–88, 1997.

[228] L. Malcovati, U. Germing, A. Kuendgen, M. G. Della Porta, C. Pascutto, R. Invernizzi, A. Giagounidis, B. Hildebrandt, P. Bernasconi, S. Knipp, C. Strupp, M. Lazzarino, C. Aul, and M. Cazzola. Time-dependent prognostic scoring system for predicting survival and leukemic evolution in myelodysplastic syndromes. *Journal of clinical oncology : official journal of the American Society of Clinical Oncology*, 25(23):3503–10, 2007.

[229] M. G. Alexandrakis, F. H. Passam, C. Dambaki, C. a. Pappa, and E. N. Stathopoulos. The relation between bone marrow angiogenesis and the proliferation index Ki-67 in multiple myeloma. *Journal of clinical pathology*, 57(8):856–60, 2004.

[230] D. Wolowiec, Z. Wozniak, S. Potoczek, G. Ganczarski, T. Wrobel, K. Kuliczkowski, I. Frydecka, and M. Jeleń. Bone marrow angiogenesis and proliferation in B-cell chronic lymphocytic leukemia. *Analytical and quantitative cytology and histology / the International Academy of Cytology [and] American Society of Cytology*, 26(5):263–70, 2004.

[231] T. Padró, S. Ruiz, R. Bieker, H. Bürger, M. Steins, J. Kienast, T. Büchner, W. E. Berdel, and R. M. Mesters. Increased angiogenesis in the bone marrow of patients with acute myeloid leukemia. *Blood*, 95(8):2637–44, 2000.

[232] H. F. S. Negaard, N. Iversen, I. M. Bowitz-Lothe, P. M. Sandset, B. Steinsvik, B. Ostenstad, and P. O. Iversen. Increased bone marrow microvascular density in haematological malignancies is associated with differential regulation of angiogenic factors. *Leukemia*, 23(1):162–9, 2009.

[233] M. H. Mangi and A. C. Newland. Angiogenesis and angiogenic mediators in haematological malignancies. *British Journal of Haematology*, 111(1):43–51, 2000.

[234] H. De Raeve, E. Van Marck, B. Van Camp, and K. Vanderkerken. Angiogenesis and the role of bone marrow endothelial cells in haematological malignancies. *Histology and histopathology*, 19 (3):935–50, 2004.

[235] A. Vacca, D. Ribatti, L. Roncali, G. Ranieri, G. Serio, F. Silvestris, and F. Dammacco. Bone marrow angiogenesis and progression in multiple myeloma. *British journal of haematology*, 87(3):503–8, 1994.

[236] A. R. Kini, N. E. Kay, and L. C. Peterson. Increased bone marrow angiogenesis in B cell chronic lymphocytic leukemia. *Leukemia*, 14(8):1414–1418, 2000.

[237] S. S. Bhatti, L. Kumar, A. K. Dinda, and R. Dawar. Prognostic value of bone marrow angiogenesis in multiple myeloma: use of light microscopy as well as computerized image analyzer in the assessment of microvessel density and total vascular area in multiple myeloma and its correlation with various clinical. *American journal of hematology*, 81(9):649–56, 2006.

[238] S. Kumar, M. A. Gertz, A. Dispenzieri, M. Q. Lacy, L. A. Wellik, R. Fonseca, J. A. Lust, T. E. Witzig, R. A. Kyle, P. R. Greipp, and S. V. Rajkumar. Prognostic value of bone marrow angiogenesis in patients with multiple myeloma undergoing high-dose therapy. *Bone marrow transplantation*, 34(3):235–9, 2004.

[239] S. Molica, A. Vacca, D. Ribatti, A. Cuneo, F. Cavazzini, D. Levato, G. Vitelli, L. Tucci, A. M. Roccaro, and F. Dammacco. Prognostic value of enhanced bone marrow angiogenesis in early B-cell chronic lymphocytic leukemia. *Blood*, 100(9):3344–51, 2002.

[240] P. Salven, A. Orpana, L. Teerenhovi, and H. Joensuu. Simultaneous elevation in the serum concentrations of the angiogenic growth factors VEGF and bFGF is an independent predictor of poor prognosis in non-Hodgkin lymphoma: a single-institution study of 200 patients. *Blood*, 96(12):3712–8, 2000.

[241] S. V. Rajkumar, R. A. Mesa, and A. Tefferi. A review of angiogenesis and anti-angiogenic therapy in hematologic malignancies. *Journal of hematotherapy & stem cell research*, 11(1):33–47, 2002.

[242] O. Sezer, K. Niemöller, O. Kaufmann, J. Eucker, C. Jakob, I. Zavrski, and K. Possinger. Decrease of bone marrow angiogenesis in myeloma patients achieving a remission after chemotherapy. *European journal of haematology*, 66(4):238–44, 2001.

[243] M. Bhutani, B. Turkbey, E. Tan, T. J. Kemp, L. a. Pinto, a. R. Berg, N. Korde, a. R. Minter, B. M. Weiss, E. Mena, L. Lindenberg, O. Aras, M. P. Purdue, J. N. Hofmann, S. M. Steinberg, K. R. Calvo, P. L. Choyke, I. Maric, K. Kurdziel, and O. Landgren. Bone marrow angiogenesis in myeloma and its precursor disease: a prospective clinical trial. *Leukemia*, 28(2):413–6, 2014.

[244] R. C. Zangar, D. S. Daly, and A. M. White. ELISA microarray technology as a high-throughput system for cancer biomarker validation. *Expert review of proteomics*, 3(1):37–44, 2006.

[245] H.-P. Gerber and N. Ferrara. The role of VEGF in normal and neoplastic hematopoiesis. *Journal of molecular medicine (Berlin, Germany)*, 81(1):20–31, 2003.

[246] W. Jelkmann. Pitfalls in the measurement of circulating vascular endothelial growth factor. *Clinical chemistry*, 47(4):617–23, 2001.

[247] F. Bertolini, P. Mancuso, Y. Shaked, and R. S. Kerbel. Molecular and cellular biomarkers for angiogenesis in clinical oncology. *Drug discovery today*, 12(19-20):806–12, 2007.

[248] D. Kahn, G. J. Weiner, S. Ben-Haim, L. L. Ponto, M. T. Madsen, D. L. Bushnell, G. L. Watkins, E. A. Argenyi, and R. D. Hichwa. Positron emission tomographic measurement of bone marrow blood flow to the pelvis and lumbar vertebrae in young normal adults. *Blood*, 83(4):958–63, 1994.

[249] M. Horger and R. Bares. The role of single-photon emission computed tomography/computed tomography in benign and malignant bone disease. *Seminars in nuclear medicine*, 36(4):286–94, 2006.

[250] I. McCarthy. The physiology of bone blood flow: a review. *The Journal of bone and joint surgery. American volume*, 88 Suppl 3 (suppl_2):4–9, 2006.

[251] A. J. Beer and M. Schwaiger. Imaging of integrin alphavbeta3 expression. *Cancer metastasis reviews*, 27(4):631–44, 2008.

[252] W. W. Li, M. Hutnik, and G. Gehr. Antiangiogenesis in haematological malignancies. *British journal of haematology*, 143(5): 622–31, 2008.

[253] S. Shinkaruk, M. Bayle, G. Laïn, and G. Déléris. Vascular endothelial cell growth factor (VEGF), an emerging target for cancer chemotherapy. *Current medicinal chemistry. Anti-cancer agents*, 3(2):95–117, 2003.

[254] T. Binzoni, D. Tchernin, J.-N. Hyacinthe, D. Van De Ville, and J. Richiardi. Pulsatile blood flow in human bone assessed by laser-Doppler flowmetry and the interpretation of photoplethysmographic signals. *Physiological measurement*, 34(3):N25–40, 2013.

[255] S. M. Aziz, F. Khambatta, T. Vaithianathan, J. C. Thomas, J. M. Clark, and R. Marshall. A near infrared instrument to monitor relative hemoglobin concentrations of human bone tissue in vitro and in vivo. *The Review of scientific instruments*, 81(4):043111, 2010.

[256] A. N. Bashkatov. Optical properties of human cranial bone in the spectral range from 800 to 2000 nm. *Proceedings of SPIE*, 6163: 616310–616310–11, 2006.

[257] T. Binzoni, S. Bianchi, J. H. Fasel, H. Bounameaux, E. Hiltbrand, and D. Delpy. Human tibia bone marrow blood perfusion by non-invasive near infrared spectroscopy: a new tool for studies on microgravity. *Life in space for life on earth*, 501:103–104, 2002.

[258] T. Binzoni, T. S. Leung, C. Courvoisier, R. Giust, G. Tribillon, T. Gharbi, and D. T. Delpy. Blood Volume and Haemoglobin Oxygen Content Changes in Human Bone Marrow during Orthostatic Stress. *Journal of physiological anthropology*, 25(1):1–6, 2006.

[259] T. Binzoni, T. Leung, V. Hollis, S. Bianchi, J. H. D. Fasel, H. Bounameaux, E. Hiltbrand, and D. Delpy. Human tibia bone marrow: defining a model for the study of haemodynamics as a function of age by near infrared spectroscopy. *Journal of physiological anthropology and applied human science*, 22(5):211–8, 2003.

[260] T. Binzoni, D. Boggett, and D. Van De Ville. Laser-Doppler flowmetry at large interoptode spacing in human tibia diaphysis: Monte Carlo simulations and preliminary experimental results. *Physiological Measurement*, 32:N33, 2011.

[261] T. Binzoni and D. Van De Ville. Noninvasive Probing of the Neurovascular System in Human Bone/Bone Marrow Using Near-Infrared Light. *Journal of Innovative optical health sciences*, 04 (02):183, 2011.

[262] M. Klasing and J. Zange. In vivo quantitative near-infrared spectroscopy in skeletal muscle and bone during rest and isometric exercise. In D. A. Boas, editor, *European conference on biomedical optics*, volume 5138, pages 318–322, 2003. ISBN 2203601345.

[263] M. Firbank, M. Hiraoka, M. Essenpreis, and D. T. Delpy. in the wavelength range 650-950 nm. *Physics in medicine and biology*, 38:503, 1993.

[264] J. Mateus and A. R. Hargens. Photoplethysmography for non-invasive in vivo measurement of bone hemodynamics. *Physiological Measurement*, 33(6):1027, 2012.

[265] J. Mateus and A. R. Hargens. Bone hemodynamic responses to changes in external pressure. *Bone*, 52(2):604–610, 2013.

[266] J. Näslund, J. Pettersson, T. Lundeberg, D. Linnarsson, and L.-G. Lindberg. Non-invasive continuous estimation of blood flow changes in human patellar bone. *Medical & biological engineering & computing*, 44(6):501–9, 2006.

[267] J. E. Näslund, S. Näslund, E. Lundeberg, L.-G. Lindberg, and I. Lund. Bone blood flow is influenced by muscle contractions. *Journal of biomedical science and engineering*, 04(07):490–496, 2011.

[268] N. Ugryumova, S. J. Matcher, and D. P. Attenburrow. Measurement of bone mineral density via light scattering. *Physics in medicine and biology*, 49:469, 2004.

[269] Y. Xu, N. Iftimia, H. Jiang, L. Key, and M. Bolster. Imaging of in vitro and in vivo bones and joints with continuous-wave diffuse optical tomography. *Optics express*, 8(7):447–51, 2001.

[270] Q. Zhang and H. Jiang. Three-dimensional diffuse optical imaging of hand joints: System description and phantom studies. *Optics and Lasers in Engineering*, 43(11):1237–1251, 2005.

[271] M. Y. Gordon, I. D. Douglas, H. M. Clink, and B. M. Pickering. Distribution of granulopoietic activity in the human skeleton, studied by colony growth in agar diffusion chambers. *British journal of haematology*, 32(4):537–42, 1976.

[272] J. F. Griffith, B. BAO, and Others. Age-Related Physiological Changes of the Bone Marrow and Immune System. In *Geriatric Imaging*, pages 891–904. Springer, 2013.

[273] J. Justesen, K. Stenderup, E. N. Ebbesen, L. Mosekilde, T. Steiniche, and M. Kassem. Adipocyte tissue volume in bone marrow is increased with aging and in patients with osteoporosis. *Biogerontology*, 2(3):165–171, 2001.

[274] D. R. White, H. Q. Woodard, and S. M. Hammond. Average soft-tissue and bone models for use in radiation dosimetry. *The British journal of radiology*, 60(717):907–13, 1987.

[275] J. C. Pinheiro and D. M. Bates. *Mixed-effects models in S and S-PLUS*. Springer Verlag, New York, 2000. ISBN 978-1-4419-0318-1.

[276] B. Winter. Linear models and linear mixed effects models in R with linguistic applications. page 42, 2013.

[277] D. Bates, M. Maechler, B. Bolker, and S. Walker. *lme4: Linear mixed-effects models using Eigen and S4*, 2013.

[278] A. Kuznetsova, P. Bruun Brockhoff, and R. Haubo Bojesen Christensen. *lmerTest: Tests for random and fixed effects for linear mixed effect models (lmer objects of lme4 package).*, 2013.

[279] R Core Team. *R: A Language and Environment for Statistical Computing*. R Foundation for Statistical Computing, Vienna, Austria, 2013.

[280] R. Selthofer, V. Nikolić, T. Mrcela, R. Radić, I. Leksan, I. Rudez, and K. Selthofer. Morphometric analysis of the sternum. *Collegium antropologicum*, 30(1):43–7, 2006.

[281] W. Gao-ju and W. Qing. Feasibility of manubrium sterni cancellous bone plus pyramesh in anterior cervical spinal fusion surgery. *Journal of Clinical Rehabilitative Tissue Engineering Research*, 15 (9):1698–1701, 2011.

[282] P. Xiu, D. Shui, Q. Wang, G. Wang, and Y. Lan. Anatomic and morphometric analysis of manubrium sterni as a source of autograft for anterior cervical fusion surgery using quantitative 3-dimensional computed tomographic scans. *Spine*, 37(16):E935–41, 2012.

[283] R. C. Mesquita, S. S. Schenkel, D. L. Minkoff, X. Lu, C. G. Favilla, P. M. Vora, D. R. Busch, M. Chandra, J. H. Greenberg, J. a. Detre, and a. G. Yodh. Influence of probe pressure on the diffuse correlation spectroscopy blood flow signal: extra-cerebral contributions. *Biomedical Optics Express*, 4(7):978, 2013.

[284] J. F. Griffith, D. K. W. Yeung, G. E. Antonio, F. K. H. Lee, A. W. L. Hong, S. Y. S. Wong, E. M. C. Lau, and P. C. Leung. Vertebral bone mineral density, marrow perfusion, and fat content in healthy men and men with osteoporosis: dynamic contrast-enhanced MR imaging and MR spectroscopy. *Radiology*, 236(3): 945–51, 2005.

[285] A. Arbabi. A quantitative analysis of the structure of human sternum. *Journal of medical physics*, 34(2):80–6, 2009.

[286] R. L. P. Van Veen, H. Sterenborg, and R. van Veen. Determination of VIS-NIR absorption coefficients of mammalian fat, with time-and spatially resolved diffuse reflectance and transmission spectroscopy. *Biomedical Topical Meeting, OSA Technical Digest*, pages 1–3, 2004.

[287] I. R. Reid. Relationships between fat and bone. *Osteoporosis international : a journal established as result of cooperation between the European Foundation for Osteoporosis and the National Osteoporosis Foundation of the USA*, 19(5):595–606, 2008.

[288] Y.-H. Hsu, S. a. Venners, H. a. Terwedow, Y. Feng, T. Niu, Z. Li, N. Laird, J. D. Brain, S. R. Cummings, M. L. Bouxsein, C. J. Rosen, and X. Xu. Relation of body composition, fat mass, and serum lipids to osteoporotic fractures and bone mineral density in Chinese men and women. *The American journal of clinical nutrition*, 83(1):146–54, 2006.

[289] M. A. Bredella, C. M. Gill, A. V. Gerweck, M. G. Landa, V. Kumar, S. M. Daley, M. Torriani, and K. K. Miller. Ectopic and serum lipid levels are positively associated with bone marrow fat in obesity. *Radiology*, 269(2):534–41, 2013.

[290] I. Wakabayashi. Relationships of body mass index with blood pressure and serum cholesterol concentrations at different ages. *Aging clinical and experimental research*, 16(6):461–6, 2004.

[291] M. A. Richards, J. A. Webb, S. E. Jewell, W. M. Gregory, and R. H. Reznek. In-vivo measurement of spin lattice relaxation time (T1) of bone marrow in healthy volunteers: the effects of age and sex. *The British journal of radiology*, 61:30–33, 1988.

[292] M. Brookes and W. J. Revell. *Blood supply of bone: scientific aspects*. Springer, 1998.

[293] I. B. Wilkinson and D. J. Webb. Venous occlusion plethysmography in cardiovascular research: methodology and clinical applications. *British journal of clinical pharmacology*, 52(6):631–46, 2001.

[294] J. Allen. Photoplethysmography and its application in clinical physiological measurement. *Physiological measurement*, 28(3):R1–39, 2007.

[295] J. R. Mourant, J. P. Freyer, a. H. Hielscher, a. a. Eick, D. Shen, and T. M. Johnson. Mechanisms of light scattering from biological cells relevant to noninvasive optical-tissue diagnostics. *Applied optics*, 37(16):3586–93, 1998.

[296] A. V. J. Challoner. Photoelectric plethysmography for estimating cutaneous blood flow. *Non-invasive physiological measurements*, 1:125–151, 1979.

[297] K. H. Shelley. Photoplethysmography: beyond the calculation of arterial oxygen saturation and heart rate. *Anesthesia and analgesia*, 105:S31–6, 2007.

[298] W. B. Murray and P. A. Foster. The peripheral pulse wave: information overlooked. *Journal Of Clinical Monitoring*, 12(5):365–377, 1996.

[299] A. B. Hertzman and J. B. Dillon. Applications of photoelectric plethysmography in peripheral vascular disease. *American Heart Journal*, 20(6):750–761, 1940.

[300] B. a. Feddersen, D. W. Piston, and E. Gratton. Digital parallel acquisition in frequency domain fluorimetry. *Review of Scientific Instruments*, 60(9):2929, 1989.

[301] B. Tuncali, A. Karci, B. E. Tuncali, O. Mavioglu, M. Ozkan, A. K. Bacakoglu, H. Baydur, A. Ekin, and Z. Elar. A new method for estimating arterial occlusion pressure in optimizing pneumatic tourniquet inflation pressure. *Anesthesia and analgesia*, 102(6): 1752–7, 2006.

[302] D. R. White, E. M. Widdowson, H. Q. Woodard, and J. W. Dickerson. The composition of body tissues (II). Fetus to young adult. *The British journal of radiology*, 64(758):149–59, 1991.

[303] J. Allen and A. Murray. Age-related changes in the characteristics of the photoplethysmographic pulse shape at various body sites. *Physiological measurement*, 24(2):297–307, 2003.

[304] F. Iranpour, A. M. Merican, A. a. Amis, and J. P. Cobb. The width:thickness ratio of the patella: an aid in knee arthroplasty. *Clinical orthopaedics and related research*, 466(5):1198–203, 2008.

[305] A. Kienle. Non-invasive determination of muscle blood flow in the extremities from laser Doppler spectra. *Physics in medicine and biology*, 46(4):1231, 2001.

[306] V. Quaresima, M. Ferrari, M. A. Franceschini, M. L. Hoimes, and S. Fantini. Spatial distribution of vastus lateralis blood flow and oxyhemoglobin saturation measured at the end of isometric quadriceps contraction by multichannel near-infrared spectroscopy. *Journal of biomedical optics*, 9(2):413–20, 2004.

[307] E. M. Buckley, A. B. Parthasarathy, P. E. Grant, A. G. Yodh, and M. A. Franceschini. Diffuse correlation spectroscopy for measurement of cerebral blood flow: future prospects. *Neurophotonics*, 1 (1):011009, 2014.

[308] G. Dietsche, M. Ninck, C. Ortolf, J. Li, F. Jaillon, and T. Gisler. Fiber-based multispeckle detection for time-resolved diffusing-wave spectroscopy: characterization and application to blood flow detection in deep tissue. *Applied optics*, 46(35):8506–14, 2007.

[309] G. M. Tellis, R. C. Mesquita, and a. G. Yodh. Use of Diffuse Correlation Spectroscopy To Measure Brain Blood Flow Differences During Speaking and Nonspeaking Tasks for Fluent Speakers and Persons Who Stutter. *Perspectives on Fluency and Fluency Disorders*, 21(3):96–106, 2011.

[310] F. Jaillon, J. Li, G. Dietsche, T. Elbert, and T. Gisler. Activity of the human visual cortex measured non-invasively by diffusing-wave spectroscopy. *Optics express*, 15(11):6643–50, 2007.

[311] L. Gagnon, M. Desjardins, J. Jehanne-Lacasse, L. Bherer, and F. Lesage. Investigation of diffuse correlation spectroscopy in multi-layered media including the human head. *Optics Express*, 16(20):15514, 2008.

[312] B. L. Edlow, M. N. Kim, T. Durduran, C. Zhou, M. E. Putt, A. G. Yodh, J. H. Greenberg, and J. a. Detre. The effects of healthy aging on cerebral hemodynamic responses to posture change. *Physiological measurement*, 31(4):477–95, 2010.

[313] L. Koban, M. Ninck, J. Li, T. Gisler, and J. Kissler. Processing of emotional words measured simultaneously with steady-state visually evoked potentials and near-infrared diffusing-wave spectroscopy. *BMC Neuroscience*, 11:85, 2010.

[314] P.-Y. Lin, N. Roche-Labarbe, M. Dehaes, A. Fenoglio, P. E. Grant, and M. A. Franceschini. Regional and hemispheric asymmetries of cerebral hemodynamic and oxygen metabolism in newborns. *Cerebral cortex (New York, N.Y. : 1991)*, 23(2):339–48, 2013.

[315] R. C. Mesquita, O. K. Faseyitan, P. E. Turkeltaub, E. M. Buckley, A. Thomas, M. N. Kim, T. Durduran, J. H. Greenberg, J. a. Detre, A. G. Yodh, and R. H. Hamilton. Blood flow and oxygenation changes due to low-frequency repetitive transcranial magnetic stimulation of the cerebral cortex. *Journal of biomedical optics*, 18(6):067006, 2013.

[316] L. Dong, L. He, Y. Lin, Y. Shang, and G. Yu. Simultaneously extracting multiple parameters via fitting one single autocorrelation function curve in diffuse correlation spectroscopy. *IEEE transactions on bio-medical engineering*, 60(2):361–8, 2013.

Appendix A

Design of DOS-DCS probe and spectrometer bundle

In the following pages the design of hand-held self calibrated optical probe and fiber bundle for spectrometer entrance (look at chapter 3) is presented. In the probe design M1 and M4 are main and calibration source and M5-M13 are detector fibers in DOS setup. A2 and A3 are source fibers and S1-S7 are detector fibers for DCS. DCS detector fibers (S1-S7) are single mode fibers with core diameter of 5.6 μm. The rest of fibers are multimode with core diameter of 200 μm.

The bundle drawing shows the specification of an 8 leg fiber bundle with 200 μm fiber per leg.

(5.460)

REVISIONS

REV	DESCRIPTION	DATE	APPROVED

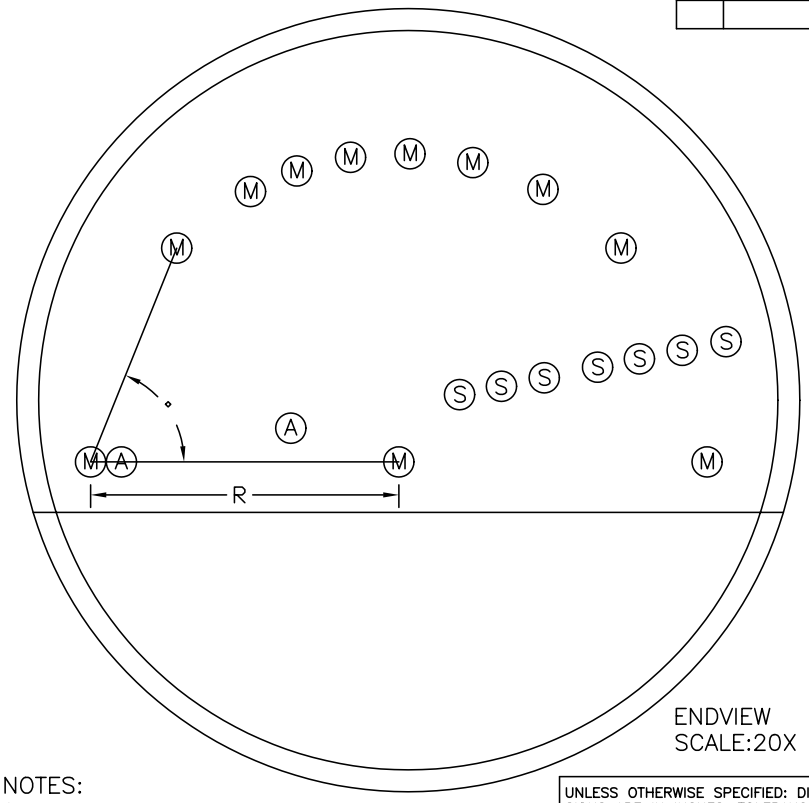

ENDVIEW
SCALE:20X

M#	(R(mm),°)
M1	(0, 0)
A2	(0.250, 0)
A3	(1.647, 9.5526)
M4	(2.5, 0)
M5	(5, 0)
M6	(4.638, 21.9510)
M7	(4.283, 31.0590)
M8	(3.937, 38.0520)
M9	(3.599, 43.9560)
M10	(3.247, 49.5090)
M11	(2.892, 54.6570)
M12	(2.547, 59.3820)
M13	(1.869, 68.0490)
S1	(3.042, 10.3314)
S2	(3.388, 10.4251)
S3	(3.742, 10.5032)
S4	(4.183 10.5819)
S5	(4.529, 10.6329)
S6	(4.883, 10.6777)
S7	(5.245, 10.7172)

NOTES:
1.

S = (7)SM800/5.6/125
M&A = (11)WF200/220/245 P22

ALL S&A FIBERS GOTO FC CONNECTORS (9)
ALL M FIBERS GOTO SMA COMNNECTORS (11)

UNLESS OTHERWISE SPECIFIED: DIMENSIONS ARE IN INCHES. TOLERANCES ARE:
ANGLES ±0.5° | DECIMALS:
CONCENTRICITY ±.002 | .X±0.1
PERPENDICULARITY ±.002. | .XX±.01
RADIUS .01 MAX | .XXX±.001
PARALLEL ±.002. | .XXXX±.0005
SURFACE FINISH ✓ OR BETTER
BREAK ALL EDGES .010 MAX.
ALL DIMENSIONS APPLY AFTER FINISH.

MATERIAL: SEE DRAWING

FINISH: NONE

FIBEROPTIC SYSTEMS, INC.
SIMI VALLEY, CA. 93065

DRAWN BY/DATE: TJ 1/19/11

TITLE: (20) FIBER PROBE, 5M

TEMPLATE NO: 70-0005
REVISION: D

SIZE: A | DWG NO.: 50-3370 | REV: 4

SCALE: 1:2 | CUSTOMER: ICFO | SHEET: 2 of 2

(5.460)

REVISIONS

REV	DESCRIPTION	DATE	APPROVED
2	1mm WAS .040", 2.0 WAS 1.0	5/27/10	TJ

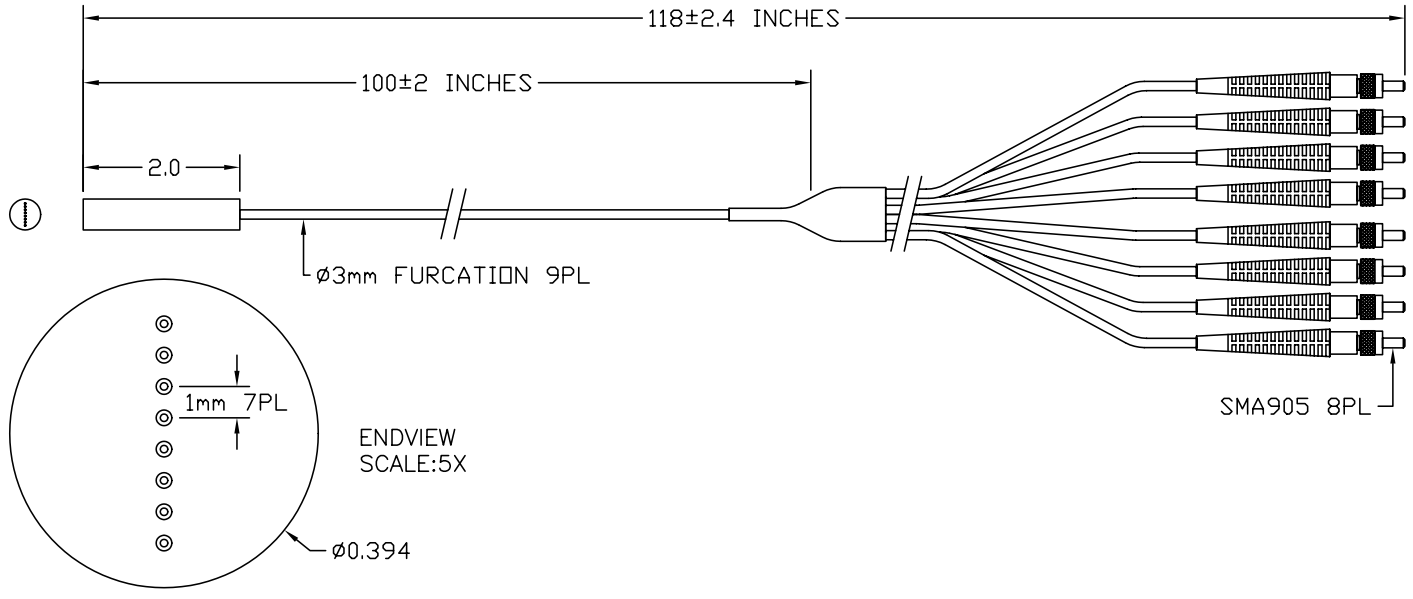

NOTES:

2. EPOXY – EPOTEK 353NDT.
3. PARTS – 20–XXXX, STAINLESS STEEL.
4. BROKEN FIBER – NONE.
5. OPERATING TEMPERATURE – 105°C MAX.
6. INSPECTION – VISUAL PER 70–0014.
7. RANDOMIZED – NO.
8. LABEL – FSI PN, REV, DATECODE.
9. POLISH – 0.3um.
10. TOOLING – STANDARD.

UNLESS OTHERWISE SPECIFIED: DIMENSIONS ARE IN INCHES. TOLERANCES ARE:

ANGLES ±0.5°	DECIMALS:
CONCENTRICITY ±.002	.X±0.1
PERPENDICULARITY ±.002.	.XX±.01
RADIUS .01 MAX	.XXX±.002
PARALLEL ±.002.	.XXXX±.0005

SURFACE FINISH √ OR BETTER

BREAK ALL EDGES .010 MAX.
ALL DIMENSIONS APPLY AFTER FINISH.

MATERIAL: SEE DRAWING

FINISH: NONE

FIBEROPTIC SYSTEMS, INC.
SIMI VALLEY, CA. 93065

DRAWN BY/DATE: TJ 5/20/10

TEMPLATE NO: 70–0005
REVISION: D

TITLE: 8 to 1 BUNDLE, 3M, SMA

SIZE: A | DWG NO.: 50–3253 | REV: 2

SCALE: 1:2 | CUSTOMER: ICFO | SHEET: 1 of 1

Appendix B

Measured optical and physiological parameters on murine tumors

In this appendix, the measured optical (absorption and reduced scattering coefficient) and physiological parameters (total hemoglobin concentration and oxygen saturation) are presented. The control mice are indicated by dashed lines and treated mice with solid lines. The number of measurement days for each mouse is different because they have been sacrificed in different days after start of the study.

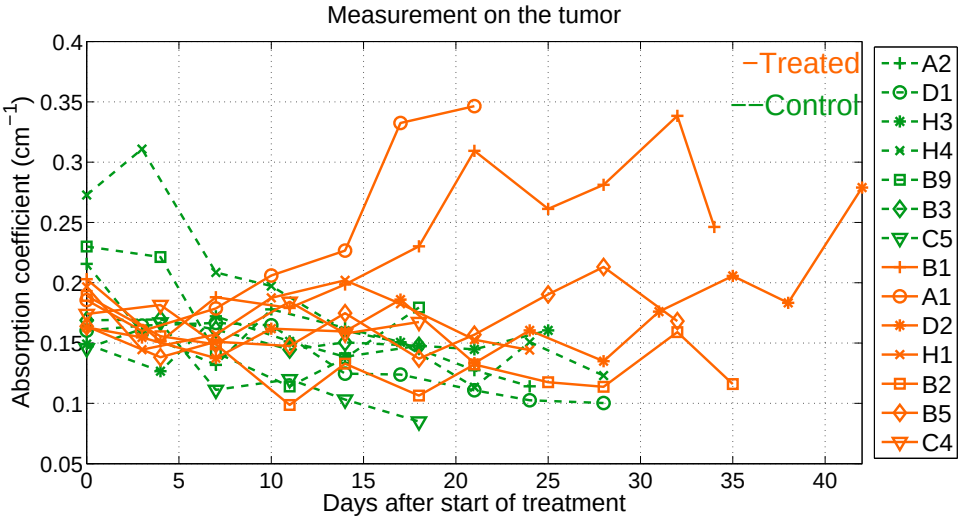

Fig. B.1 Absorption coefficient (μ_a) of both treated (solid orange lines) and control mice (dashed green lines) are presented over all days of measurement. Treated animal

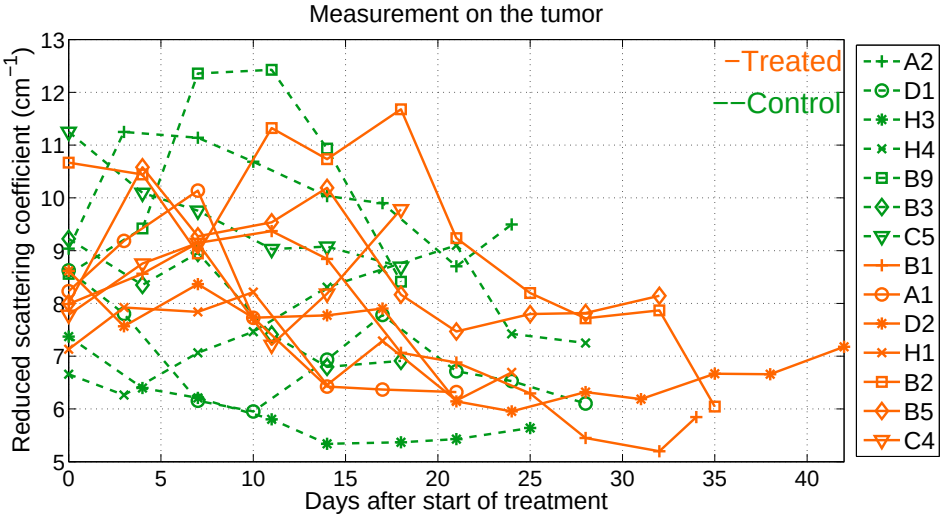

Fig. B.2 Reduced scattering coefficient (μ_s') of both treated (solid orange lines) and control mice (dashed green lines) are presented over all days of measurement. Treated animal

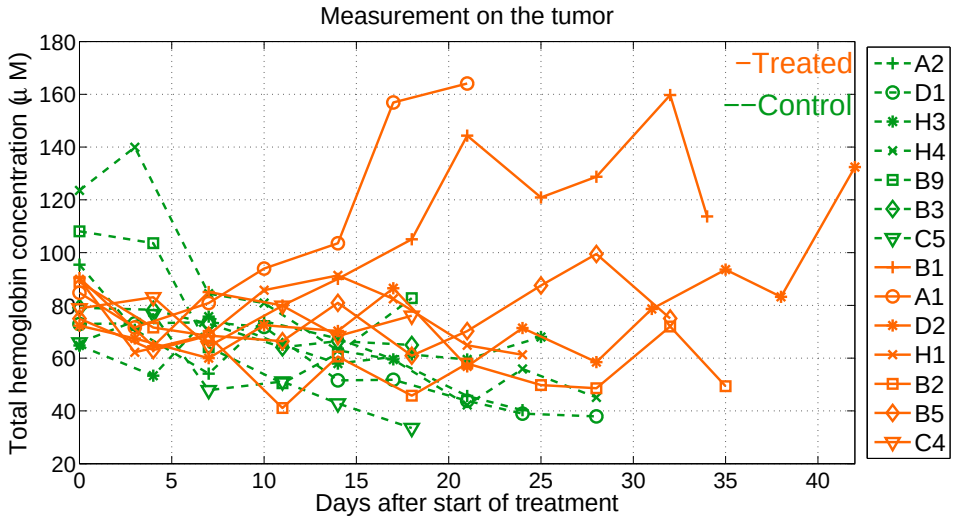

Fig. B.3 Total hemoglobin concentration of both treated (solid orange lines) and control mice (dashed green lines) are presented over all days of measurement. Treated animal

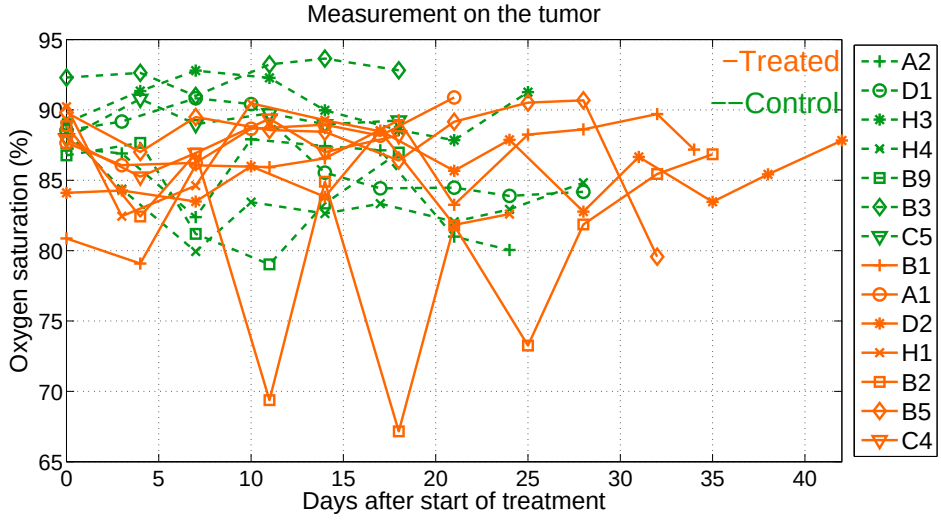

Fig. B.4 Oxygen saturation of both treated (solid orange lines) and control mice (dashed green lines) are presented over all days of measurement. Treated animal

Appendix C

Optical and physiological properties of manubrium.

In this appendix the measured optical (μ_a and μ_s') and physiological parameters (blood flow index, blood volume, and oxygen saturation) of the manubrium for all subjects are presented.

Table C.1 Absorption coefficient (cm^{-1}) of the manubrium.

Subject	λ = 690 nm	λ = 785 nm	λ = 830 nm
01	0.10 ± 0.00	0.11 ± 0.00	0.12 ± 0.00
02	0.15 ± 0.01	0.15 ± 0.01	0.16 ± 0.01
03	0.10 ± 0.00	0.10 ± 0.01	0.10 ± 0.01
04	0.08 ± 0.01	0.09 ± 0.01	0.10 ± 0.01
05	0.17 ± 0.00	0.16 ± 0.01	0.17 ± 0.01
06	0.14 ± 0.01	0.15 ± 0.01	0.16 ± 0.01
07	0.12 ± 0.01	0.12 ± 0.01	0.12 ± 0.01
08	0.09 ± 0.01	0.09 ± 0.01	0.10 ± 0.01
09	0.13 ± 0.00	0.13 ± 0.00	0.14 ± 0.00
10	0.15 ± 0.00	0.16 ± 0.00	0.17 ± 0.00

(Continued.)

Subject	$\lambda = 690$ nm	$\lambda = 785$ nm	$\lambda = 830$ nm
11	0.12 ± 0.01	0.14 ± 0.01	0.15 ± 0.01
12	0.14 ± 0.02	0.15 ± 0.02	0.16 ± 0.02
13	0.10 ± 0.01	0.11 ± 0.01	0.12 ± 0.01
14	0.16 ± 0.02	0.17 ± 0.02	0.17 ± 0.02
15	0.19 ± 0.02	0.19 ± 0.02	0.19 ± 0.02
16	0.13 ± 0.01	0.15 ± 0.01	0.16 ± 0.01
17	0.21 ± 0.03	0.20 ± 0.02	0.21 ± 0.02
18	0.18 ± 0.01	0.18 ± 0.01	0.20 ± 0.01
19	0.17 ± 0.01	0.17 ± 0.01	0.18 ± 0.01
20	0.17 ± 0.00	0.19 ± 0.00	0.20 ± 0.00
21	0.11 ± 0.00	0.12 ± 0.00	0.13 ± 0.00
22	0.22 ± 0.02	0.22 ± 0.01	0.24 ± 0.02
23	0.05 ± 0.01	0.06 ± 0.01	0.06 ± 0.01
24	0.14 ± 0.01	0.15 ± 0.01	0.16 ± 0.01
25	0.15 ± 0.02	0.16 ± 0.02	0.18 ± 0.02
26	0.12 ± 0.02	0.12 ± 0.02	0.14 ± 0.02
27	0.20 ± 0.01	0.19 ± 0.01	0.21 ± 0.02
28	0.13 ± 0.01	0.14 ± 0.01	0.15 ± 0.01
29	0.17 ± 0.01	0.17 ± 0.01	0.18 ± 0.01
30	0.11 ± 0.00	0.12 ± 0.00	0.13 ± 0.00
31	0.16 ± 0.02	0.17 ± 0.03	0.18 ± 0.03
32	0.12 ± 0.00	0.14 ± 0.00	0.15 ± 0.00

Table C.2 Reduced scattering coefficient (cm^{-1}) of the manubrium.

Subject	$\lambda = 690$ nm	$\lambda = 785$ nm	$\lambda = 830$ nm
01	10.1 ± 0.4	09.5 ± 0.3	08.9 ± 0.4
02	11.4 ± 0.3	10.4 ± 0.2	09.3 ± 0.2
03	10.4 ± 0.7	09.9 ± 0.7	09.2 ± 0.6
04	09.6 ± 0.9	09.3 ± 0.9	08.6 ± 0.9
05	10.8 ± 1.0	10.2 ± 0.8	09.3 ± 0.7
06	10.1 ± 1.1	09.7 ± 1.0	08.8 ± 0.9
07	11.0 ± 1.2	10.6 ± 1.1	09.9 ± 1.0
08*	09.3 ± 0.3	08.9 ± 0.2	08.2 ± 0.2
09	09.8 ± 0.3	09.0 ± 0.3	08.3 ± 0.3
10	10.0 ± 0.8	09.3 ± 0.7	08.5 ± 0.7
11	09.7 ± 0.6	09.0 ± 0.5	08.3 ± 0.5
12	10.4 ± 0.7	09.6 ± 0.7	08.6 ± 0.6
13	09.9 ± 0.1	09.2 ± 0.2	08.5 ± 0.2
14	13.2 ± 0.4	12.6 ± 0.3	11.2 ± 0.3
15*	12.1 ± 0.4	11.5 ± 0.3	10.1 ± 0.3
16	09.7 ± 0.3	08.9 ± 0.3	08.3 ± 0.3
17	11.0 ± 0.3	10.1 ± 0.2	09.2 ± 0.3
18*	11.1 ± 0.4	10.2 ± 0.6	09.0 ± 0.5
19	12.1 ± 0.4	11.5 ± 0.4	10.2 ± 0.4
20	10.7 ± 0.2	10.3 ± 0.2	09.5 ± 0.2
21	10.3 ± 0.2	09.6 ± 0.2	08.9 ± 0.2
22	10.2 ± 0.5	09.2 ± 0.7	08.4 ± 0.5
23	09.5 ± 0.2	08.7 ± 0.2	08.1 ± 0.2
24	09.4 ± 0.5	08.9 ± 0.5	08.1 ± 0.4
25	11.3 ± 0.9	10.3 ± 0.8	09.4 ± 0.7
26	11.1 ± 0.4	10.1 ± 0.4	09.6 ± 0.3
27	09.8 ± 1.6	09.0 ± 0.6	08.4 ± 0.6
28	09.0 ± 0.5	08.3 ± 0.5	07.9 ± 0.5
29	10.2 ± 0.6	09.1 ± 0.5	08.3 ± 0.4
30	09.5 ± 0.2	08.8 ± 0.1	08.2 ± 0.1
31	10.8 ± 0.6	10.2 ± 0.5	09.0 ± 0.6
32	09.7 ± 0.3	09.4 ± 0.3	08.3 ± 0.3

Table C.3 Physiological parameters of the manubrium.

Subject	Blood flow index (cm^2/s)	Blood volume (μM)	Oxygen saturation (%)
01	$4.4\times10^{-9} \pm 1.6\times10^{-9}$	56.0 ± 1.4	71.4 ± 2.1
02	$4.0\times10^{-9} \pm 3.7\times10^{-10}$	77.3 ± 5.8	69.8 ± 0.9
03	$3.5\times10^{-9} \pm 6.2\times10^{-10}$	50.0 ± 3.1	68.5 ± 1.8
04	$7.4\times10^{-9} \pm 2.0\times10^{-9}$	48.4 ± 5.6	73.6 ± 1.2
05	$6.5\times10^{-9} \pm 2.6\times10^{-9}$	82.1 ± 5.4	65.2 ± 3.3
06	$5.6\times10^{-9} \pm 1.4\times10^{-9}$	78.7 ± 3.3	71.0 ± 1.1
07	$3.5\times10^{-9} \pm 1.0\times10^{-9}$	60.6 ± 3.9	69.4 ± 1.4
08*	$2.7\times10^{-9} \pm 6.3\times10^{-10}$	46.7 ± 4.8	68.5 ± 1.8
09	$3.7\times10^{-9} \pm 1.2\times10^{-9}$	70.1 ± 1.8	70.5 ± 1.0
10	$6.5\times10^{-9} \pm 2.9\times10^{-9}$	83.6 ± 2.1	71.7 ± 0.7
11	$4.5\times10^{-9} \pm 1.1\times10^{-9}$	73.2 ± 6.6	75.0 ± 0.5
12	$7.3\times10^{-9} \pm 3.0\times10^{-9}$	79.8 ± 10.5	71.8 ± 1.2
13	$5.1\times10^{-9} \pm 1.0\times10^{-9}$	55.5 ± 5.7	71.9 ± 1.1
14	$7.5\times10^{-9} \pm 2.4\times10^{-9}$	85.8 ± 9.3	70.6 ± 0.6
15*	$2.9\times10^{-9} \pm 5.3\times10^{-10}$	95.3 ± 11.4	67.8 ± 0.8
16	$8.7\times10^{-9} \pm 2.6\times10^{-9}$	77.2 ± 5.3	73.3 ± 0.6

(Continued.)

Subject	Blood flow index (cm^2/s)	Blood volume (μM)	Oxygen saturation (%)
17	$4.8\times10^{-9} \pm 1.1\times10^{-9}$	103.7 ± 12.1	65.9 ± 1.7
18*	$1.0\times10^{-8} \pm 5.3\times10^{-9}$	95.9 ± 4.0	70.1 ± 2.1
19	$4.3\times10^{-9} \pm 6.9\times10^{-10}$	88.8 ± 4.8	68.8 ± 1.1
20	$8.2\times10^{-9} \pm 2.2\times10^{-9}$	98.1 ± 1.8	72.6 ± 0.8
21	$4.7\times10^{-9} \pm 1.0\times10^{-9}$	61.1 ± 1.0	73.4 ± 0.9
22	$5.2\times10^{-9} \pm 1.5\times10^{-9}$	115.4 ± 6.3	70.1 ± 2.7
23	$9.7\times10^{-9} \pm 3.1\times10^{-9}$	29.6 ± 3.0	76.9 ± 1.3
24	$5.8\times10^{-9} \pm 1.9\times10^{-9}$	77.3 ± 6.1	72.1 ± 1.3
25	$9.2\times10^{-9} \pm 1.7\times10^{-9}$	86.5 ± 9.2	74.1 ± 1.0
26	$3.8\times10^{-9} \pm 1.1\times10^{-9}$	66.0 ± 9.2	71.8 ± 1.1
27	$8.4\times10^{-9} \pm 1.7\times10^{-9}$	101.0 ± 6.7	68.4 ± 2.3
28	$4.9\times10^{-9} \pm 2.0\times10^{-9}$	71.4 ± 4.3	70.8 ± 0.5
29	$6.0\times10^{-9} \pm 1.5\times10^{-9}$	90.0 ± 5.9	69.5 ± 1.0
30	$4.1\times10^{-9} \pm 1.4\times10^{-9}$	63.4 ± 2.4	71.9 ± 0.6
31	$4.8\times10^{-9} \pm 1.2\times10^{-9}$	88.4 ± 14.6	71.2 ± 1.4
32	$4.6\times10^{-9} \pm 1.6\times10^{-9}$	70.6 ± 1.9	73.2 ± 1.4

* Smoker subjects.

Appendix D

Optical and physiological properties of patella.

In this appendix the measured optical (μ_a and μ_s') and physiological parameters (blood flow index, blood volume, and oxygen saturation) of the patella for all subjects are presented.

Table D.1 μ_a values of the patella in three wavelengths during rest.

	μ_a (cm^{-1})		
	$\lambda = 690\ nm$	$\lambda = 785\ nm$	$\lambda = 830\ nm$
Subject 1	0.044 ± 0.007	0.034 ± 0.004	0.045 ± 0.004
Subject 2	0.041 ± 0.004	0.037 ± 0.002	0.042 ± 0.003
Subject 3	0.053 ± 0.009	0.055 ± 0.004	0.071 ± 0.006
Subject 4	0.024 ± 0.006	0.026 ± 0.003	0.038 ± 0.003
Subject 5	0.029 ± 0.004	0.027 ± 0.002	0.033 ± 0.003
Subject 6	0.046 ± 0.006	0.037 ± 0.004	0.041 ± 0.004
Subject 7	0.043 ± 0.004	0.040 ± 0.003	0.044 ± 0.003
Subject 8	0.028 ± 0.009	0.032 ± 0.002	0.048 ± 0.003

Table D.2 $\mu_s{}'$ values of the patella in three wavelengths during rest.

	$\mu_s{}'$ (cm^{-1})		
	$\lambda = 690\ nm$	$\lambda = 785\ nm$	$\lambda = 830\ nm$
Subject 1	6.1 ± 0.2	4.3 ± 0.3	3.5 ± 0.2
Subject 2	8.7 ± 0.2	6.5 ± 0.3	5.2 ± 0.2
Subject 3	6.3 ± 0.2	4.5 ± 0.2	3.7 ± 0.2
Subject 4	6.0 ± 0.2	4.3 ± 0.2	3.7 ± 0.2
Subject 5	7.1 ± 0.2	5.3 ± 0.2	4.3 ± 0.2
Subject 6	9.2 ± 0.3	6.5 ± 0.5	5.2 ± 0.3
Subject 7	8.6 ± 0.2	6.6 ± 0.3	5.4 ± 0.2
Subject 8	7.2 ± 0.2	4.9 ± 0.2	3.8 ± 0.2

Table D.3 Total hemoglobin concentration and oxygen saturation during rest.

	Total hemoglobin concentration (μM)	Oxygen saturation(%)
Subject 1	20 ± 2	63 ± 8
Subject 2	20 ± 1	66 ± 4
Subject 3	32 ± 3	76 ± 4
Subject 4	16 ± 2	81 ± 6
Subject 5	15 ± 1	70 ± 6
Subject 6	20 ± 2	60 ± 7
Subject 7	21 ± 1	66 ± 5
Subject 8	20 ± 3	83 ± 5

Table D.4 μ_a values in three wavelengths at the end of cuff occlusion.

	μ_a (cm^{-1})		
	$\lambda = 690\ nm$	$\lambda = 785\ nm$	$\lambda = 830\ nm$
Subject 1	0.069 ± 0.007	0.057 ± 0.007	0.062 ± 0.012
Subject 3	0.103 ± 0.008	0.076 ± 0.007	0.086 ± 0.008
Subject 5	0.058 ± 0.005	0.050 ± 0.006	0.054 ± 0.007
Subject 6	0.088 ± 0.015	0.077 ± 0.015	0.085 ± 0.031
Subject 7	0.092 ± 0.009	0.088 ± 0.012	0.093 ± 0.016
Subject 8	0.062 ± 0.006	0.069 ± 0.012	0.118 ± 0.032
Average	0.079 ± 0.016	0.069 ± 0.013	0.083 ± 0.021

Table D.5 $\mu_s{}'$ values in three wavelengths at the end of cuff occlusion.

	$\mu_s{}'$ (cm^{-1})		
	$\lambda = 690\ nm$	$\lambda = 785\ nm$	$\lambda = 830\ nm$
Subject 1	8.6 ± 0.5	5.5 ± 0.3	4.3 ± 0.3
Subject 3	6.5 ± 0.3	4.5 ± 0.2	3.8 ± 0.2
Subject 5	7.3 ± 0.3	5.5 ± 0.3	4.6 ± 0.2
Subject 6	10.7 ± 0.9	7.3 ± 0.8	5.7 ± 0.9
Subject 7	11.0 ± 0.5	9.1 ± 1.0	7.8 ± 0.9
Subject 8	5.7 ± 0.3	3.9 ± 0.2	2.8 ± 0.3
Average	8.3 ± 2.2	6.0 ± 1.9	4.8 ± 1.7